SINGLE-FREQUENCY, SINGLE-RECEIVER TERRESTRIAL AND SPACEBORNE POINT POSITIONING

TOMAS BERAN

August 2008

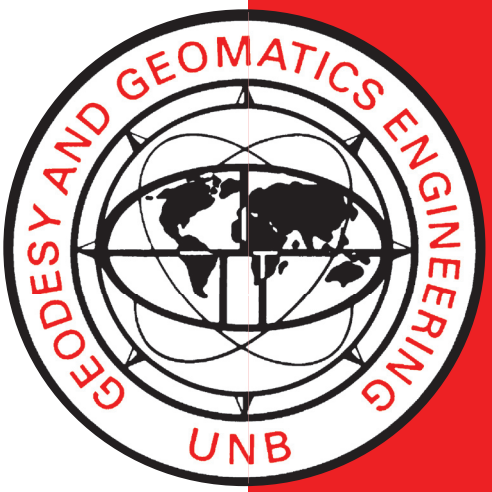

TECHNICAL REPORT
NO. 257

SINGLE-FREQUENCY, SINGLE-RECEIVER TERRESTRIAL AND SPACEBORNE POINT POSITIONING

Tomas Beran

Department of Geodesy and Geomatics Engineering
University of New Brunswick
P.O. Box 4400
Fredericton, N.B.
Canada
E3B 5A3

August 2008

PREFACE

This technical report is a reproduction of a dissertation submitted in partial fulfillment of the requirements for the degree of Doctor of Philosophy in the Department of Geodesy and Geomatics Engineering, May 2008. The research was supervised by Dr. Richard Langley, and funding was provided by the Natural Sciences and Engineering Research Council of Canada.

As with any copyrighted material, permission to reprint or quote extensively from this report must be received from the author. The citation to this work should appear as follows:

Beran, Tomas (2008). *Single-Frequency, Single-Receiver Terrestrial and Spaceborne Point Positioning*. Ph.D. dissertation, Department of Geodesy and Geomatics Engineering, Technical Report No. 257, University of New Brunswick, Fredericton, New Brunswick, Canada, 185 pp.

ABSTRACT

High-accuracy, point positioning has been an attractive research topic in the GPS community for a number of years. The overall quality of precise point positioning results is also dependent on the quality of the GPS measurements and the user's processing software. Dual-frequency, geodetic-quality GPS receivers are routinely used both in static and kinematic applications for high-accuracy point positioning. However, use of low-cost, single-frequency GPS receivers in similar applications creates a challenge because of difficulty of handling the ionosphere, multipath and other measurement error sources. Potential use of such receivers to provide horizontal positioning accuracies of a few decimetres, and vertical accuracies of less than two metres, will be examined in this dissertation. Practical applications of post-processed, high-accuracy, single-frequency point positioning include a myriad of terrestrial and space-borne applications, where the size and cost of the GPS unit is an issue.

The processing technique uses pseudorange and time-differenced carrier-phase measurements in a sequential least-squares filter. In developing the approach, different techniques were investigated. Ionospheric delay grid maps are used to remove the bulk of the ionospheric error, while tropospheric error is handled by a prediction model. Pseudorange multipath errors are mitigated by means of stochastic modelling and carrier-phase cycle slips are detected and corrupted measurements are removed in a quality-control algorithm.

The technique was first tested on L1 measurements extracted from datasets from static, high-quality GPS receivers. Accuracies better than two-decimetres in horizontal components (northing and easting r.m.s.), and three-decimetre accuracies in the vertical component (up-component r.m.s.), were obtained. A test dataset from a stationary low-cost GPS receiver has been processed to demonstrate the difference in data quality. Positioning results obtained are worse than those of a high-quality GPS receiver, but they are still within the few decimetre accuracy level (northing and easting r.m.s.) and less than two metre vertical accuracy level. The use of the technique is not restricted to static applications, and the results of kinematic experiments are also presented. These experiments consist of terrestrial data processing and spaceborne data processing. The kinematic terrestrial tests include processing of single-frequency data from geodetic-quality GPS receiver and low-cost GPS receiver from a moving vehicle. The spaceborne kinematic tests include processing of dual-frequency data from a geodetic-quality GPS receiver on board of a low Earth orbit (LEO) satellite, and processing of the simulated single-frequency data from a low-cost GPS receiver for a future satellite mission.

The question whether it is possible to use low-cost GPS receivers for high accuracy GPS positioning has been answered. Contributions to the leading edge research in the area of high precision GPS point positioning have been made. The software that was developed is the only software capable of reliable pseudorange and carrier-phase data processing from low-cost GPS receivers. Its reliability is accomplished through data quality control based on residual outlier detection theory. The implemented algorithm is capable to detect 95% of outliers. Despite the encouraging results the limitations of this

technique were found. During the static terrestrial data testing it was found that the presence of multipath has negative impact on the positioning results from low-cost GPS receivers. The kinematic terrestrial data testing is limited to short periods of time when a reliable reference solution is available. The majority of the test results are from terrestrial platforms, because the spaceborne single-frequency point positioning requires more sophisticated ionospheric models than the terrestrial single-frequency point positioning. One example of sophisticated ionospheric model is a global 3D ionospheric model which was tested in this dissertation.

ACKNOWLEDGEMENTS

I would like to thank my advisor, Richard Langley for giving me the opportunity to perform this research, for his continuing support and all of his advices on all related and unrelated topics. I would like to thank Canadian research agencies for funding this research and international research organizations for providing access to the GPS data. I would like to thank my family, who encouraged me to pursue this journey, which literally changed my life. I would like to thank my wife Angela for her continuing support. Last but not least, I would like to thank all of you my friends, who helped me during my studies, you know who you are.

TABLE OF CONTENTS

LIST OF FIGURES

LIST OF TABLES

LIST OF SYMBOLS

A	(various)	design (measurement partials) matrix
C	(various)	variance-covariance matrix
H	(various)	linearized system design matrix
I	(various)	identity matrix
P	(various)	weight matrix
Q	(various)	process noise variance-covariance matrix
R	(various)	measurement noise variance-covariance matrix
e	(various)	measurement error vector
l	(various)	measurement vector
v	(various)	residual vector
w	(various)	misclosure vector
x	(various)	state vector
c	(m/s)	vacuum speed of light
d_{ion}	(m)	ionospheric delay or advance
d_{trop}	(m)	tropospheric delay
d_{hyd}	(m)	hydrostatic part of the tropospheric delay
d_{wet}	(m)	non-hydrostatic part of the tropospheric delay
e	(m)	pseudorange random noise
f	(Hz)	frequency
M	(unitless)	length of filter smoothing
N	(unitless)	carrier-phase integer ambiguity
P	(m)	pseudorange measurement
S	(various)	spectral amplitudes
Φ	(m)	carrier-phase measurement
$\delta\mathbf{x}$	(various)	corrections vector
ε	(m)	carrier-phase random noise
λ	(m)	GPS signal wavelength
σ	(various)	standard deviation

LIST OF ACRONYMS

AAC	Associate Analysis Centres
ASI	Agenzia Spaziale Italiana
CHAMP	Challenging Minisatellite Payload
CNES	Centre National d'Etudes Spatiales
CODE	Centre for Orbit Determination in Europe
CSR	Centre for Space Research
CSRS	Canadian Spatial Reference System
DARTS	Dynamic Ambiguities Estimation
DEOS	Delft Institute for Earth Oriented Space Research
DLL	Delay Lock Loop
DORIS	Doppler Orbitography and Radiopositioning integrated by Satellite
ESOC	European Space Operation Centre
GDOP	Geometrical Dilution of Precision
GFZ	Geo Forschungs Zentrum
GIM	Global Ionospheric Map
GNSS	Global Navigation Satellite System
GPS	Global Positioning System
GRAPHIC	Group and Phase Ionosphere Calibration
GRGS	Groupe de Recherche de Géodésie Spatiale
GRL	Geodetic Research Laboratory
ICD	Interface Control Document
IEEE	Institute of Electrical and Electronics Engineers
IGS	International GNSS Service
INS	Inertial Navigation System
IOC	Initial Operational Capability
ION	Institute of Navigation
IONEX	Ionosphere Map Exchange Format
JPL	Jet Propulsion Laboratory
KMS	Kort&Matrikelstyrensen
LEO	Low Earth Orbit
MPGPS	Multi-Purpose GPS Processing Software
NASA	National Aeronautics and Space Administration
NCL	Newcastle University
NOAA	National Oceanic and Atmospheric Administration
OCXO	Oven Controlled Crystal Oscillator
PPP	Precise Point Positioning
PRN	Pseudo Random Number
RINEX	Receiver Independent Exchange Format
RTK	Real-Time Kinematic
SGPS	Spaceborne GPS
SLR	Satellite Laser Ranging
SPAN	Synchronized Position and Attitude Navigation

TCXO	Temperature Controlled Crystal Oscillator
TEC	Total Electron Contend
TTC	Trimble Total Control
UNB	University of New Brunswick
VRS	Virtual Reference Stations
WAAS	Wide Area Augmentation System
WADGPS	Wide Area Differential GPS

1 Introduction

Use of satellite geodetic techniques in the second half of the twentieth century began a new era in positioning and navigation. Astronomers and physicists studied the principles of celestial mechanics for more than four hundred years and scientific and technological discoveries in the last century enabled people to launch the first artificial satellite and enter the space surrounding our planet. Within a couple of decades it was possible to determine the position of artificial, and natural, Earth satellites at the few-metre-level at any given time. The idea of reversing the traditional observation equation and using artificial satellites as "fixed" monuments in space gave birth to the satellite-based global navigation systems (or global navigation satellite systems (GNSS) which is today's generic term for such systems).

The American Global Positioning System (GPS) is one of the oldest continuously maintained systems in the GNSS group. During more than twenty-five years of its existence, this satellite-based navigation system has been a valuable tool for the civilian geo-scientific research community. GPS now directly and indirectly influences our lives and the evolution of this system still continues. The University of New Brunswick (UNB) Geodetic Research Laboratory (GRL) has been on the leading edge of the positioning and navigation research almost as long as GPS has been available. The GRL goal is to develop and test algorithms that are faster, more accurate, more reliable and cost-efficient and use this (and other) positioning systems in new and innovative applications. Spaceborne GPS applications fit well into this category of applications for numerous reasons (for example the demand for low-cost attitude determination). The research

challenge is to develop a filter that will provide orbit information for satellites below the GPS constellation. The software also has to operate with a minimum of remote user interaction for the entire expected lifetime of the platform that it is built for.

1.1 Research Motivation and Dissertation Statement

In order to achieve high-accuracy point positioning results using GPS, numerous research groups have used dual-frequency, geodetic-quality receiver data. The UNB GRL achieved sub-decimetre-level results in static and kinematic mode in this research area [Bisnath, 2004]. The Geodetic Survey Division of Natural Resources Canada introduced an on-line post-processing precise positioning service that facilitates access to the Canadian Spatial Reference Frame (CSRS-PPP). The providers of the service claim that the resulting cm-level accuracy for static positioning is comparable to phase-differential GPS, for dual and single-frequency geodetic-quality receiver data [Tétreault et al., 2005]. Researchers from the Jet Propulsion Laboratory (JPL) evaluated the real-time positioning performance of a single-frequency receiver using the 1-Hz differential corrections provided by NASA's Global Differential GPS System [Muellerschoen et al., 2004]. The results obtained using single-frequency data from a geodetic-quality receiver are of similar accuracy to those obtained by the CSRS-PPP.

The overall quality of precise point positioning results is also dependent on the quality of the GPS measurements and the user's processing software. Dual-frequency, geodetic-

quality GPS receivers are routinely used both in static and kinematic applications for high-accuracy point positioning. However, use of low-cost, single-frequency GPS receivers in similar applications creates a challenge because of how the ionosphere, multipath and other measurement error sources are handled. In this thesis, potential use of such receivers to provide horizontal positioning accuracies of a few decimetres, and vertical accuracies of less than two metres, is investigated. Practical applications of post-processed, high-accuracy, single-frequency point positioning include a myriad of terrestrial and space-borne applications (for example geo-referencing for Geographic Information Systems), where the size and cost of the GPS unit is an issue.

Acceptance of a new approach is dependent upon cost considerations. A low-grade (L1 C/A-code) receiver coupled with a single patch antenna is cost effective, because the number of receiver tracking channels is half that of a dual-frequency receiver. Further GPS receiver hardware and software simplification results from the fact that a low-cost receiver does not track the P-code. A point positioning experiment with low-cost GPS receivers, summarized by Montenbruck and Gill [2001], demonstrates the potential use of this technique on LEO satellites. The model of the fractional total electron contend (TEC) above the receiver altitude, accounts for roughly 90% of the total ionospheric delay. The accuracy of the model is limited by the capability to adjust the TEC scaling factor.

There are two primary reasons to consider research in point positioning techniques for ground-based applications. The first reason is that the community of the potential users of this point positioning technique is much larger than the community of potential GPS

users in the spaceborne environment. The second reason is the access to the GPS data. In order to validate the high-accuracy point positioning technique on a particular GPS receiver, ground–based static and kinematic data must be collected, processed and analysed.

One of the primary applications of this research is low-earth orbiter (LEO) sensor positioning (e.g., for gravity field modelling, altimetry, atmospheric occultation and geocoding or geolocation of remote sensing data). Satellite applications are driven by technical and commercial constraints. The majority of satellites are launched into near circular orbits with altitudes of 300 - 1500 km, and they are considered as LEOs [Montenbruck and Gill, 2000]. GPS receivers can provide precise and continuous platform position and velocity. Moreover, the advantage of GPS over all tracking systems, is that the system is capable of providing tracking for highly dynamic platforms, such as LEOs. Engineering spaceborne GPS (SGPS) applications use GPS-derived information for spacecraft operations. These applications are also evolving into autonomous spacecraft navigation systems to allow autonomous manoeuvre planning and formation flying.

The dissertation question could be summarized as follows: What is the maximum accuracy that could be currently obtained from an L1 C/A-code GPS receiver used for positioning of spaceborne platforms? It is known that the results from geodetic-quality GPS receivers in space will be better than those of low-cost receivers. In order to achieve higher accuracy, is it necessary to use a higher-quality GPS receiver, or is it necessary to

provide additional orbit information, or is it necessary to utilise both? The same type of GPS receiver will be first used to collect data on the ground and the series of ground-based tests will help provide the maximum accuracies.

1.2 Contributions of this Research

The first contribution of this research is an in-depth comparison of the quality of the data from low-cost GPS receivers with the data obtained from geodetic-quality GPS receivers. The comparison is done on multiple datasets from different receivers, varying atmospheric conditions, and site conditions on static and kinematic platforms, on the surface of the Earth and in space. The second contribution is the evaluation of the 3D ionospheric model and its use in the precise point positioning software. The third contribution is the software implementation itself, because the software implemented is, to the best of my knowledge, the only software capable of processing carrier-phase (and pseudorange) measurements from low-cost GPS receivers.

Dealing with GPS data from low-cost receivers emphasized the need for robust quality control algorithms. The data quality control methods investigated include residual outlier detection and cycle-slip detection. The cycle-slip detection algorithm uses an approach, which is based on higher-order differences of carrier-phase observations and a repeated search through all satellites in view. The data quality control algorithms are directly related to the measurement stochastic modelling. Issues like data sampling interval, and

impact of measurement weighting were considered and the results are covered in this dissertation.

Atmospheric measurement errors are also an integral part of this research. The prediction models for ionospheric and tropospheric delays under normal atmospheric conditions remove most of the atmospheric error. The residual tropospheric delay error is typically about one order of magnitude bigger than the residual ionospheric delay error (Note: This depends on models used. The ionospheric delay error would be bigger if for example, the Klobuchar model is used). This fact and the fact that the primary applications of this research were spaceborne platforms, which will experience almost no tropospheric delay, explains why the atmospheric research emphasis is on the ionospheric delay. The accuracy of the ionospheric delay models under varying conditions and alternative methods for ionospheric error handling were investigated.

1.3 Outline of the Dissertation

The structure of this dissertation follows the progression of the research. The state of art of the GPS point positioning technique is given in Chapter 2. Chapter 3 describes the research that was conducted in a chronological order. It starts with descriptions of the filter models that were investigated in order to determine the most suitable model for the kinematic point positioning applications. Chapter 4 describes the mathematical model used to obtain the results presented in this dissertation. The follow-up sections are

dedicated to all measurement error sources that need to be addressed. Special attention is paid to the measurement sources specific to low-cost GPS receivers and spaceborne GPS receivers.

Chapter 5 describes the sequence of tests needed to validate the low-cost GPS point positioning technique in a spaceborne environment. It starts with ground-based static and kinematic tests, which highlight the differences between the low-cost GPS receiver data and the geodetic-quality-receiver data, as well as the difference between static and kinematic datasets. Spaceborne data testing consists of real data from a geodetic-quality receiver in space and the simulated data from a low-cost GPS receiver.

Chapter 6 provides the summary of the ground-based and spaceborne data testing and Chapter 7 provides suggestions for future research and further improvements in the area of high-accuracy, low-cost point positioning.

2 Recent Developments in Single Point Positioning

A short description of recent developments starts with a description of the "state-of-art" point positioning technique, which relies on the data from global networks of geodetic-quality GPS receivers. The following sections provide a summary of recent developments in terrestrial and spaceborne point positioning.

2.1 Single Point Positioning Concept

Recent single point positioning concepts enhance pseudorange-based positioning with carrier-phase processing. Data from global networks of geodetic-quality GPS receivers continuously examined and processed in International GNSS Service (IGS) processing centres provide precise GPS satellite orbits and precise satellite clock offset estimates necessary for high-accuracy single point positioning. Processing of undifferenced pseudorange and carrier-phase data from a single GPS receiver, integrated with precise GPS orbit and clock products is called Precise Point Positioning (PPP).

A carrier-phase-filtered pseudorange processing technique first proposed by Ron Hatch in the early 1980's [Hatch, 1982] is given by:

$$\hat{\mathbf{P}}(t_i) = \frac{1}{M}\mathbf{P}(t_i) + \frac{M-1}{M}(\mathbf{P}(t_{i-1}) + (\mathbf{\Phi}(t_i) - \mathbf{\Phi}(t_{i-1})) \qquad (2.1)$$

where $\hat{\mathbf{P}}(t_i)$ are the estimated pseudorange at the current epoch in metres, $\mathbf{P}(t_i)$ and

$\mathbf{P}(t_{i-1})$ are the observed pseudorange at the current and at the previous epoch, respectively in metres, $\mathbf{\Phi}(t_i)$ and $\mathbf{\Phi}(t_{i-1})$ are the carrier phases at the current and at the previous epoch respectively, and M is the number of epochs used for filtering (the length of the filter).

The carrier-phase and pseudorange combination uses averaged noisy code-phase range measurements to estimate the ambiguity term in the precise carrier-phase measurements. The longer the pseudorange averaging, which requires continuous, cycle-slip-free, carrier-phase measurements, the better the carrier-phase ambiguity estimate.

Point-positioning-processing modelling considerations include relativistic GPS satellite clock correction due to the eccentricity of the GPS satellite orbits; GPS satellite phase-centre to centre-of-mass offset; GPS satellite phase wind-up due to the relative rotation of the GPS satellite antennas with respect to the receiver antenna [Note that receiver antenna rotations may also contribute to phase wind up]; sub-diurnal variations in Earth rotation; solid Earth tides; ocean loading; and consistency between models used in the generation of GPS orbits and clocks and models used in the point positioning processing [Bisnath and Langley, 2002]. A table showing typical sizes of these effects [Tétreault et al., 2005] is reproduced below.

Correction	Reason	Magnitude
Satellite Antenna	To account for the difference between the satellite centre of mass, to which the satellite coordinates are referenced, and the phase centre of the antenna, from which observations are measured.	metre-level
Phase Wind-Up	To account for a change in phase measurement due to the satellite rotating around its vertical axis, during noon-turn and eclipse for example.	dm-level
Solid Earth Tides	To account for the periodic displacement of the Earth's crust due to Sun and Moon.	dm-level
Ocean-Loading	To account for the deformation of the Earth's crust caused by the increased load of water along the coast resulting from tides.	cm-level
Periodic Relativity	To account for the effect of relativity on the GPS on-board atomic clock.	metre-level
Pseudo-Range or Differential Code Bias	To conform to the IGS convention regarding the combination of pseudo-range observations used. $\mathbf{P}_{C/A}$ and $\mathbf{P}_{C/A} + (\mathbf{P}_2 - \mathbf{P}_1)$ (Up to April 2, 2002) $\mathbf{P}_2$ and $\mathbf{P}_1$ (After April 2, 2002)	2 ns on user's clock
User Antenna	To account for user-antenna phase-centre variations.	cm-level

Table 2.1: Effects modelled in PPP Estimation [Tétreault et al., 2005].

2.2 Recent Developments in Ground-based Point Positioning

Precise point positioning (PPP) is a very active research area. The Institute of Navigation (ION) has typically dedicated a separate PPP session at their annual international technical meetings since 2004. This section will describe the results achieved by:

- Other university research groups,
- Government research agencies, and
- Global point positioning services (Wide Area Differential GPS (WADGPS) Services) from private industry companies.

Researchers from the Hydrographic Science Research Center of the Department of Marine Science of the University of Southern Mississippi carried out an evaluation of the commercial WADGPS services [Bisnath et al., 2003]. Three services were studied:

- NavCom Technology, Inc. Starfire;
- C&C Technologies, Inc. C-Nav; and
- Thales GeoSolutions Group Ltd. SkyFix XP.

The tests of all three systems were divided into static and marine kinematic tests. The static data were collected from three setups on the roof of a building at the Stennis Space Center in Mississippi. Approximately two weeks of data were collected for the static, day-long evaluations. The reference solutions for the static data tests were obtained by processing the two weeks of the raw GPS data in the U.S. National Geodetic Survey OPUS processing engine. The kinematic evaluation was made by comparing the WADGPS solutions with short baseline (few-km) RTK solutions produced by the GrafNav GPS processing package from WayPoint Positioning, Inc. (now a subsidiary company of NovAtel Inc.) All of the kinematic tests were performed during the same time period on the same vessel. Table 2.2 summarizes the standard deviations of the horizontal and vertical components of the static results after convergence periods, which usually took about 30 minutes and Table 2.3 summarizes the standard deviations of the

horizontal and vertical components of the kinematic results after about 30 minutes convergence periods as reported by the authors.

	C-Nav	Starfix-HP	SkyFix XP
Long-term static positioning precision	5-10 cm hor. and 20 cm vert. (1σ)	5 cm hor. and 15 cm vert. (1σ)	10 cm hor. and 20-30 cm vert. (1σ)
Long-term static positioning accuracy	15 cm hor. and 45 cm vert. (95%)	15 cm hor. and 25 cm vert. (95%)	20 cm hor. and 45 cm vert. (95%)

Table 2.2: Long-term static positioning precision and accuracy [Bisnath et al., 2003].

	C-Nav	Starfix-HP	SkyFix XP
Kinematic positioning precision	5 cm hor. and 10-15 cm vert. (1σ)	5 cm hor. and 5-15 cm vert. (1σ)	5-10 cm hor. and 5-15 cm vert. (1σ)
Kinematic positioning accuracy	5-20 cm hor. and 20-30 cm vert. (95%)	10-15 cm hor. and 15-35 cm vert. (95%)	10-25 cm hor. and 25-60 cm vert. (95%)

Table 2.3: Kinematic positioning precision and accuracy [Bisnath et al., 2003].

The biases observed on the static solutions range from 0.6 to 7 cm horizontally and 1.3 to -19.3 cm vertically. From the published results it can be concluded that the precision and accuracy of the static and kinematic results is at the same level. Positioning at the one-decimetre (1σ) horizontal and two-decimetre (1σ) vertical level is possible after about 30 minutes initialization time.

In 2003 Septentrio company researcher, Andrew Simsky, presented a standalone real-time positioning algorithm based on dynamic ambiguities estimation (DARTS) [Simsky, 2003]. The algorithm consists of Kalman filter processing of undifferenced ionosphere-

free pseudorange and carrier-phase observations. The carrier-phase ambiguities are estimated as unknown parameters, which are allowed to vary from epoch to epoch within the range specified by the Kalman filter process noise parameters (see section 3.4 for more information). Andrew Simsky claims that the "dynamic" ambiguities absorb some of the measurement errors and biases. Resulting standard deviations for position are within the range of 1.0-1.3 m for heights, and 0.6-0.8 m for horizontal coordinates. This level of accuracy has been achieved on static sites in Belgium and Canada, and during kinematic experiments in Europe. Table 2.4 shows the results of the week-long static positioning tests on the rooftop of Septentrio building in Leuven, Belgium.

Static Tests	r.m.s.
Northing Accuracy [cm]	72
Easting Accuracy [cm]	84
Height Accuracy [cm]	130

Table 2.4: r.m.s. of the differences between DARTS solution and a reference solution for static tests [Simsky, 2003]

The Mathematical Geodesy and Positioning group of the Department of Earth Observation and Space Systems of the Faculty of Aerospace Engineering of the Delft University of Technology achieved decimetre accuracy results using undifferenced pseudorange and time-differenced carrier-phase observations from a single-frequency GPS receiver [Le, 2004]. The mathematical formulation of the filter is identical to the one by Bisnath and Langley, [2002]. In order to minimize the effect of error sources present

in single frequency GPS observations, the mathematical model used in Le's research includes: precise IGS ephemerides, global ionospheric maps, a tropospheric delay prediction model and differential code biases. The filter was tested on a series of static and kinematic datasets. Table 2.5 shows statistics of the static test results. Le [2004] states that, "the kinematic test results achieved the same accuracy as the static ones under favourable condition". In summary, the results demonstrate a precision of 2-3 decimetres (standard deviation) for the horizontal position components and 5 decimetres (standard deviation) for the vertical.

Station	Statistics	North [cm]	East [cm]	Height [cm]
Delft	Mean	-2	-7	5
Netherlands	STD	28	22	48
(DELF)	95 %	56	43	93
Penticton,	Mean	2	-4	-64
Canada	STD	30	22	79
(DRAO)	95 %	58	43	137

Table 2.5: Delft's statistics of position estimates in local north, east and height coordinates with one week of data at 30-second interval for two stations [Le, 2004].

In the same year, researchers from the Jet Propulsion Laboratory (JPL), California Institute of Technology, presented a paper on the evaluation of real-time point-positioning performance of single-frequency receivers using NASA's global differential GPS system [Muellerschoen et al., 2004]. The group and phase ionosphere calibration (GRAPHIC) observable was used to eliminate the ionospheric delay [Gold et al., 1994]. This observable takes advantage of the fact that the group delay in the pseudorange observable and the phase advance have the same magnitude, but are opposite in sign. An alternative method of removing the ionospheric delay was presented by Muellerschoen et

al., [2004], which uses a database of global real-time grid maps of ionosphere electron density. Table 2.6 shows the six day r.m.s. results [cm] of one hertz user position error of a global distribution of single-frequency receivers with kinematic positioning using the global differential corrections and the modified GRAPHIC data observable formulated to reduce receiver multipath. The results shown were obtained for North American and European sites over a period of 6 days from August 10th to August 16th, 2004, using an elevation mask angle of 9 degrees and the modified GRAPHIC observable. The choice of a specific value for the elevation mask angle is not explained in the paper.

Site Location	r.m.s. Error North [cm]	r.m.s. Error East [cm]	r.m.s. Error Height [cm]
Urals Ridge, Russia	16	15	22
Colorado Springs, U.S.A.	10	12	34
Brewster, U.S.A.	17	12	31
Delft, Netherlands	9	9	22
Fairbanks, U.S.A.	16	19	39

Table 2.6: JPL's six day r.m.s. results of kinematic positioning with single-frequency receivers using the global differential corrections and the modified GRAPHIC [Muellerschoen et al., 2004].

Ionospheric modeling techniques for real-time single-frequency precise point positioning were investigated by University of Calgary researchers Chen and Gao [2005]. They investigated three types of ionospheric error handling:

1. Klobuchar ionospheric prediction model,
2. Global ionospheric map model, and
3. Ionospheric delay estimation technique.

The ionospheric delay estimation technique with estimated horizontal gradients and global ionospheric maps performed better than the Klobuchar model. Positioning results from mid-latitude stations and quiet ionospheric conditions were investigated. Positioning results were obtained using data from three stations located in different ionospheric regions (equatorial, mid-latitude, and high-latitude) under different ionospheric conditions. The Ap index, which is a measure of the general level of geomagnetic activity over the globe for a given day, was used to define the ionospheric conditions. Static positioning results from the three different stations under three different ionospheric conditions, using data from a global ionospheric model are shown in Table 2.7.

Station	Ap Index	North [cm]	East [cm]	Height [cm]
Galapagos Islands, Ecuador	4	59	65	145
	7	60	96	141
	30	35	60	98
Calgary, Canada	4	26	26	47
	7	28	36	40
	30	31	20	52
Fairbanks, U.S.A.	4	19	21	51
	7	33	28	82
	30	48	33	88

Table 2.7: University of Calgary's static positioning results with global ionospheric model [Chen and Gao, 2005].

Results obtained with an ionospheric estimation model are compatible with those obtained with a global ionospheric model at the decimetre-level range. University of

Calgary's kinematic positioning results, also described in [Chen and Gao, 2005], from an airborne dataset were collected on August 28, 2004 (Ap index: 7) with a NovAtel Black Diamond Receiver (a receiver with inertial navigation system (INS) which is now called SPAN, Synchronized Position Attitude Navigation) with a 512 antenna model with a 1 Hz sampling rate. The airborne dataset was collected on a helicopter flying 250 m above the ground, 40 km north of Halifax, Nova Scotia, Canada. Kinematic point positioning accuracy (with respect to a 10 km baseline reference solution) using a global ionospheric model was 13, 24 and 26 cm in north, east and height component r.m.s. respectively.

In February 2005, a team in the Western Australia Centre for Geodesy at Curtin University of Technology in Perth published their research on an optimum approach to GPS aircraft positioning [Castleden et al., 2005]. Three parallel strategies have been investigated: virtual reference stations (VRSs), precise point positioning and multiple reference stations, but only the first two are compared in their paper. For the long-range VRS software, test results using one-hour of 1 Hz, dual-frequency, airborne kinematic GPS data in Norway showed about 3 cm precision for the horizontal components and about 8 cm precision for the height component. The mean difference between the VRS solution and the reference trajectory, computed from multiple single-baseline solutions, is -0.5 cm in northing, 1.0 cm in easting, and -3.5 cm in height. Maximum and minimum differences are 6.8 and -7.6 cm in northing, 9.7 and -10.7 in easting, and 15.7 and -21.9 cm in height. The reference coordinates for all stations were determined with 1 cm horizontal and 3 cm vertical accuracy using 3-day static processing with GIPSY software.

For the PPP software, epoch-by-epoch static, processed as simulated ground-based kinematic, test results using three hours of 1 Hz data indicated 3.0 cm standard deviation in North, 3.2 cm in East, and 6.3 cm in Height for GPS station HONE. Mean differences with respect to a known reference position are 4.2 cm in northing, -19.8 cm in easting and 3.4 cm in height for GPS station SORH. Table 2.8 shows the statistics of position estimates in local north, east and height coordinates from the "kinematic", epoch-by-epoch ground based static, processing and a static processing for the GPS station KONG. This table shows a reasonable evaluation of the VRS solution, but the PPP "kinematic" results are still questionable, because of the -17 cm east, and 15 cm height bias. The concluding remark that "simulated ground based kinematic tests results indicate about 3 cm precision" seems to be rather optimistic.

Data/Solution Type	Statistics	North [cm]	East [cm]	Height [cm]
VRS kinematic	Mean	-0.5	-1.0	-3.5
	STD	3.1	3.1	7.8
PPP "kinematic" (station KONG)	Mean	3.6	-17.0	15.7
	STD	2.8	4.8	7.4

Table 2.8: Curtin position differences of VRS kinematic and PPP "kinematic" test results and the reference solution [Castleden et al., 2005].

Researchers at Ohio State University developed and tested the PPP module of their Multi-Purpose GPS Processing Software (MPGPS) in different testing scenarios [Wieglosz et al., 2005]. These testing scenarios included: single-frequency (L1) code and carrier observations (P1 and L1) with the support of an external ionospheric model, and "so-called" ionosphere-free dual-frequency observations (P3 and L3, see section 4.3.2) to

almost totally eliminate the ionospheric effect. They tested three different positioning scenarios/modes: instantaneous (single-epoch P1 solution), kinematic positioning, and static positioning. Table 2.9 provides the accuracy of their kinematic PPP results in terms of the residuals from the "true" position after 1 hour of data accumulation. The GPS data collected by the Ohio station which is part of the network of Continuously Operating Reference Stations (CORS) in Columbus, Ohio, U.S.A. (COLB) on August 31, 2003 were selected. The COLB station is equipped with a Trimble 5700 geodetic GPS receiver with a choke-ring antenna. The data-sampling interval was 30 s. The night session included the data collected during 3-4 pm local time and the daytime session included the data collected during 1-2 pm local time. Table 2.9 shows single-frequency (P1/L1+GIM) and dual-frequency (P3/L3) residuals from 1-hour average position after 1-hour of data accumulation using a kinematic processing technique. GIM stands for the Global Ionosphere Model described in section 4.3.2.2. Values in brackets represent results obtained from night-time observations . Kinematic results were obtained from the same datasets as the static results; the difference is the filter-processing mode.

Kinematic PPP after 1h	P3/L3 Solution	P1/L1+GIM Solution
North Residuals [cm]	-5.0 (-8.0)	25.0 (30.0)
East Residuals [cm]	-6.0 (-5.0)	10.0 (-39.0)
Height Residuals [cm]	-23.0 (-13.0)	-87.0 (-55.0)

Table 2.9: Ohio State University single-frequency and dual-frequency residuals using kinematic processing technique [Wieglosz et al., 2005].

From Table 2.9 it can be concluded that about 3 dm precision in the horizontal

components, and less than 9 dm precision in the vertical component was achieved during the single-frequency test. Table 2.10 presents the precision of the static PPP solution after 1 hour of data accumulation. Values in brackets represent results obtained from night-time observations.

Static PPP after 1h	P3/L3 Solution	P1/L1+GIM Solution
North Residuals [cm]	-14.0 (-20.0)	-18.0 (-8.0)
East Residuals [cm]	-3.0 (-11.0)	-10.0 (-26.0)
Height Residuals [cm]	-1.0 (-25.0)	-3.0 (-6.0)

Table 2.10: Ohio State University single-frequency and dual-frequency residuals using static processing technique [Wieglosz et al., 2005].

From Table 2.10 it can be concluded that about 2 dm precision in horizontal components, and less than 1 dm precision in vertical components was achieved during the single-frequency test. The fact that the daytime results are better than the nighttime results, unlike the results in Table 2.9, is a concern that is not addressed in the paper. A single-frequency kinematic PPP solution plotted in the same paper shows maximum and minimum differences of 5 and -5 cm in north, 15 to -15 cm in east, and 50 and -20 cm in height component in the nighttime. The daytime plot shows 20 to -5 cm variation in north, 15 cm to -25 cm in east, and 40 to -40 cm in height component.

The Geodetic Survey Division of Natural Resources Canada provides an on-line PPP service with data from the Canadian Spatial Reference System (CSRS-PPP) [Tétreault et al., 2005]. Observation sessions varying in duration from tracking stations distributed

globally were processed. The r.m.s. of differences between the estimated and known IGS ITRF 2000 station coordinates were computed, but the paper does not show the individual test results. For the static mode evaluation, the precision was evaluated by processing 24-hour datasets and computing the r.m.s. of coordinate differences with respect to the 24-hour average position. Kinematic results were assessed using stationary GPS data and computing r.m.s. of the coordinate differences with respect to the 30-second-average positions. The kinematic statistics represent a best-case scenario since they neglect some of the real-world effects such as the varying multipath environments encountered by a moving receiver. Table 2.11 shows a summary of the single-frequency and dual-frequency results represented by r.m.s. of coordinate differences with respect to the 24-hour average position using the static processing technique. The convergence time is based on the standard deviations of the estimated parameter and it can take as long as 4 hours for the position component to decrease below the 5 cm-level.

CSRS Static PPP	Iono-Free Solution	Single-Frequency Solution
Latitude r.m.s. [cm]	1	2
Longitude r.m.s. [cm]	1	3
Height r.m.s. [cm]	2	4

Table 2.11: Natural Resources Canada single-frequency and dual-frequency results using a static processing technique [Tétreault et al., 2005].

From Table 2.11 it can be seen that static PPP can achieve centimetre-level precision in horizontal and vertical coordinate from a 24-hour GPS dataset. There are no plots in the paper to graphically represent the results or any information about the mean

differences between the CSRS-PPP estimated positions and the IGS reference positions. Most values in the Table 2.11 and in Table 2.12 have limited precision (one digit) which is not explained and dual-frequency static CSRS-PPP results are three-times better than the best dual-frequency static results presented by Muellerschoen et al., [2004].

CSRS Kinematic PPP	Iono-Free Solution	Single-Frequency Solution
Latitude r.m.s. [cm]	5	25
Longitude r.m.s. [cm]	4	25
Height r.m.s. [cm]	10	50

Table 2.12: Natural Resources Canada single-frequency and dual-frequency results kinematic processing technique [Tétreault et al., 2005].

Table 2.12 shows single-frequency and dual-frequency results represented by r.m.s. of coordinate differences with respect to the 30-min average positions using a kinematic processing technique. In order to validate the capabilities of the CSRS-PPP kinematic positioning comparison with a known reference trajectory would be more meaningful.

The r.m.s. of the coordinate differences with respect to the 30-min average positions show that a few-centimetres horizontal and 10-centimetre vertical position is achievable using dual-frequency data in kinematic mode. The results obtained with single-frequency data are about five times worse than those of dual-frequency data, which is not consistent with the static single frequency and dual frequency positioning results in Table 2.11. A somewhat more realistic indication of the CSRS-PPP kinematic processing capabilities is provided on a 3.80-m-baseline repeatability, computing independent PPP solutions from

each receiver from a 1-Hz data (most likely dual-frequency) during a four-hour flight. The paper [Tétreault et al., 2005] shows a plot with peak-to-peak variations between 3.72 m and 3.97 m with apparent few-centimetre-level discontinuities in the 3.8 m baseline length time series. The plotted time series is only 2.5 hours long.

Single-frequency point positioning results from the University of Calgary researchers [Gao et al., 2006] indicate 0.4 and 0.7 m horizontal accuracy in northing and easting, respectively and 1.4 m in height for a road test in sub-optimal conditions. Presentations at the ION GNSS 2007 [e.g. Leandro et al., 2007] focus on dual-frequency PPP with the emphasis on data analysis and reliable determination of other parameter besides position. There is evidence that the research area of precise kinematic positioning with low-cost receivers is still very active.

The overall state of the art of the precise point positioning shows 5 to 10 cm-level horizontal precision and 15 to 30 cm vertical precision, and 15 to 20 cm horizontal accuracy and 25 to 45 cm vertical accuracy for the static and kinematic dual-frequency point positioning. The precision of the results is represented by a standard deviation and the accuracy is represented by values at 95% probability level. Lower boundaries apply to static applications and upper boundaries apply to kinematic applications. Single-frequency static point positioning results in some cases achieve similar precision and accuracy in horizontal components; however the vertical component precision and accuracy values are at least twice as large as the dual-frequency ones. These results were accomplished with geodetic-quality GPS receivers. There is no comprehensive study on

precise point positioning with low-cost GPS receivers, but there is evidence that one of the early attempts to use low-cost hand-held GPS for sub-metre relative positioning was presented by Lawrence Weil from Magellan Corporation in 1992 [Weil, 1992]. University of Nottingham researchers [Hill et al., 1999] created a software package called GRINGO which is capable of extracting raw data from Garmin hand-held GPS receivers.

2.3 Recent Developments in Spaceborne Point Positioning

The goal of orbit determination is to derive orbital parameter values from observations [Seeber, 1993]. GPS Precise Orbit Determination (POD) is a term for precise orbit determination methods, where GPS, and perhaps some other systems, are used to provide measurements that are used to determine the trajectory of a GPS-equipped satellite. In order to understand the recent developments in spaceborne GPS precise orbit determination, it is beneficial to briefly introduce some of the precise orbit determination strategies. In the following paragraphs the basic principles of dynamic orbit determination, kinematic orbit determination, reduced dynamic orbit determination (hybrid strategy), and geometric orbit determination will be described.

Dynamic orbit determination exploits orbital mechanics and filtering theory to provide an accurate orbit solution from sparse and noisy measurements. In dynamic orbit determination, the orbit model is derived from models of forces acting on a satellite and the laws of motion. The force and satellite models are used to compute a model of

satellite acceleration over time, from which, by double integration, a nominal trajectory is formed [Yunck, 1996]. The dynamic precise orbit determination of a low Earth orbit (LEO) satellite using triple differenced GPS phases is presented in Bae et al. (2007). Using the triple differenced iono-free GPS phase observables, the orbit solution for 24 hours of Challenging Minisatellite Payload (CHAMP) satellite data show the 3D r.m.s. accuracy of 8 cm when compared with the published Rapid Science Orbit.

In the kinematic orbit determination strategy, the conventional dynamic solution produces a reference trajectory and postfit residuals. This is all done in one step in a Kalman filter with additional process noise state parameters, represented by a local force model. This force is estimated to account for the geometric discrepancy between the measurements and the dynamic solution [Yunck, 1996].

The basic premise of the reduced dynamic orbit determination strategy, or hybrid strategy, is to achieve a balance between dynamic and geometric information. This is done by process noise weighting, or more specifically by down-weighting of errors caused by each solution [Yunck, 1996]. Švehla and Rothacher (2003), showed that it is possible to estimate kinematic positions of a LEO satellite with the same level of accuracy (4 - 6 cm 3D r.m.s. w.r.t. SLR) with the widely applied reduced-dynamic or dynamic approaches and kinematic orbit determination strategies.

Geometric orbit determination is a precise orbit determination technique using GPS measurements only; there is no underlying dynamic information required [Bisnath and

Langley, 1999]. Techniques used for the geometric orbit determination include all GPS positioning techniques (single receiver positioning, differential positioning, code measurents only, phase and code measurents, phase measurents only).

GPS measurements from satellites in low Earth orbit experince ionospheric errors from the portion of the ionosphere which is on metre level, depending on the satellite's altitude and the ionospheric activity. The fractional total electron content above the receiver's altitude is obtained from a global ionospheric model and the altitude dependent scale factor [Montenbruck and Gill, 2001]. The effective height for the residual ionosphere is computed using a thin layer approximation. The scale factor can be predicted using a Chapman profile or adjusted as a free parameter of an extended set of single-frequency menasurements. The results applying predicted corrections to the single-frequency pseudorange measuremnts for the CHAMP satellite orbiting at an altitude of 450 km show a significant accuracy gain over uncorrected observations. The systematic radial bias of 3.5 m is removed out of 3.8 m total radial bias presented in the uncorrected solution. The best results were obtained when the CHAMP's C/A code pseudoranges were processed in a reduced dynamic orbit determination. The Kalman filter parameters included 6-dimensional state vetor of the satelite, GPS receiver clock error, 3-dimensional vector of empirical accelerations, and the ionospheric scaling parameter.

Geometric orbit determination was used to determine the orbit of the CHAMP satellite [Bisnath, 2004]. The mathematical formulation of the GPS phase-connected precise point positioning filter used is described in section 3.4.3. The improved quality dataset

processing results show that near decimetre orbit accuracy is attainable when compared to the JPL results obtained with a reduced-dynamic orbit determination strategy. For the CHAMP satellite, the average radial, along track, and cross-track accuracies in terms of r.m.s. for 7 consecutive 24-hour arcs obtained by Bisnath [2004] were 24, 15, and 14 cm, respectively.

The U.S. and French JASON-1 oceanographic mission satellite supports three satellite tracking systems:

1) GPS,
2) Doppler Orbitography and Radiopositioning Integrated by Satellite (DORIS) system, and
3) Satellite Laser Ranging (SLR) [Haines et al., 2003].

Nearly 8 months of GPS data from JASON-1 were processed by JPL using JPL Gipsy/Oasis II software and a reduced dynamic precise orbit determination technique. The independent orbit solutions, University of Texas SLR + DORIS versus JPL GPS solution, agree to within ±2 cm 80% of the time and to within ±1 cm 51% of the time.

The JASON-1 Orbit Comparison Campaign analyses precise orbit solutions from different Associate Analysis Centres (AAC). It is the second campaign run in the framework of the IGS LEO Pilot Project [ESOC, 2003].

The following AAC's have contributed to the JASON-1 orbit campaign:

ASI Agenzia Spaziale Italiana, Matera, Italy

CNES Centre National d'Etudes Spatiales, Toulouse, France

CSR Centre for Space Research, University of Texas, USA

DEOS Delft Institute for Earth Oriented Space Research, The Netherlands

ESOC European Space Operation Centre, Darmstadt, Germany

GFZ Geo Forschungs Zentrum, Potsdam, Germany

GRGS Groupe de Recherche de Géodésie Spatiale, Toulouse, France

JPL Jet Propulsion Laboratory, Pasadena, USA

NCL Newcastle University, UK

IGS LEO JASON-1 precision of all solution types in pairwise comparison ranges from 0.46 cm 3D r.m.s. (GSFC reduced dynamics solution, GPS and GSFC reduced dynamics solution, GPS + SLR) to 3.05 cm 3D r.m.s. (Reduced dynamics solution, GPS and ESOC reduced dynamic solution, DORIS + SLR). The average value of all comparisons is about 2 cm 3D r.m.s. [ESOC, 2003].

One of the recent results [Wu and Bar-Sever, 2006] present sub-centimetre 1D r.m.s. for the real-time estimation of the differential orbit between the two satellites. The two GRACE spacecrafts are separated by a moderately long baseline (about 200 km), and they are of roughly similar shape, which allows differential dynamics to be tightly constrained and strengthen the orbit determination. To the author's knowledge, there are not any recent developments in the area of spaceborne point positioning, but this formation flying application serves as an example of the leading edge of spaceborne GPS application.

2.4 Summary of Recent Developments in Single Point Positioning

This chapter described different strategies for precise orbit determination using GPS. Geometric orbit determination strategy, which relies solely on the GPS measurements, provides better than three decimetre-level accuracy and reduced dynamic orbit determination strategy, which uses a combination of GPS measurements and reference dynamic trajectory provides two centimetre-level accuracy.

Recent developments in ground-based point positioning, described in the this chapter showed a wide range of accuracies from almost few decimetre-level in horizontal components and about metre and half vertical component accuracy for single frequency kinematic to five to ten centimetre-level horizontal accuracies, and two to three decimetre vertical accuracies for dual-frequency static observations. The next chapter will provide an overview of mathematical models used in precise point positioning and their performance.

3 Review of Point Positioning Models

Point positioning filters described in the previous chapter use different mathematical models. Selection of a point positioning filter depends on many aspects of the particular point positioning application. The typical selection criteria depends on the user required accuracy, solution availability and reliability, availability of other positioning and navigation systems, budget restrictions, etc. In order to justify the selection of a specific mathematical model, an overview of commonly used mathematical models is given in this chapter. Each section in this chapter will describe one mathematical model and provide a summary of its performance. The pseudorange-only positioning model represents the lowest accuracy solution. The pseudorange model with between-satellite differences demonstrates the effect of receiver clock parameter elimination. Pseudorange model with sequential least squares solution shows the effect of smoothing in the position domain. Two types of Kalman filter models, pseudorange and undifferenced carrier-phase model and pseudorange and time-differenced carrier-phase model, demonstrate the use of information describing the change of unknown parameters from one epoch to the next. The data from Algonquin IGS station (ALGO) were used in the tests of the three types of filter models described above. The Kalman filter model tests use data from University of New Brunswick IGS station and an aircraft data collected in Greenland. The described models are ordered according to the mathematical complexity starting from the basic pseudorange least-squares model and ending with a complex Kalman-filter-based pseudorange and carrier-phase model.

3.1 Pseudorange Model

The pseudorange-only position model, sometime referred as the navigation solution, is well documented in the Interface Control Document for GPS users [IS-GPS-200D, 2004]. The standard position solution is performed in every GPS receiver and it is shown here as an example of the "lowest accuracy solution".

The linearized filter of the conventional pseudorange observation model is

$$\mathbf{P}_t - \mathbf{P}_t^{\mathbf{0}} = \mathbf{A}_t \boldsymbol{\delta}\mathbf{x}_t + \mathbf{e}_t;\ \mathbf{C}_{\mathbf{P}_t} \tag{3.1}$$

where $\mathbf{P}_t$ and $\mathbf{P}_t^{\mathbf{0}}$ are the pseudorange measurement and predicted value, respectively; $\mathbf{A}_t$ is the measurement design matrix whose elements are the measurement partial derivatives with respect to the receiver position and clock estimates for epoch t; $\boldsymbol{\delta}\mathbf{x}_t$ are the estimated corrections to the receiver position and clock at epoch t; $\mathbf{e}_t$ are the measurement errors associated with $\mathbf{P}_t$; $\mathbf{C}_{\mathbf{P}_t}$ is the covariance matrix for $\mathbf{P}_t$.

The least-squares solution for equation (3.1) is

$$\boldsymbol{\delta}\mathbf{x}_t = -(\mathbf{A}_t^T \mathbf{C}_{\mathbf{P}_t}^{-1} \mathbf{A}_t)^{-1} \mathbf{A}_t^T \mathbf{C}_{\mathbf{P}_t}^{-1} \mathbf{w}_{\mathbf{P}_t} \tag{3.2}$$

where $\hat{\mathbf{x}} = \mathbf{x}^0 + \boldsymbol{\delta}\mathbf{x}$ (the estimate is equal to the approximate initial value plus the estimated correction); $\mathbf{w}_{\mathbf{P}}$ is the misclosure vector for the pseudoranges,:

$$\mathbf{w}_{\mathbf{P}_t} = \mathbf{A}_t \hat{\mathbf{x}}_t - \mathbf{l}_{\mathbf{P}_t} \tag{3.3}$$

where $\mathbf{l}_{\mathbf{P}_t}$ is the measurement vector.

The data from Algonquin IGS station (ALGO) was used in pseudorange-only positioning model, pseudorange model with between-satellite differences and pseudorange model with sequential least squares solution tests. A 24-hour dataset with 30 s sampling interval from July 17, 2004 was used. ALGO is equipped with an AOA BenchMark ACT GPS receiver with the AOAD/M_T choke ring antenna and a hydrogen maser clock. A 10 degree elevation angle cut-off was applied to the data.

The IGS final orbit and clock information, UNB3 tropospheric delay model (Saastamoinen zenith delay tropospheric model, Neill mapping functions, surface met lookup table and height propagators) and global total electron contend (TEC) map ionospheric delay model, were used. Figure 3.1 shows the position differences with respect to the known IGS position. The r.m.s. of the differences are 1.1 m, 0.7 m and 1.9 m in north, east and height components, respectively [Beran et al., 2004]. The north, east and height component errors are higher than those of Le [2004]: 0.5 m, 0.3 and 0.8 m. Please note that some datasets in chapter 3 were collected under different atmospheric conditions with different GPS equipment and environment effects. The standalone positioning models used were identical, but there are differences in tropospheric delay models and elevation cut-off angles. Figure 3.2 shows the least-squares residuals indicating the presence of residual atmospheric delay and unmodeled biases.

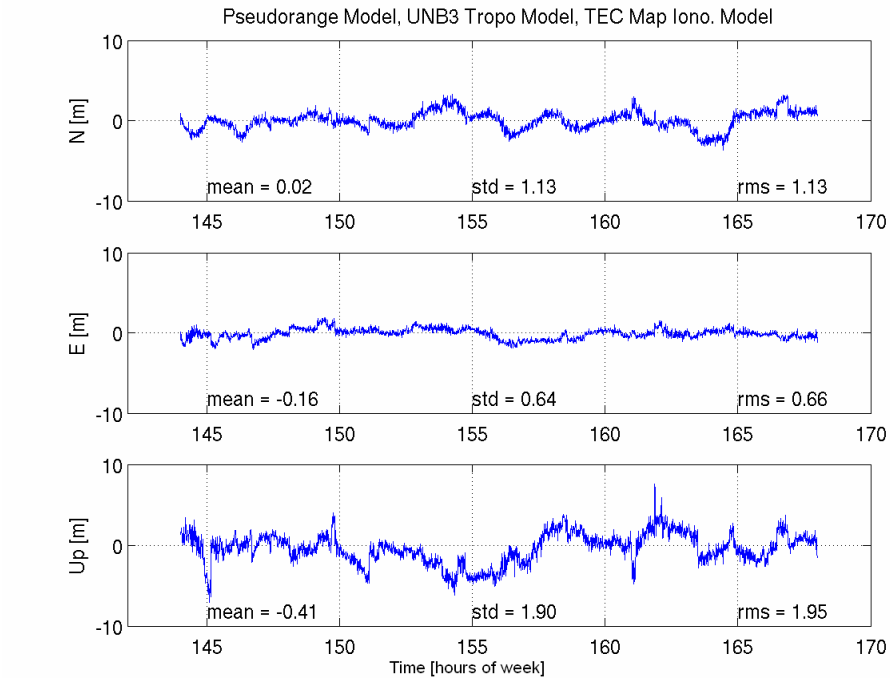

Figure 3.1: Position component and receiver clock errors of the pseudorange model with UNB3 tropospheric delay model and global TEC map ionospheric delay model [Beran et al., 2004].

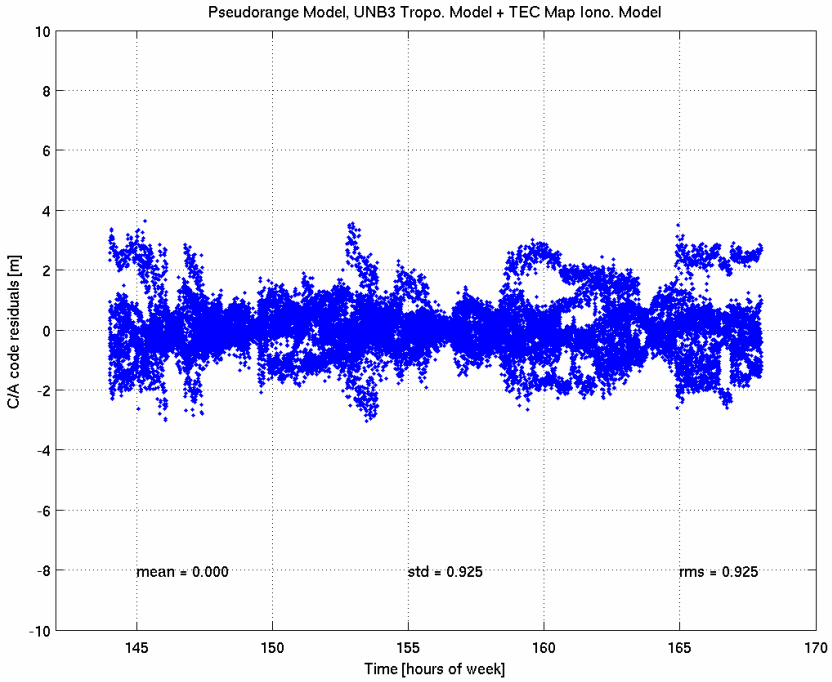

Figure 3.2: Filter residuals from the pseudorange model with UNB3 tropospheric delay model and global TEC map ionospheric delay model from Beran et al. [2004].

3.2 Pseudorange Model with Between-Satellite Differences

Receiver clock error could be removed from the solution by creating between-satellite differences at each epoch. The pseudorange model with between-satellite differences was examined to investigate if the removal of the receiver clock error has any impact on horizontal and vertical position estimates.

The linearized vector–matrix equation of the between satellite filter observation model is

$$\nabla \mathbf{P}_t - \nabla \mathbf{P}_t^{\mathbf{0}} = \nabla \mathbf{A}_t \boldsymbol{\delta} \mathbf{x}_t + \nabla \mathbf{e}_t ;\ \nabla \mathbf{C}_{\mathbf{P}_t} \tag{3.4}$$

where $\nabla \mathbf{P}_t$ and $\nabla \mathbf{P}_t^{\mathbf{0}}$ are the between-satellite differenced pseudorange measurement and predicted value, respectively; $\nabla \mathbf{A}_t$ is the measurement design matrix at epoch t; $\boldsymbol{\delta} \mathbf{x}_t$ are the estimated corrections to the receiver position at epoch t; $\nabla \mathbf{e}_t$ are the measurement errors associated with $\nabla \mathbf{P}_t$; $\nabla \mathbf{C}_{\mathbf{P}_t}$ is the covariance matrix for $\nabla \mathbf{P}_t$.

The solution for equation (3.4) is

$$\boldsymbol{\delta} \mathbf{x}_t = -(\nabla \mathbf{A}_t^T \nabla \mathbf{C}_{\mathbf{P}_t}^{-1} \nabla \mathbf{A}_t^T)^{-1} \nabla \mathbf{A}_t^T \nabla \mathbf{C}_{\mathbf{P}_t}^{-1} \mathbf{w}_{\mathbf{P}_t} \tag{3.5}$$

where $\hat{\mathbf{x}} = \mathbf{x}^0 + \boldsymbol{\delta} \mathbf{x}$.

Using the same data as in section 3.1, Figure 3.3 shows the coordinate differences with respect to the known IGS position. The r.m.s. of the differences are 1.4 m, 0.9 m and 2.6 m in north, east and height components, respectively [Beran et al., 2004]. The r.m.s. of the residuals from this model is 1.22 m.

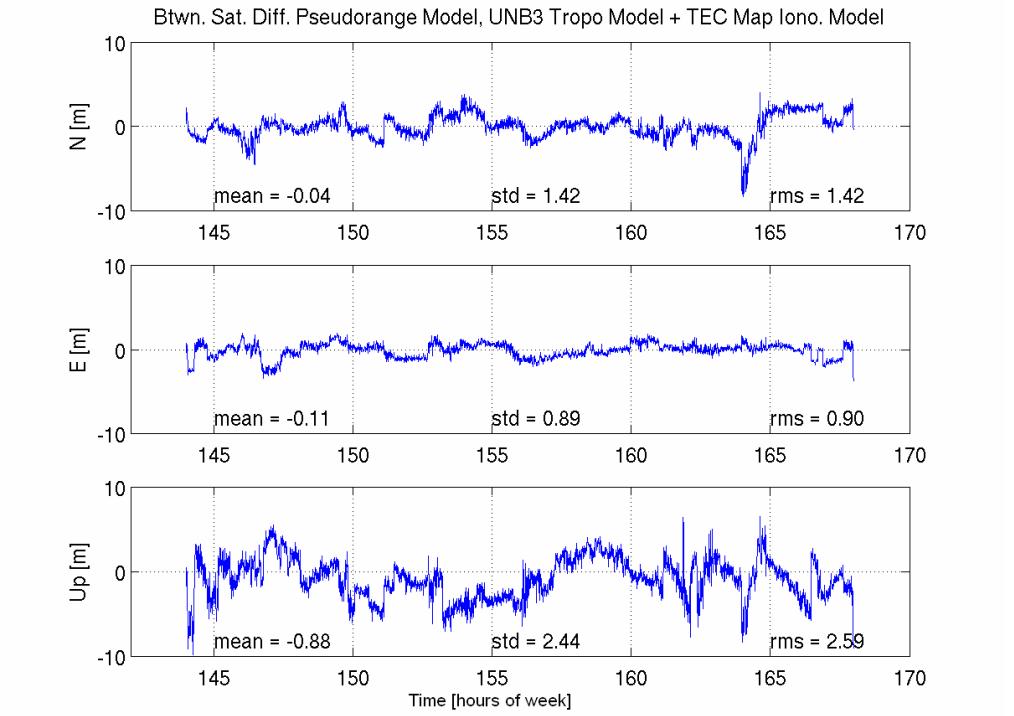

Figure 3.3: Position component and receiver clock errors of the pseudorange model with between-satellite differences from Beran et al., [2004].

Between-satellites differencing results in a decrease of geometrical strength (see e.g., Vaníček et al. [1984]) and a lower number of observations are partially responsible for the results which are less accurate than those of the original pseudorange model. In theory, estimating the receiver clock error as an unknown parameter and removing it by between-satellite differencing should yield the same results. This theory holds true only if

the receiver clock is not correlated with the position components, which is not the case in reality. Perhaps, the main reason that the results obtained in this section are less accurate than those in section 3.1 is that the stochastic model did not account for mathematical correlation in between-satellite differenced observables.

3.3 Pseudorange Model – Weighting Unknown Parameters in the Sequential Least Squares Solution

It is important to keep in mind that all previous models provide epoch-by-epoch independent solutions. The pseudorange model in the sequential least-squares solution takes advantage of the previous epoch estimate and its covariance matrix. It is a form of weighted constraints, or in this case weighting of the unknown parameters [Wells and Krakiwsky, 1971]. The reason why this particular model is presented here is to show the effect of smoothing in the solution domain [Kouba and Héroux, 2001].

The linearized filter observation model in matrix form is the same as that given in (3.1):

$$\mathbf{P}_t - \mathbf{P}_t^{\mathbf{0}} = \mathbf{A}_t \boldsymbol{\delta}\mathbf{x}_t + \mathbf{e}_t;\ \mathbf{C}_{\mathbf{P}_t} \tag{3.6}$$

However, the sequential least squares filter solution for ***(3.6)*** is

$$\boldsymbol{\delta}\mathbf{x}_t = -(\mathbf{C}_{\mathbf{x}^0}{}^{-1} + \mathbf{A}_t^T \mathbf{C}_{\mathbf{P}_t}^{-1} \mathbf{A}_t^T)^{-1} \mathbf{A}_t^T \mathbf{C}_{\mathbf{P}_t}^{-1} \mathbf{w}_{\mathbf{P}_t}$$

$$\mathbf{C}_{\mathbf{x}^0} = \mathbf{C}_{\hat{\mathbf{x}}_{t-1}} + \mathbf{C}_{\varepsilon_{\Delta t}} \tag{3.7}$$

where $\hat{\mathbf{x}} = \mathbf{x}^0 + \boldsymbol{\delta}\mathbf{x}$; $\mathbf{w}_{\mathbf{P}}$ is the misclosure vector for the pseudoranges; and $\mathbf{C}_{\hat{\mathbf{x}}_{t-1}}$ is the

receiver position and clock covariance based on the last epoch's solution; $\mathbf{C}_{\varepsilon_{\Delta t}}$ is the process noise covariance matrix reflecting the between-epoch position change.

The process noise covariance matrix plays an important role in this type of filter. Unlike the Kalman filter process noise covariance matrix, the $\mathbf{C}_{\varepsilon_{\Delta t}}$ matrix in this filter actually dictates how much the unknown parameters could change between epochs. Choosing numerically small values for position component variances means that the filter assumes very little or no dynamics (appropriate for static positioning) and choosing numerically large values will result in an epoch-by-epoch independent (or kinematic) solution. Optimal results could be obtained by forward and backward runs of this filter and/or by some a-priori knowledge of the GPS receiver dynamics.

The pseudorange model with a sequential least-squares solution produces results which are smoother (standard deviations of the horizontal and vertical components are 1 dm and 2 dm smaller, respectively than those in section 3.1). The filtering in the solution domain depends to a large extent on the matrix reflecting the between-epoch position and receiver clock change. Process noise variance for position components was 10^{-2}m^2/epoch and 10^{-8} m^2/epoch for the receiver clock error estimates. The process noise variance for position components represents a decimetre-level position change between epochs, which means that unlike in [Kouba and Héroux, 2001] there are no static constraints used in the filter. The receiver clock process noise variance is about ten orders of magnitude larger than the short-term stability of the station hydrogen maser atomic clock so the clock term can absorb a portion of unmodeled atmospheric biases. Typical

Allan variance parameters for various timing standards used in GPS are on the order of 10^{-20} m^2/epoch. More information about noise variances could be found in Brown and Hwang, [1992].

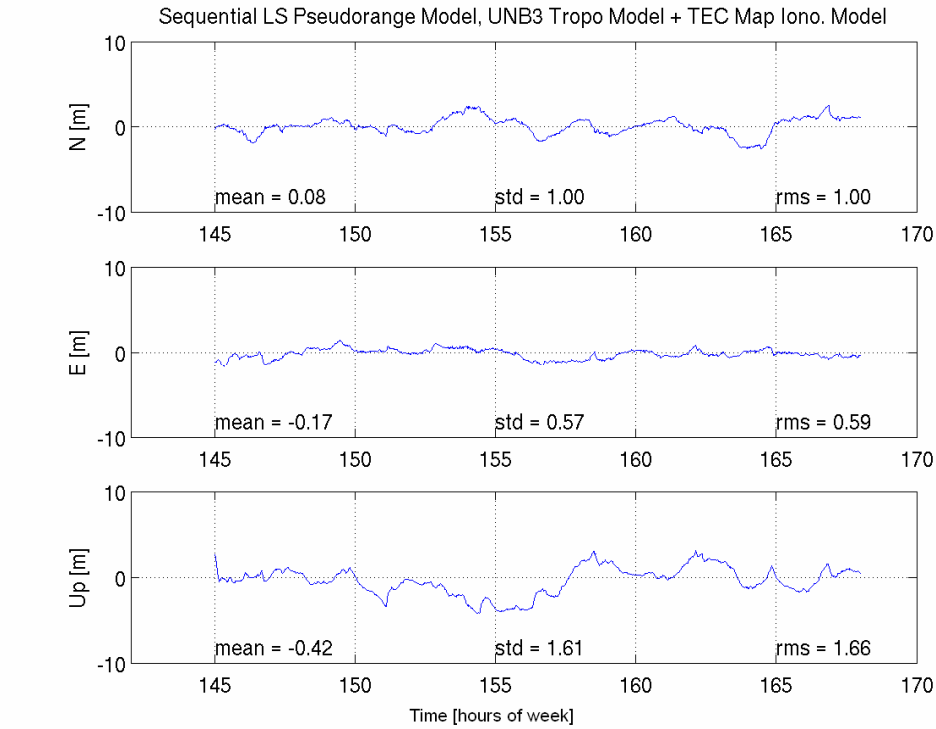

Figure 3.4: Position component and receiver clock errors of the pseudorange model with the sequential least-squares solution without the initial convergence period from Beran et al., [2004].

Using the same data as in section 3.1, Figure 3.4 shows the coordinate differences with respect to the known IGS position. The r.m.s. of the differences are 1.0 m, 0.6 m and 1.7 m in north, east and height components, respectively [Beran et al., 2004]. The r.m.s. of the residuals from this model is 0.96 m.

Functional Model	3D Bias [m]	r.m.s. of the code (and phase) residuals [m]
Pseudorange model with. btwn. sat. diff.	0.89	1.22
Pseudorange model	0.44	0.93
Sequential LS solution	0.55	0.96
Pseudorange and time-diff. carrier-phase model	0.76	0.66 (0.001)

Table 3.1: 3D bias and r.m.s. of residuals of different functional and stochastic models without the initial convergence period from Beran et al., [2004].

The use of different functional and stochastic models are summarized in Table 3.1. The pseudorange model, the pseudorange model with between-satellite differences, the sequential least-squares solution and the pseudorange and time-differenced carrier-phase 3D bias and r.m.s. are used in the comparison. In conclusion, the receiver clock error estimation model (section 3.1) is mathematically equivalent to the receiver clock error removal by between-satellite differencing under conditions described in section 3.2. The preference is given to the receiver clock error estimation model, because of preservation of the geometrical strength [Vaníček et al., 1984]. There is some advantage in the sequential least-squares solution presented in section 3.3, over the epoch-by-epoch solutions presented in sections 3.1 and 3.2. Use of pseudorange with time-differenced carrier-phase observation combines the strengths of the receiver clock error estimation model and the sequential least-squares solution. The sequential processing philosophy is further investigated in the next sections dedicated to the Kalman filter models.

3.4 Kalman Filter Models

The sequential least-squares technique is a subset of the Kalman filter (e.g. Bisnath [2004]). The Kalman filter is usually used in a variety of estimation processes, because it utilizes all measurements up to the current epoch (sequential least squares) and dynamic information that describes the change of unknown parameters from one epoch to the next. Single frequency pseudorange and carrier-phase measurements are combined in the Kalman filter in a way that would optimize the use of information content of both types of observables, the absolute but noisy pseudoranges and the precise but ambiguous carrier-phase measurements. Knowledge of the dynamic information is required for all unknown parameters, which are further referred to as the system state parameters or simply the system state. This section starts with the general description of the Kalman filter model. Section 3.4.1 will provide some background on the receiver clock error dynamic model and sections 3.4.2 and 3.4.3 will demonstrate the use of different dynamic models for different positioning problems.

The discrete Kalman filter system model (dynamic model) is given by:

$$\mathbf{x}_k = \mathbf{\Phi}_{k,k-1}\mathbf{x}_{k-1} + \mathbf{w}_{k,k-1},\ \mathbf{w}_{k,k-1} \sim N(\mathbf{0}, \mathbf{Q}_{k,k-1}), \tag{3.8}$$

where $\mathbf{x}_k$ is the system state at time t_k; $\mathbf{\Phi}_{k,k-1}$ is the system transition matrix which relates the state at time t_{k-1} to the state at time t_k. The system transition matrix is derived from a set of differential equations describing the system dynamics. $\mathbf{w}_{k,k-1}$ is the system noise vector. $\mathbf{Q}_{k,k-1}$ is the process noise variance-covariance matrix which describes the

uncertainty in the dynamic model. This uncertainty is usually described using the autocorrelation function of the unknown parameters, in this case the system state vector. The purpose of the process noise variance covariance matrix is to define the variation of unknown parameters in time. Three random models are frequently used in GPS data processing: white noise, random walk and an exponentially correlated model [Borre and Strang, 1997].

The Kalman filter measurement model is given by:

$$\mathbf{z}_k = \mathbf{H}_k \mathbf{x}_k + \mathbf{v}_k,\ \mathbf{v}_k \sim N(\mathbf{0}, \mathbf{R}_k), \tag{3.9}$$

where $\mathbf{z}_k$ is the measurement vector; $\mathbf{H}_k$ is the linearized system design matrix; i.e. the matrix of partial derivatives of the measurements with respect to each of the state variables; and $\mathbf{v}_k$ is the measurement noise vector. $\mathbf{R}_k$ is the measurement noise variance-covariance matrix. The complete set of discrete Kalman filter equations and their solutions can be found in Gelb [1974].

To avoid iteration in the solution, the extended Kalman filter is usually employed. In the extended Kalman filter, linearization takes place about the filter's best estimate of the state. The degree to which the user dynamics are constrained or predictable dictates the type of process model used. A GPS receiver clock process model and dynamic platform process models will be described in the following sections.

3.4.1 Receiver Clock Model

The inexpensive clock in most receivers makes GPS navigation practical, but introduces an additional unknown parameter: instantaneous receiver clock offset bias or bias relative to the GPS (System) Time [Misra, 1996]. Typical behaviour of several kinds of receiver clocks including an atomic cesium beam oscillator, an atomic rubidium vapour-cell oscillator, an oven controlled crystal oscillator (OCXO), and temperature-compensated crystal oscillator (TXCO) has been discussed by Misra [1996]. The differences between the type of clock in a geodetic-quality GPS receiver and low-cost GPS receiver is described in section 4.6.

The Kalman filter approach considers a clock with a precisely predictable offset at any instant relative to GPS Time. Two state parameters, which represent the phase and frequency errors in a GPS receiver, are required in any GPS-based estimator [Axelrad and Brown, 1996]. This model says that we expect both the frequency and phase to random walk over a short period of time. The discrete process equations are given by:

$$\mathbf{x}_{ck} = \mathbf{\Phi}_{ck,k-1}\mathbf{x}_{ck-1} + \mathbf{w}_{ck,k-1} \tag{3.10}$$

where:

$$\mathbf{x}_{c_{k-1}} = \begin{bmatrix} dt \\ \dot{dt} \end{bmatrix}, \mathbf{\Phi}_{ck,k-1} = \begin{bmatrix} 1 & \Delta t \\ 0 & 1 \end{bmatrix},$$

$$\mathbf{Q}_{ck,k-1} = E[\mathbf{w}_c \mathbf{w}_c^T] = \begin{bmatrix} S_{dt}\Delta t + S_{\dot{dt}}\dfrac{\Delta t^3}{3} & S_{\dot{dt}}\dfrac{\Delta t^2}{2} \\ S_{\dot{dt}}\dfrac{\Delta t^2}{2} & S_{\dot{dt}}\Delta t \end{bmatrix}. \tag{3.10*}$$

The nomenclature is the same as in the previous section. The process noise variance matrix $\mathbf{Q}_{ck,k-1}$ represents the uncertainty associated with the receiver clock prediction. The white noise spectral amplitudes S_{dt} = $2*10^{-19}$m^2/epoch and S_{di} = $8\pi^2*7*10^{-21}$m^2/epoch were determined from the Allan variance parameters of the two-state clock model [Brown and Hwang, 1992]. For the studies presented here, spectral amplitudes S_{dt} and S_{di} were chosen to represent an uncontrolled crystal oscillator because use the Kalman filter will converge even if higher quality receiver clock is used. If the spectral amplitudes used in the filter are lower than those represented the actual receiver clock the filter convergence may not be accomplished.

This section described the mathematical model with two state parameters, which represents the phase and frequency errors in a GPS receiver and the uncertainty associated with the unknown state parameters. The same principle, and in-depth-knowledge, is required for all unknown parameters estimated in the Kalman filter. The following two sections describe two different cases of the receiver dynamics, the static case represented by the pseudorange and carrier-phase model, sub-section 3.4.2, and the near-constant-acceleration-case represented by the pseudorange and time-differenced carrier-phase model, section 3.4.3.

3.4.2 Pseudorange and Carrier-Phase Model

A pseudorange and carrier-phase model has been investigated [Beran et al., 2003]. Absence of a velocity observable in this system makes it more suitable for static positioning applications. In this case, receiver position and receiver clock terms must be estimated together with other nuisance parameters such as carrier-phase ambiguities and zenith ionospheric delays (in the case when dual-frequency measurements are not available). If kinematic GPS data were processed with this type of filter, the uncertainty in the position state parameters' prediction (the system noise matrix) would have to be large enough to accommodate changes in position. Uncertain state parameters cause large innovation ("innovation" is observed minus predicted measurement) values and therefore less smoothing in the filter.

The corresponding dynamic model is given by the following equation:

$$\mathbf{x}_{S_k} = \mathbf{\Phi}_{S_{k,k-1}} \mathbf{x}_{S_{k-1}} + \mathbf{w}_{S_{k,k-1}} \tag{3.11}$$

where:

$$\mathbf{x}_S = [x \quad y \quad z \quad N_1 \quad ... \quad N_n \quad dt \quad \dot{dt} \quad d_{ion} \quad \dot{d}_{ion}]^T$$

$\mathbf{x}_S$ is the system state vector which includes position, ambiguities for n satellites, receiver clock parameters and ionospheric delay parameters. The corresponding system transition matrix follows:

$$\mathbf{\Phi}_{S_{k,k-1}} = \begin{bmatrix} \mathbf{I} & & \\ & \mathbf{\Phi}_{ck,k-1} & \\ & & \mathbf{\Phi}_{ik,k-1} \end{bmatrix} \tag{3.12}$$

with $\mathbf{I} = (3+n)$ x $(3+n)$ identity matrix, where n is the number of satellites; and $\mathbf{\Phi}_{ik,k-1} = \mathbf{\Phi}_{ck,k-1}$. The system noise covariance matrix is:

$$\mathbf{Q}_{Sk,k-1} = E[\mathbf{w}_S \mathbf{w}_S{}^T] = \begin{bmatrix} (S_p \Delta t) \cdot \mathbf{I}_p & & & \\ & (S_a \Delta t) \cdot \mathbf{I}_a & & \\ & & \mathbf{Q}_c & \\ & & & \mathbf{Q}_i \end{bmatrix} \tag{3.13}$$

where $\mathbf{I}_p = (3 \text{ x } 3)$ identity matrix, $\mathbf{I}_a = (n \text{ x } n)$ identity matrix and

$$\mathbf{Q}_{ik,k-1} = \begin{bmatrix} S_i \frac{\Delta t^3}{3} & S_i \frac{\Delta t^2}{2} \\ S_i \frac{\Delta t^2}{2} & S_i \Delta t \end{bmatrix} \tag{3.14}$$

where S_p represents the spectral amplitude for the position random process. S_p for a static observer should theoretically be set to zero (random bias model), but this may inherently cause numerical problems. This could be the result of the error covariance matrix converging to zero, when the filter deals with infinitesimally small numbers after a prolonged duration of processing. A value, which maximizes the smoothing of the position component estimates is used (random walk model). The same theory could be applied to the dynamic model of the ambiguity parameters. Instead of treating carrier-phase ambiguities as constants, the spectral amplitude for the ambiguity random process, $S_a = 1*10^{-3}$ m^2/epoch, is set to a value which allows ambiguities to absorb some of the unmodeled biases, such as residual atmospheric biases and multipath effects. The actual numerical value of the spectral amplitude for the ambiguity random process was determined empirically with a rate of 0.17 m/s. Smaller value causes long convergence time after a millisecond jump [Beran et al., 2003]. $S_i = (4/60*dt)^2$ m^2/epoch represents the spectral amplitude of the zenith ionospheric delay integrated random walk model,

where dt is the data sampling interval. The spectral amplitude of the zenith ionospheric delay represents random changes in ionospheric delays of 0.25 m/min. Periods of moderate to active solar activities require larger values, e.g. 1.0 m/min [Goad, 1990].

The pseudorange and carrier-phase measurement model follows the form of (3.9):

$$\mathbf{z}_{sk} = \mathbf{H}_{sk}\mathbf{x}_{sk} + \mathbf{v}_{sk} \tag{3.15}$$

where:

$$\mathbf{z}_{sk}{}^{i} = \begin{bmatrix} \mathbf{P}^{i} - \mathbf{P}^{i}{}_{o} \\ \mathbf{\Phi}^{i} - \mathbf{\Phi}^{i}{}_{0} \end{bmatrix},$$

$\mathbf{P}^{i} - \mathbf{P}^{i}{}_{o}$ are observed minus computed pseudoranges and $\mathbf{\Phi}^{i} - \mathbf{\Phi}^{i}{}_{0}$ are observed minus computed carrier-phases

$$\mathbf{H}_{sk}{}^{i} = \begin{bmatrix} h_x{}^{i} & h_y{}^{i} & h_z{}^{i} & 0 & \ldots & 0 & 1 & 0 & F(E) & 0 \\ h_x{}^{i} & h_y{}^{i} & h_z{}^{i} & 1 & \ldots & 0 & 1 & 0 & -F(E) & 0 \end{bmatrix}, \tag{3.16}$$

$h_x{}^{i}, h_y{}^{i}, h_z{}^{i}$ are the measurement partial derivatives with respect to the receiver position; *F(E)* are the broadcast model ionospheric delay mapping functions [IS-GPS-200D, 2004];

$$\mathbf{v}_{sk} = \begin{bmatrix} e_P{}^{i} \\ \varepsilon_{\Phi}{}^{i} \end{bmatrix}, \tag{3.17}$$

and $e_P{}^{i}$ and $\varepsilon_{\Phi}{}^{i}$ are the measurement errors associated with $\mathbf{P}^{i}$ and $\mathbf{\Phi}^{i}$, respectively.

The pseudorange and carrier-phase filter was tested on a randomly selected one hour of observations collected on 20 July 2002 by the University of New Brunswick (UNB)

IGS station, located on the roof of the Head Hall building on the Fredericton campus (IGS station identifier UNB1). UNB1 used a Javad Legacy receiver equipped with a dual-depth choke-ring antenna and it was used to collect 30 s sampling interval data with a 5° elevation mask angle. IGS orbit and clock were used. Reference coordinates of the antenna phase center are known from the IGS data processing. Only L1 single-frequency measurements were used in the processing. The r.m.s. of the differences with respect to the known IGS position, after the filter reached a steady state, are 1.0 m, 0.6 m and 0.7 m in north, east and height component. The results of the processing are presented in Figure 3.5. The north, east and height component error values were computed by differencing the estimated position from the reference IGS coordinates of the antenna. Summary statistics for this dataset are given in Table 3.2. The statistics include the results from the filter's initial convergence period and the convergence period after the millisecond jump just before the hour 165.4. There was no quality control algorithm built into the software at this time, and potential cycle slips may be present in the data.

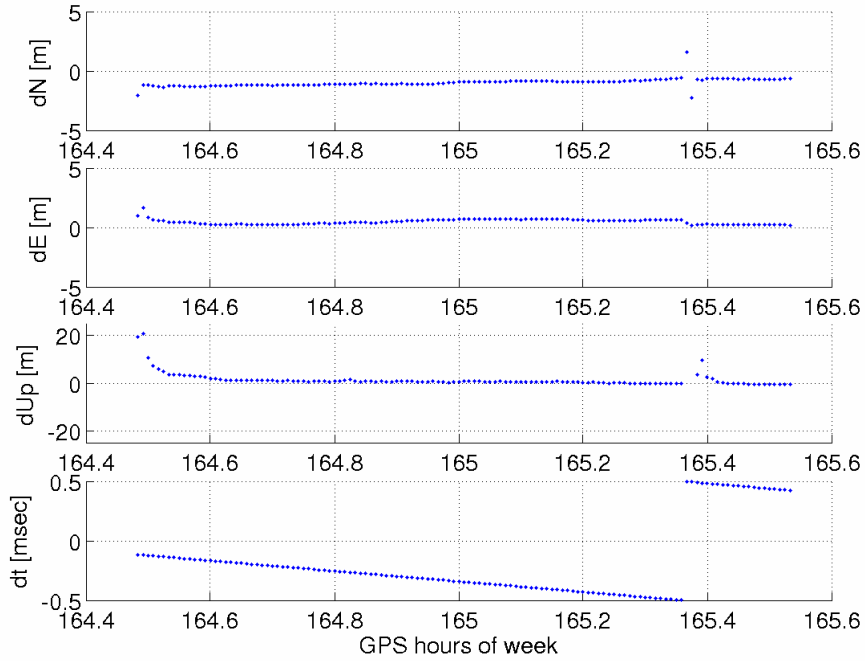

Figure 3.5: Position component differences and receiver clock bias estimates for pseudorange and carrier-phase filter on a high-quality static dataset from Beran, et al., [2003].

Position Error Components [cm]			
	North	East	Height
Mean	101.0	51.0	61.0
Std. Dev.	15.0	17.0	43.0
r.m.s.	102.0	55.0	75.0

Table 3.2: Summary statistics of steady-state component errors for pseudorange and carrier-phase filter from Beran, et al., [2003].

3.4.3 Pseudorange and Time-Differenced Carrier-Phase Model

A low-dynamic system model is more suitable for platforms with near-constant or zero accelerations, such as cars or boats [Beran, et al., 2003]. Time-differencing of carrier-phase measurements eliminates the carrier-phase ambiguity parameters and provides a velocity observable to the filter. The corresponding dynamic model is given by the following:

$$\mathbf{x}_{Lk} = \mathbf{\Phi}_{Lk,k-1}\mathbf{x}_{Lk-1} + \mathbf{w}_{Lk-1} \tag{3.18}$$

where:

$$\mathbf{x}_L = [x \quad y \quad z \quad \dot{x} \quad \dot{y} \quad \dot{z} \quad dt \quad d\dot{t}]^T$$

$\mathbf{x}_L$ includes the user position, velocity and receiver clock terms. The corresponding system transition matrix follows:

$$\mathbf{\Phi}_{Lk,k-1} = \begin{bmatrix} \mathbf{I} & \Delta t \cdot \mathbf{I} & 0 \\ 0 & \mathbf{I} & 0 \\ 0 & 0 & \mathbf{\Phi}_{ck,k-1} \end{bmatrix} \tag{3.19}$$

with ***I*** a 3 x 3 identity matrix. The system noise matrix is:

$$\mathbf{Q}_{Lk,k-1} = E[\mathbf{w}_L \mathbf{w}_l^T] = \begin{bmatrix} (S_p \frac{\Delta t^3}{3}) \cdot \mathbf{I} & (S_p \frac{\Delta t^2}{2}) \cdot \mathbf{I} & 0 \\ (S_p \frac{\Delta t^2}{2}) \cdot \mathbf{I} & (S_p \Delta t) \cdot \mathbf{I} & 0 \\ 0 & 0 & \mathbf{Q}_c \end{bmatrix} \tag{3.20}$$

The spectral amplitude of the position and velocity integrated random-walk model,

S_p, is set in the same way as in the pseudorange and carrier-phase model (sub-section 3.4.2). If the dynamical uncertainty of the vehicle is large, filtering would not improve the navigation solution. The process noise parameters of $S_p = 1*10^5$ m^2/epoch were chosen to reflect the vehicle dynamics (see below) and to obtain an optimal solution.

The pseudorange and time-differenced carrier-phase measurement model follows:

$$\mathbf{z}_{Lk} = \mathbf{H}_{Lk}\mathbf{x}_{Lk} + \mathbf{v}_{Lk} \tag{3.21}$$

where:

$$\mathbf{z}_{Lk}{}^{i} = \begin{bmatrix} \mathbf{P}^i - \mathbf{P}^i{}_o \\ \delta\mathbf{\Phi}^i - \delta\mathbf{\Phi}^i{}_0 \end{bmatrix},$$

$\mathbf{P}^i - \mathbf{P}^i{}_o$ are observed minus computed pseudorange measurements and $\delta\mathbf{\Phi}^i - \delta\mathbf{\Phi}^i{}_0$ are observed minus computed time-differenced carrier-phase measurements.

$$\mathbf{H}_{sk}{}^{i} = \begin{bmatrix} h_x{}^i & h_y{}^i & h_z{}^i & 0 & 0 & 0 & 1 & 0 \\ 0 & 0 & 0 & h_x{}^i & h_y{}^i & h_z{}^i & 0 & 1 \end{bmatrix}, \tag{3.22}$$

$h_x{}^i, h_y{}^i, h_z{}^i$ are the measurement partial derivatives with respect to the receiver position.

$$\mathbf{v}_{sk} = \begin{bmatrix} e_P{}^i \\ \varepsilon_{\delta\Phi}{}^i \end{bmatrix}, \tag{3.23}$$

and $e_P{}^i$ and $\varepsilon_{\delta\Phi}{}^i$ are the measurement errors associated with $\mathbf{P}^i$ and $\delta\mathbf{\Phi}^i$, respectively.

Data from a GPS receiver on an airplane were used to illustrate the performance of the pseudorange and time-differenced carrier-phase model on a kinematic dataset. In this

specific case, the GPS receiver platform experienced higher accelerations than those to be expected of a boat or car. The data was collected by Kort & Matrikelstyrensen (KMS) in Greenland using a Trimble 4000 SSI receiver on 22 August 2000. Data sampling interval was 1 second and the elevation angle cutoff was 0°. The selected 15 min section of the data represents the aircraft's runway movements and the take-off maneuver. The reference solution was obtained with the Trimble Geomatics Office GPS software package using a dual-frequency kinematic baseline processing technique.

The broadcast ionospheric delay model and associated parameter values (Klobuchar model) were used in the point positioning filter. IGS orbit and clock were used. This model reportedly corrects for at least 50% (r.m.s.) of the ionospheric delay [Klobuchar, 1996]. The r.m.s. of the differences with respect to the known trajectory, after the filter reached a steady state, are 0.4 m, 1.5 m and 1.0 m in north, east and height component, respectively [Beran et al., 2003]. The results of the processing are presented in Figure 3.6. The north, east and height component error values were computed by differencing the estimated position from the reference solution,. Summary statistics for this dataset are given in Table 3.3.

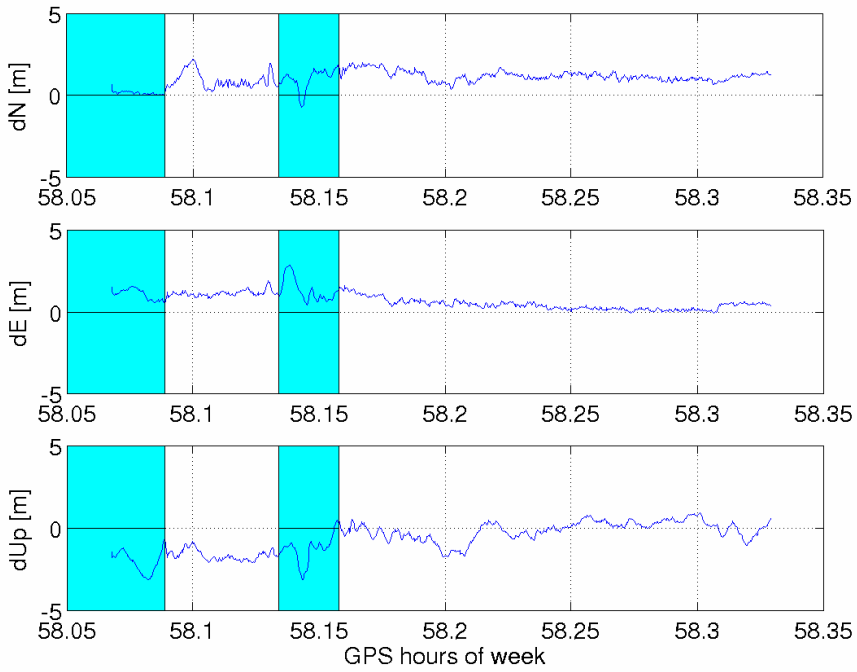

Figure 3.6: Position component differences for pseudorange and time-differenced carrier-phase filter on a kinematic dataset. The first blue-highlighted region represents the time when the aircraft is stationary and the second one represents the time when it is performing the take-off roll from Beran, et al., [2003].

Position Error Components [cm]			
	North	East	Height
Mean	18.0	137.0	-23.0
Std. Dev.	36.0	51.0	98.0
r.m.s.	40.0	147.0	101.0

Table 3.3: Summary statistics of steady-state component errors for pseudorange and carrier-phase filter from Beran, et al., [2003].

3.5 Review of Point Positioning Models - Summary

In theory the results obtained with Kalman-filter-based point positioning processors should be equivalent or superior to those of the sequential least-squares, if the additional information about the platform dynamics is accurate. Kalman-filter-based point positioning processors tested in sub-sections 3.4.2 and 3.4.3, support the above statement, but it is difficult to draw more conclusions because of the limited amount of test data (collected with different receivers under different atmospheric conditions), different handling of ionospheric delays, different elevation cut-off angle, etc. The purpose of this dissertation was to design a point positioning filter suitable for low-cost GPS receiver data processing. The filter had to be first evaluated on ground-based static and kinematic datasets and it can be also tested on spaceborne data. This generalization means that the information regarding receiver dynamics, and the uncertainty associated with this dynamic information, will be different. The options in the Kalman filter design are:

(1) design multiple filters for each processing scenario,

(2) select one type of filter dynamics and achieve sub-optimal results in cases when the actual dynamics are different from the one assumed by the filter, or

(3) simplify the Kalman filter design and use a different processing technique which obtains the dynamic information directly from the measurements themselves.

The pseudorange and time-differenced carrier-phase filter, which satisfies the third option in the Kalman filter design, will be described in detail in the next chapter.

4 Pseudorange and Time-Differenced Carrier-Phase Filter Model

The previous chapter reviewed mathematical models that are used in the point positioning filters. Recommendations from the previous chapter are: (1) to utilize the information from single-frequency pseudorange and carrier-phase observables in a sequential least-squares filter, (2) to design a filter which is suitable for positioning of spaceborne platforms equipped with low-cost GPS receivers as well as positioning of ground-based static and kinematic platforms with similar receivers. The pseudorange and time-differenced carrier-phase model fulfils these requirements and therefore was selected for further testing in the research reported in this dissertation.

It is important to emphasize that the high-accuracy point positioning methods, including this one, are based on availability of precise and accurate GPS satellite coordinates and satellite clock error estimates, and additional mathematical models to remove systematic effects affecting the estimated parameters are used [Tétreault et al., 2005]. This chapter will establish the mathematical model in section 4.1. Description of IGS orbit and clock products and point positioning correction models will be given in section 4.2, followed by the investigation of atmospheric effects in section 4.3. Investigation of models and methods to mitigate the effect of ionospheric delay is an essential part of this dissertation so the sub-sections 4.3.2.1 to 4.3.2.4 are dedicated to the different methods used in this research. Additional problems like cycle-slip detection, multipath mitigation, receiver hardware differences, and residual outlier detection are described in sections 4.4, 4.5, 4.6, and 4.7 respectively. The differential code bias (DCB)

also called inter-frequency bias is taken into account. Depending on the section of the pseudorange observation (C1 or P1) the software applies the appropriate correction. The difference in the resulting positioning accuracy can reach the two decimetre-level in the vertical component.

4.1 Mathematical Formulation of Pseudorange and Time-Differenced Carrier-Phase Filter

The filter provides a fusion of low-precision pseudorange data with the two orders of magnitude more precise time-differenced carrier-phase data. Time-differenced carrier-phase data also provide a connection between measurement epochs, so the actual velocity measurements (time-differenced carrier-phases) provide the dynamic information to the filter [Bisnath and Langley, 2002].

Figure 4.1 illustrates the sequential least-squares processing using the pseudorange and time-differenced carrier-phase filter. The filter generates a pseudorange solution and its variance-covariance matrix at epoch *t-1*. The solution at epoch *t* is obtained using the pseudoranges at epoch *t* and carrier-phase differences between epoch *t* and *t-1* and the solution, and its variance covariance matrix, from the previous epoch. The solution at epoch *t* creates a constraint for the next epoch solution and the process is repeated. As time progresses the solution variances are getting smaller and the filter converges.

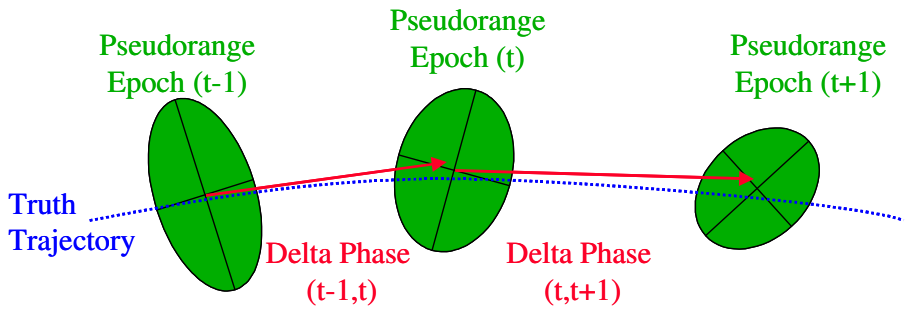

Figure 4.1: Pseudorange and Time-Differenced Carrier-Phase Sequential Least-Squares Filter.

The linearized pseudorange and time-differenced carrier-phase filter observation model in hypermatrix form is

$$\begin{bmatrix} \mathbf{P}_t - \mathbf{P}_t^0 \\ \boldsymbol{\delta\Phi}_{t-1,t} - \boldsymbol{\delta\Phi}^0_{t-1,t} \end{bmatrix} = \begin{bmatrix} 0 & \mathbf{A}_t \\ -\mathbf{A}_{t-1} & \mathbf{A}_t \end{bmatrix} \begin{bmatrix} \boldsymbol{\delta x}_{t-1} \\ \boldsymbol{\delta x}_t \end{bmatrix} + \begin{bmatrix} \mathbf{e}_t \\ \boldsymbol{\varepsilon}_{t-1,t} \end{bmatrix}; \; \mathbf{C}_{\mathbf{P}_t}, \; \mathbf{C}_{\boldsymbol{\delta\Phi}_{t-1,t}}, \qquad (4.1)$$

where $\mathbf{P}_t$ and $\mathbf{P}_t^0$ are the pseudorange measurement and predicted value, respectively; $\boldsymbol{\delta\Phi}_{t-1,t}$ and $\boldsymbol{\delta\Phi}^0_{t-1,t}$ are the time-differenced carrier-phase measurement and predicted value, respectively; $\boldsymbol{\delta x}_{t-1}$ and $\boldsymbol{\delta x}_t$ are the estimated corrections to the receiver position and clock at epochs t-1 and t, respectively; $\mathbf{A}_{t-1}$ and $\mathbf{A}_t$ are the measurement design matrices for epochs t-1 and t, respectively; $\mathbf{e}_t$ and $\boldsymbol{\varepsilon}_{t-1,t}$ are the measurement errors associated with $\mathbf{P}_t$ and $\boldsymbol{\delta\Phi}_t$, respectively; $\mathbf{C}_{\mathbf{P}_t}$ and $\mathbf{C}_{\boldsymbol{\delta\Phi}_{t-1,t}}$ are the covariance matrices for $\mathbf{P}_t$ and $\boldsymbol{\delta\Phi}_{t-1,t}$, respectively. Mathematical correlation in the time-differenced carrier-phase measurement is taken into account applying the law of propagation of variances [Hofmann-Wellenhof et al., 2001].

The best solution for (4.1), in a least-squares sense, is

$$\begin{bmatrix} \hat{\mathbf{x}}_{t-1} \\ \hat{\mathbf{x}}_{t} \end{bmatrix} = \begin{bmatrix} \mathbf{x}_{t-1}^{0} \\ \mathbf{x}_{t}^{0} \end{bmatrix} - \begin{bmatrix} \mathbf{A}_{t-1}^{T}\mathbf{C}_{\delta\Phi_{t-1,t}}^{-1}\mathbf{A}_{t-1} + \mathbf{C}_{\hat{\mathbf{x}}_{t-1}}^{-1} & -\mathbf{A}_{t-1}^{T}\mathbf{C}_{\delta\Phi_{t-1,t}}^{-1}\mathbf{A}_{t} \\ -\mathbf{A}_{t}^{T}\mathbf{C}_{\delta\Phi_{t-1,t}}^{-1}\mathbf{A}_{t-1} & \mathbf{A}_{t}^{T}\left(\mathbf{C}_{\mathbf{p}_t}^{-1} + \mathbf{C}_{\delta\Phi_{t-1,t}}^{-1}\right)\mathbf{A}_{t} \end{bmatrix} \times \begin{bmatrix} -\mathbf{A}_{t-1}^{T}\mathbf{C}_{\delta\Phi_{t-1,t}}^{-1}\mathbf{w}_{\delta\Phi} \\ \mathbf{A}_{t}^{T}\mathbf{C}_{\mathbf{P}_t}^{-1}\mathbf{w}_{\mathbf{P}} + \mathbf{A}_{t}\mathbf{C}_{\delta\Phi_{t-1,t}}^{-1}\mathbf{w}_{\delta\Phi} \end{bmatrix} \tag{4.2}$$

where $\mathbf{w}_{\mathbf{P}}$ and $\mathbf{w}_{\delta\Phi}$ are the misclosure vectors for the pseudoranges and time-differenced carrier phases, respectively; and $\mathbf{C}_{\hat{\mathbf{x}}_{t-1}}$ is the receiver-estimated position and clock covariance matrix based on the last epoch's solution.

4.2 IGS Orbit and Clock Products and Point Positioning Correction Models

The IGS combined orbit and clock products differ by their varying latency and the extent of the tracking network used for their computations [Tétreault et al., 2005]. The IGS Rapid and Final orbit and clock products were used in the research reported in this dissertation and the complete list can be found in the IGS product table [IGS, 2005]. The IGS Final orbit/clock products are usually available on the thirteenth day after the last observation in the GPS week, the IGS Rapid orbit/clock products are available 17 hours after the end of the day of interest. The IGS orbits have a 15-minute sampling interval and IGS clock products have 5-minute sampling interval. 30-second clock products were also used for point positioning tests. IGS orbits and clock are interpolated using recommended Langrangean ninth-order polynomial interpolation. The importance of IGS product sampling interval and IGS product compatibility issues will be discussed in the

data testing summary. IGS atmospheric parameters products will be discussed in section 4.3.2.2.

Point positioning processing modelling considerations include the relativistic GPS satellite clock correction due to the eccentricity of GPS satellite orbits (metre-level); GPS satellite antenna phase centre to centre-of-mass offset (metre-level); GPS satellite phase wind-up due to the relative rotation of the GPS satellite antennas with respect to a receiver antenna (dm-level); sub-diurnal variations in Earth rotation (cm-level); solid Earth tides (dm-level); ocean tide loading (cm-level); and consistency between models used in the generation of GPS orbits and clocks and models used in the point positioning processing (2 ns on user's clock) [Kouba and Héroux, 2001].

The filter's functional model currently includes all point positioning processing modelling considerations except the solid Earth tides and ocean tide loading, satellite phase wind-up and sub-diurnal variations in Earth rotation. The magnitude of the site displacement effects due to the solid Earth tides is on the decimetre-level, and ocean tide loading is on the centimetre-level (Table 2.1) [Tétreault et al., 2005]. The solid Earth tides and ocean tide loading are irrelevant to the spaceborne GPS applications, but they apply to terrestrial applications. Time-differencing of the carrier-phase observation results in the time differenced wind-up effect which is, with the exception of dynamic terrestrial platforms, at the sub-millimetre-level [Bisnath, 2004]. Research on residual error in the ionospheric delay modelling was given priority over the satellite and receiver phase wind-up implementation. Sub-diurnal variations in Earth rotation are relevant to

centimetre-level point positioning which requires dual-frequency, low-multipath observations used available from geodetic-quality GPS receivers and so, again, was ignored. Multipath effects will have an impact on low-cost receivers and potential mutipath mitigation strategy will be discussed in section 4.5.

4.3 Atmospheric Effects

Atmospheric effects should also be considered in order to obtain precise and accurate point positioning results. These effects include the ionospheric delay and the tropospheric delay. Atmospheric delay models have similar structure: they both consist of the zenith delay values and mapping functions, which are used to map the zenith delay value into a satellite-receiver slant path value. The mapping function values for elevation angles down to around 16 degrees are almost identical [Misra and Enge, 2001]. This causes a problem in the least-squares estimation process and it is not possible to estimate both zenith delay parameters (ionosphere and troposphere) at the same time. This is one reason why the residual tropospheric delay estimation is not included in the filter; the other reason is the cm-level magnitude of the residual tropospheric delay versus the dm-level accuracy of the ionospheric delay prediction models (see chapter 4.3.2.2).

4.3.1 Troposphere

The tropospheric delay affects all GPS measurements collected within the Earth's troposphere and stratosphere. The size of the tropospheric delay in distance units is about 2.4 m at sea level under normal atmospheric conditions. The tropospheric mapping function multiplies the zenith delay value by the factor of about ten for the satellite elevation angles of five degrees [Misra and Enge, 2001]. The tropospheric delay could be ignored, estimated as an unknown parameter in the least-squares adjustment (if the observation model supports it) or it could be corrected, to a certain extent, by a tropospheric delay prediction model or a combination of these approaches.

The UNB3 tropospheric delay prediction model, which has been used in the analyses, consists of the Saastamoinen zenith tropospheric delay model, Niell mapping functions, a surface met lookup table and height propagators [Collins, 1999]. It is convenient to express the tropospheric delay in two components, the hydrostatic component and the non-hydrostatic component [Mendes, 1999]. The typical formulation for the tropospheric delay is given as:

$$d_{trop} = d^{z}_{hyd} m_{hyd} + d^{z}_{wet} m_{wet} \qquad (4.3)$$

where the total delay d_{trop} is a function of the hydrostatic zenith delay d^{z}_{hyd} and its mapping function m_{hyd} and the wet (non-hydrostatic) zenith delay d^{z}_{wet} and its mapping function m_{wet}.

The hydrostatic component of the zenith delay can be modelled with millimetre accuracy (if accurate station pressure measurements are available), but the water vapour component of the tropospheric delay provides a limiting factor. The expected residual zenith delay error after applying a model such as UNB3 would be typically at the few-centimeter level [Collins, 1999].

4.3.2 Ionosphere

Ionospheric delay handling is an essential component of the research reported in this dissertation. The following sub-sections describe different techniques and their limitations. The techniques include different types of ionospheric delay modelling and ionospheric delay estimation. The single-frequency GPS user also has a measurement linear combination (GRAPHIC) available to minimize the effect of ionosphere. Results obtained with this linear combination can be found in the literature [e.g., Muellerschoen et al., 2004].

Ionospheric delay on the GPS signal is caused by the electrically charged portion of the atmosphere. The ionization of gases occurring in the Earth's atmosphere at heights from roughly 50 to 1000 km result from their interaction with the Sun's radiation. The speed of propagation of a radio signal in the ionosphere, at any instant, depends on the local electron density. The total number of free electrons (in a cross section of 1 metre squared) along the signal path is defined as the total electron content (TEC). The

refractive index for a radio wave is inversely proportional to the square of the frequency of this radio wave [Misra and Enge, 2001]. A user equipped with a dual-frequency GPS receiver can essentially eliminate the effect of Earth's ionosphere as a source of measurement error outside periods of maximum solar activity.

Ionosphere-free pseudorange measurements can be obtained using the following linear combination:

$$P_{IF} = \frac{f_{L1}^2}{(f_{L1}^2 - f_{L2}^2)} P_{L1} - \frac{f_{L2}^2}{(f_{L1}^2 - f_{L2}^2)} P_{L2} \qquad (4.4)$$
$$P_{IF} = 2.546 P_{L1} - 1.546 P_{L2}$$

where f_{L1} is the frequency of the L1 carrier ($f_{L1} = 1575.42$ MHz), f_{L2} is the frequency of the L2 carrier ($f_{L2} = 1227.60$ MHz), P_{L1} is the L1 pseudorange in metres, P_{L2} is the L2 pseudorange in metres, and P_{IF} is the resulting ionosphere-free pseudorange in metres. Ionosphere-free carrier-phase measurements could be obtained using the same principle. Using the propagation of errors it was found that the resulting noise of the ionosphere-free measurements is almost three times worse that that of single-frequency measurements [Misra and Enge, 2001].

4.3.2.1 Broadcast Model

Single frequency users are provided with an algorithm, which uses 8 coefficients from the broadcast navigation message, to correct for approximately 50% r.m.s. of the ionospheric range error [Klobuchar, 1987; 1996]. This Klobuchar model represents the

zenith delay as a constant value at night-time and a half-cosine function during daytime with a maximum at 2 p.m. local time. Update of the Klobuchar model coefficients occurs when there is a significant change in the 10.7 cm solar flux. Some of the results in the early stage of this research were obtained using the Klobuchar model [e.g. Beran et al., 2003].

Some of the limitations of the Klobuchar model were addressed in a Center for Orbit Determination in Europe (CODE) research project, which computes and validates Klobuchar-style coefficients on a regular basis. The coefficients computation is based on the best-fit Klobuchar model to the CODE's Global Ionosphere Map (section 4.3.2.2). The mean and peak differences expressed between the Klobuchar broadcast model and the Global Ionosphere Map (GIM) values are about 13 and 26 TECU (1 TECU = 16 cm on L1) for the GPS broadcast model and about 14 and 35 TECU for the CODE Klobuchar-style model and the GIM values [CODE, 2006]. Klobuchar-style coefficients are mentioned here to complete the description of the ionospheric products. The point positioning filter is capable of using the Klobuchar model but a preference was given to the Global Ionosphere Maps, which are more accurate.

4.3.2.2 Global Ionosphere Map (Grid Map Model)

In order to minimize the effect of the ionosphere, external corrections from IGS composite ionospheric products (Rapid and Final) could be also applied. The slant

ionospheric delays are computed from a geographic grid of TEC values or the ionosphere maps generated by some IGS processing centres [Schaer, 1998]. IGS composite Rapid and Final ionospheric grid maps were used in most of the tests reported in chapter 5.

Using global IGS station data (geometry-free linear combination which carries ionospheric delay data), IGS processing centre in the Polytechnical University of Catalonia (UPC, Barcelona, Spain) computes global ionosphere maps as composite of ionospheric grid maps from CODE, ESA, JPL and UPC. TEC is developed into a series of spherical harmonics adopting a single-layer model in a Sun-fixed, geomagnetic reference frame. Each day, a set of TEC coefficients, which approximates an average distribution of vertical TEC within a certain time interval on a global grid, is computed. Rapid ionospheric grid maps are available in less than 24 hours (2-9 TECU accuracy [IGS, 2005]), and the final ionospheric grid maps are available in about 11 days (2-8 TECU accuracy [IGS, 2005]).

The Ionosphere Map Exchange Format (IONEX) supports the exchange of 2-dimensional or 3-dimensional TEC maps in a geographic grid [Schaer et al., 1998]. Maps are epoch specific. Procedures to compute the TEC value as a function of geodetic latitude, longitude and universal time are described by Schaer [1997]. The CODE recommended strategy is to interpolate linearly between consecutive rotated TEC maps by $t - T_i$ (where t is the interpolation time and T_i is the map reference epoch time). Geocentric longitude of the interpolation point λ' is computed as:

$$\lambda' = \lambda + (t - Ti) \tag{4.5}$$

which represents a rotation around the Z-axis in order to compensate to a great extent for the strong correlation between the ionosphere and the Sun's position [Schaer et al., 1998]. The IONEX format supports two different mapping functions adopted for the TEC determination: 1/cos(z) and the Q-factor mapping function. Further description and comparison of different ionospheric mapping functions can be found in the literature [e.g. Komjathy, 1999].

4.3.2.3 Global 3D Ionospheric Model (Fusion Numerics)

Even though the IONEX format supports the exchange of 3-dimensional TEC maps in a geographic grid, the IGS composite global ionosphere maps are only 2-dimensional. One of the early providers of a global 3-dimensional TEC model is a private company, Fusion Numerics Inc., from Boulder, Colorado. Their IonoNumerics model is a physics-based dynamic model of the ionosphere. It tracks seven ion species based on the solar index and magnetic pull that causes their motion along with frictional heating and cooling processes and chemical transformations. This model is constrained by GPS observations from a global array of GPS stations [Khattanov et al., 2004].

There are currently two versions of the point positioning software. First version of our point positioning software is capable of obtaining the slant ionospheric delay values from the IonoNumerics model running on a host server and the second version obtains the ionospheric delay values from the 2D global ionospheric maps (GIM's). The client-server

communication in the first version of the software is facilitated via Web services. The expected accuracy of the IonoNumerics model is 2 TECU at the 1σ-level [Khattanov et al., 2004].

4.3.2.4 Ionospheric Delay Estimation or Residual Atmospheric Delay Estimation

One option for handling the ionosphere is to estimate the zenith ionospheric delay as an unknown parameter at every epoch in the least-squares estimation process. The partial derivatives of the GPS observables with respect to the unknown parameter, the zenith ionospheric delay, are the ionospheric delay mapping function values for the specific elevation angles. The Klobuchar model mapping function:

$$F = 1.0 + 16.0 * (0.53 - E)^3 \quad (4.6)$$

where E is the elevation angle in semi-circles, was implemented in the processing software even though a standard geometric mapping function, which computes the secant of the zenith angle of the satellite at the thin shell ionospheric pierce point, may provide better results [Komjathy, 1999].

One of the weaknesses of the zenith ionospheric delay estimation is a loss of a degree of freedom in the least-squares estimation process. In case of terrestrial GPS applications, the zenith "ionospheric" delay parameter absorbs a certain percentage of the tropospheric delay. This is due to the similarity of the mapping function values even for low-elevation

angles. The spaceborne GPS applications will benefit from the zenith ionospheric delay estimation more than the ground-based applications, because the spaceborne measurements are obtained within the ionosphere on a vehicle rapidly moving through the ionosphere and ground-based ionospheric models may not be applicable. The residual ionospheric delay estimation in this case, is actually estimating the effect of the ionosphere between the satellite equipped with a GPS receiver and a GPS satellite transmitting the signal. The above-satellite portion of the ionosphere will vary due to the different height of the GPS-equipped satellite above the Earth's surface (due to the ellipticity of the orbit); due to the position of that satellite in its orbit; and due to the variations in the ionosphere in time.

4.4 Cycle slips

The loss of carrier-phase tracking resulting in an integer number of cycles discontinuity will cause an error in the carrier-phase measurements. The loss may be due to internal receiver tracking problems or an interruption in the ability of the antenna to receive the satellite signals [Seeber, 1993]. The signal tracking interruptions usually occur when a satellite is observed at a low elevation angle. The process of repairing a cycle-slip consists of cycle slip detection; finding out the exact epoch when a cycle-slip occurred, cycle-slip determination; determining the size of the cycle-slip, and cycle-slip correction, correcting the carrier-phase measurements to make them continuous [Teunissen and Kleusberg, 1998].

The majority of the cycle-slip detection algorithms require a smooth (low-noise) quantity derived from the observations, which is tested for discontinuities that may represent a cycle-slip [Bisnath et al., 2001]. The observables available in the case of a low-cost, single-frequency GPS receiver are L1 pseudoranges and L1 carrier-phase observations. Cycle-slip candidates could be detected in the geometry-free pseudorange minus carrier-phase linear combination or in the time-differenced carrier-phase linear combinations. The first is also known as the geometry-free linear combination and the technique will perform the same on static and kinematic data. One potential drawback of the geometry-free linear combination is the pseudorange noise, which will cause the technique to fail to detect cycle-slips of a few cycles. The second technique is more feasible for the pseudorange and time-differenced carrier-phase filter, because the filter requires continuous carrier-phase measurements only between two consecutive epochs.

A cycle slip detection algorithm used in the point positioning filter software, developed for the research reported in this dissertation, creates all possible relative difference in jerks (time-differenced accelerations) between all satellites in view, selects a potential cycle slip candidate and removes it from the solution. This process runs in a loop until all relative differences are below a given threshold or until all satellites are rejected and the filter has to return to a code-only solution.

4.5 Multipath

The typical multipath error in the pseudorange measurement varies from about 1 m to 5 m. Multipath in the pseudorange measurements are usually two orders of magnitude bigger than the multipath errors in the carrier-phase measurements [Misra and Enge, 2001]. Pseudorange multipath errors in terrestrial applications will have an impact mostly on low-elevation angle measurements, so one of the filter software configuration settings is elevation angle cut-off. Pseudorange multipath errors in spaceborne applications is usually minimized by careful GPS antenna location, and/or GPS antenna hardware, on the space vehicle.

One alternative method to reduce the negative impact of multipath errors on single-frequency measurements is to use an elevation angle dependent weighting function, based on the actual amount of multipath in the measurements. This weighting function is typically an exponential function, which has been found to fit the least-squares residuals plotted against the elevation angle [Jin, 1996]. The equation of the weighting function is:

$$y = a_0 + a_1 e^{\left(-\frac{x}{x_0}\right)} \tag{4.7}$$

where y is the r.m.s. error, a_0, a_1 and x_0 are coefficients dependent on the receiver brand and the observation type, and x is the satellite elevation angle in degrees. In order to determine the parameters of this exponential weighting function, the least-squares residuals must be first determined.

The coefficients of the exponential weighting function fitted to the C1 pseudorange residuals from processing of Garmin GPS 35 receiver data collected on September 2nd, 2005 on the roof of Gillin Hall at the University of New Brunswick are a_0 = 0.58, a_1 = 5.27, and x_0 = 19.41. UNB Gillin Hall could be considered a high-multipath site [Boudreau, 1993]. The results provided by Jin, [1996] are a_0 = 0.065, a_1 = 0.5, and x_0 = 15, but the expected amount of multipath is not specified. Orders of magnitude different solutions were computed for datasets from different sites and in many cases a solution was not found.

When the experimental weighing function, with the coefficients computed by the least-squares fit, was used on the Garmin GPS 35 receiver, September 2nd, 2005 dataset, positioning results improved by 5 cm in North and East r.m.s. Height component r.m.s. got worse by the same amount. This is not considered a significant improvement, which would justify further investigation of this weighting function.

There is an option to select the elevation-angle weighting scheme. The options are: uniform weighting scheme; and $1/\cos^2(z)$, where z is the elevation angle of a GPS satellite. Change in the elevation-angle weighting scheme did not result a significant improvement (more than 5 cm-level) of the positioning results.

4.6 Low-Cost Versus Geodetic Quality GPS Receivers

The essential components of any GPS receiver are: an antenna with optional preamplifier, a radio-frequency and intermediate-frequency (RF/IF) "front end" section, a signal tracker/correlator section, a microprocessor that controls the receiver processing of the signal and computes the coordinates, a power supply and memory devices for storing instructions and data [Langley, 2000]. The ranging precision depends on the slope of the correlation function, which depends on the bandwidth of the signal. The ranging performance also depends on the signal-to-noise ratio (or the carrier-to-noise density ratio) and the averaging time used by the receiver bandwidth of code and carrier tracking loops [Misra and Enge, 2001]. Typical bandwidth values for a code-tracking loop for modern GPS receivers range from less than 1 Hz to several Hz [Langley, 1997].

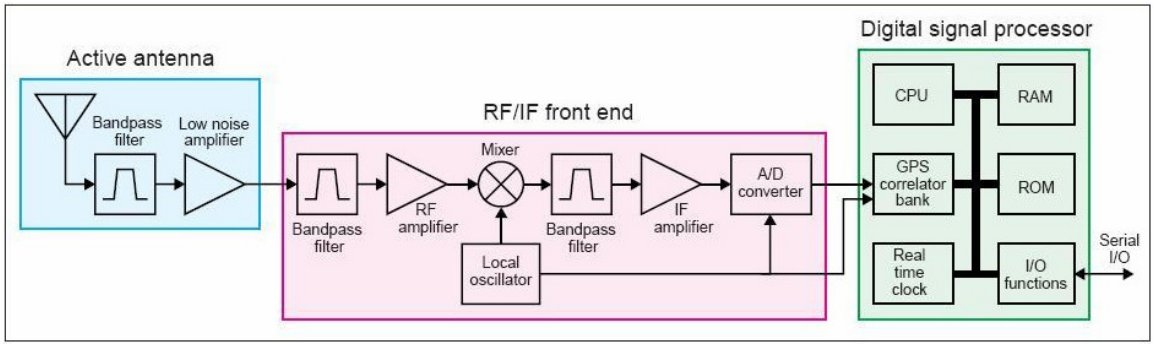

Figure 4.2: GPS receiver components [Langley, 2000].

A concise overview of causes and sources of (thermal) noise contaminating the GPS range observations has been given by Langley [1997]. A key parameter in the precision

of the pseudorange and carrier-phase observations made by the GPS receiver is the carrier-to-noise density ratio. The c/n_0 , expressed in Hz, is the ratio of the power level in the signal carrier to the noise power in (or normalized to) 1 Hz bandwidth. It is usually expressed in dB-Hz by taking the logarithm:

$$C / N_0 = 10 \cdot \log_{10} c / n_0 \tag{4.8}$$

The signal power (with respect to the noise) received at the antenna depends on the signal power transmitted by the satellite and on the loss during the signal propagation. Typical C / N_0 values at present for GPS signals received on the Earth range from 35 to 55 dB-Hz. The code tracking loop, or the delay lock loop (DLL) provides the pseudorange observation and the carrier tracking loop, usually a Costas type phase lock loop (PLL), provides the carrier-phase observation [Langley, 1997].

In order to assess the internal noise of a GPS receiver a zero-baseline test could be performed. The advantage of this test is that the baseline coordinate differences are precisely known and the ambient environmental effects, such as atmospheric delays and multipath, will cancel out when the GPS observations are differenced between the two receivers. Standard deviations in the C/A-code on L1 measurements for geodetic-quality GPS receivers range from 0.04 to 0.26 m for the zero-baseline test of geodetic-quality GPS receivers [Bona and Tiberius, 2001]. A zero-baseline test with two low-cost GPS receivers (Garmin 25 LP) show average C/A-code noise values of 2.3 m using a low-cost antenna and 0.8 m for a geodetic-quality antenna [van Leeuven, 1998].

The clocks in most GPS receivers are of an inexpensive kind for practical reasons. The

requirement for the clock to maintain a satellite signal in track could be generally met with a temperature-compensated crystal oscillator (TCXO). The offset between the receiver clock and the GPS system clock ensemble is allowed to change in time without any significant constraints [Misra, 1996]. This would be the case for the majority of low-cost GPS receivers. Geodetic-quality GPS receivers use a receiver clock-steering technique to maintain the offset with respect to the GPS system clock to within 1 millisecond. This is usually accomplished by adding or subtracting 1 millisecond to the receiver clock whenever the receiver clock offset with respect to GPS time reaches a certain threshold. Some of the results presented in this dissertation show about 47 millisecond-per-hour-drift for a low-cost GPS receiver and 0.5 millisecond-per-hour-drift for geodetic-quality GPS receivers.

The general purpose of a GPS antenna is to convert the energy in the electromagnetic waves arriving from satellites into an electric current that can be processed by the electronics in the receiver [Langley, 1998]. The antenna may be required to operate just at the L1 frequency, in case of low-cost, single-frequency GPS receivers, or at both L1 and L2 frequencies, in case of geodetic-quality GPS receivers. Perhaps the most common antenna type is the microstrip patch antenna [Langley, 1998]. Several parameters describe the performance of antennas. Antenna bandwidth is the frequency band over which the antenna's performance is acceptably good. A microstrip patch antenna designed for use with a standard C/A-code receiver will have a narrower bandwidth compare to P(Y)-code or codeless or semi-codeless tracking. Dual frequency antennas typically have two patches, one for each frequency, each one of which has a bandwidth of

about ±10 MHz, which is a similar bandwidth to the one required for P(Y)-code tracking [Langley, 1998]. Different-quality antennas play a role in the tests presented in chapter 5.

A GPS antenna is usually combined with a low-noise preamplifier that boosts the signal's level before feeding it to the GPS receiver [Langley, 1998]. Geodetic-quality GPS receivers usually use active antennas which receive the power for the antenna preamplifier through the same coaxial cable along which the signal travels to the receiver [Langley, 1998]. Preamplifier characteristics (low-noise, high-gain) for the geodetic-quality GPS antennas will be better than those of low-cost GPS antennas. Last but not least, the geodetic-quality GPS antennas could have a special design, which reduces the response to reflected signals to the minimum. This is usually achieved by extending the antenna's ground plane, a piece of metal that the microstrip patch antenna sits on. One form of ground plane is the choke-ring. Choke-ring antennas are effective in reducing the effects of ground-bounce multipath [Langley, 1998].

4.7 Residual Outlier Detection for Low-Cost GPS Receivers

Empirical data collected by a GPS receiver, or any scientific instrument, reflects physical reality. Scientists try to capture this reality by a means of a mathematical model. This model has two components: the functional model which describes the relationship between the observables and the unknown parameters of the model; and the stochastic model which reflects the variability in the measurement data due to noise and other non-

systematic effects [Teunissen and Kleusberg, 1998].

The need for an adjustment of observations arises when one has to solve a redundant system of observation equations. The redundancy in terms of degrees of freedom is defined as the difference between the number of observations and the number of unknown parameters. Least-squares estimation is the best linear unbiased estimation [Wells and Krakiwsky, 1971]. The least-squares quality testing is based on the two following premises: (1) the unbiasedness, which means that if an adjustment was repeated the different outcomes of the adjustment would on the average coincide with the "true" values in the vector of unknown parameters (the parameters of the mathematical model); (2) the dispersion in this vector describes the precision of the least-squares estimator [Teunissen and Kleusberg, 1998].

The result of an adjustment and its quality relies on the validity of the functional and stochastic model. Prior to the model validation, a null hypothesis (H_0) and an alternative hypothesis (H_a) should be stated. The null hypothesis consists of the model that one believes to be valid, and an alternative hypothesis consists of all misspecifications one can expect in the null hypothesis [Teunissen and Kleusberg, 1998]. The statistical testing presented here will be restricted to the misspecifications in the mean, premise number 1 in least-squares quality testing.

The null hypothesis (H_0) is:

$$\mathrm{E}\{\mathbf{l}\} = \mathbf{A}\mathbf{x},\ \mathrm{D}\{\mathbf{l}\} = \mathbf{C}_\mathbf{l} \tag{4.9}$$

where $E\{\mathbf{l}\}$ is the expectation function of the measurements, **A** is the design matrix, **x** is the vector of unknowns, $D\{\mathbf{l}\}$ is the distribution function, and $\mathbf{C_l}$ is the variance-covariance matrix of the measurements.

The alternative hypothesis (H_a) is:

$$E\{\mathbf{l}\} = \mathbf{Ax} + \mathbf{C}\Delta,\ D\{\mathbf{l}\} = \mathbf{C_l} \tag{4.10}$$

where **C** is an unknown matrix which in one dimensional cases reduces to vector **c**, and Δ is a unknown vector which in one dimensional cases reduces to a scalar.

The testing procedure consists of the three following steps: (1) Detection step, to check the overall validity of the null hypothesis (quadratic form of the residuals is tested); (2) Identification step, to identify the potential source of error in the model (this procedure usually involves screening each individual observation for the presence of an outlier); (3) Adaptation step, which consists of a corrective action, that needs to be taken to get the null hypothesis accepted [Teunissen and Kleusberg, 1998].

In the pseudorange and time-differenced carrier-phase model described in this chapter, a residual outlier detection algorithm runs separately on both pseudorange and delta carrier-phase observations. The level of significance for the null hypothesis testing is 5%, which means that there is 95% statistical significance of the tests. There are no constant threshold values used in these tests, the values in the statistical tests are derived from the a-priori pseudorange and carrier-phase measurement noise information. If an outlier is detected, the corresponding satellite is removed and a new solution is generated and

tested. If all redundant (redundancy is defined as the number of satellites minus number of unknowns) delta carrier-phase measurements are rejected, the filter generates a code-only solution and its variance covariance matrix. The solution and the variance covariance matrix of the estimated parameters are used as a new initial solution (the filter will reset).

4.8 Realisation of Single-Frequency Point-Positioning Algorithm in Processing Software

The single-frequency point-positioning algorithm has been implemented with the C++ programming language in the Microsoft Visual Studio C++ integrated development environment. The point-positioning filter software is designed to process all observed data, and auxiliary data from external sources, in a single run. The software design principles are consistent with object-oriented programming philosophy: the related data objects and functions performed on them are encapsulated in classes and the complexity of these functions is hidden from the user of this software.

Figure 4.3 shows the flowchart of the main function of the point positioning filter software. The software opens the observation file in RINEX format [Gurtner, 2002] and looks for a valid epoch of data. If the data is found, it is stored in the current epoch object. If not, the software stops. In the next step the software looks for the data stored in the previous epoch object. If the data is available, the software calls the code and delta-phase solution function, and if not the software calls the code-only solution function. If a

solution is produced, results are stored in output files. After that, the current epoch data object is copied to the previous epoch data object and the software returns to the observation file and the processing continues. Function call graph for the main function is shown in Appendix I and function call graph for the calcCodePhaseSolution function is shown in Appendix II.

The input files are defined in the command line, which calls the compiled executable version of the software. The input files are the RINEX observation file, precise ephemeredes in the SP3 format, ionospheric grid map in the IONEX format, and the high-rate clock file in the CLK format. The output files for each epoch include the computed coordinates, receiver clock errors and their uncertainties, number of satellites used in the solution and the geometrical dilution of precision (GDOP), least squares residuals for the pseudorange observations, and time-differenced carrier-phase observations, input file names, time of processing and the software settings.

The software settings include Boolean flags for use of ionosphere-free linear combination (if the dual-frequency data is available), a flag for use of P1 pseudorange (if it is available), a flag for zenith delay estimation, flags for code and delta-phase residual outlier detection usage, elevation cut-off angle value and values for measurement standard deviations for pseudorange measurements and for the carrier-phase measurements. Appendix III shows an example of the configuration file. In the current version of the software the processing parameters are included in a configuration file and a new executable has to be generated every time the settings are changed. In the next

version of the processing software, the configuration file will be added to the list of input files in the command line.

The pseudorange and time-differenced carrier-phase model, implemented in the software, utilizes pseudorange and carrier-phase measurements. The software uses IGS orbit and clock products of the highest quality available at the time of processing. Atmospheric effects are compensated to a large extent by the tropospheric delay prediction model and by the ionospheric grid map model. Cycle slips in the carrier-phase observations are detected and the contaminated observations are rejected from the processing. In the next chapter, the developed software will be tested. The objective is to determine the correctness of different components of the mathematical model as well as its performance and ability to process different data types under different conditions.

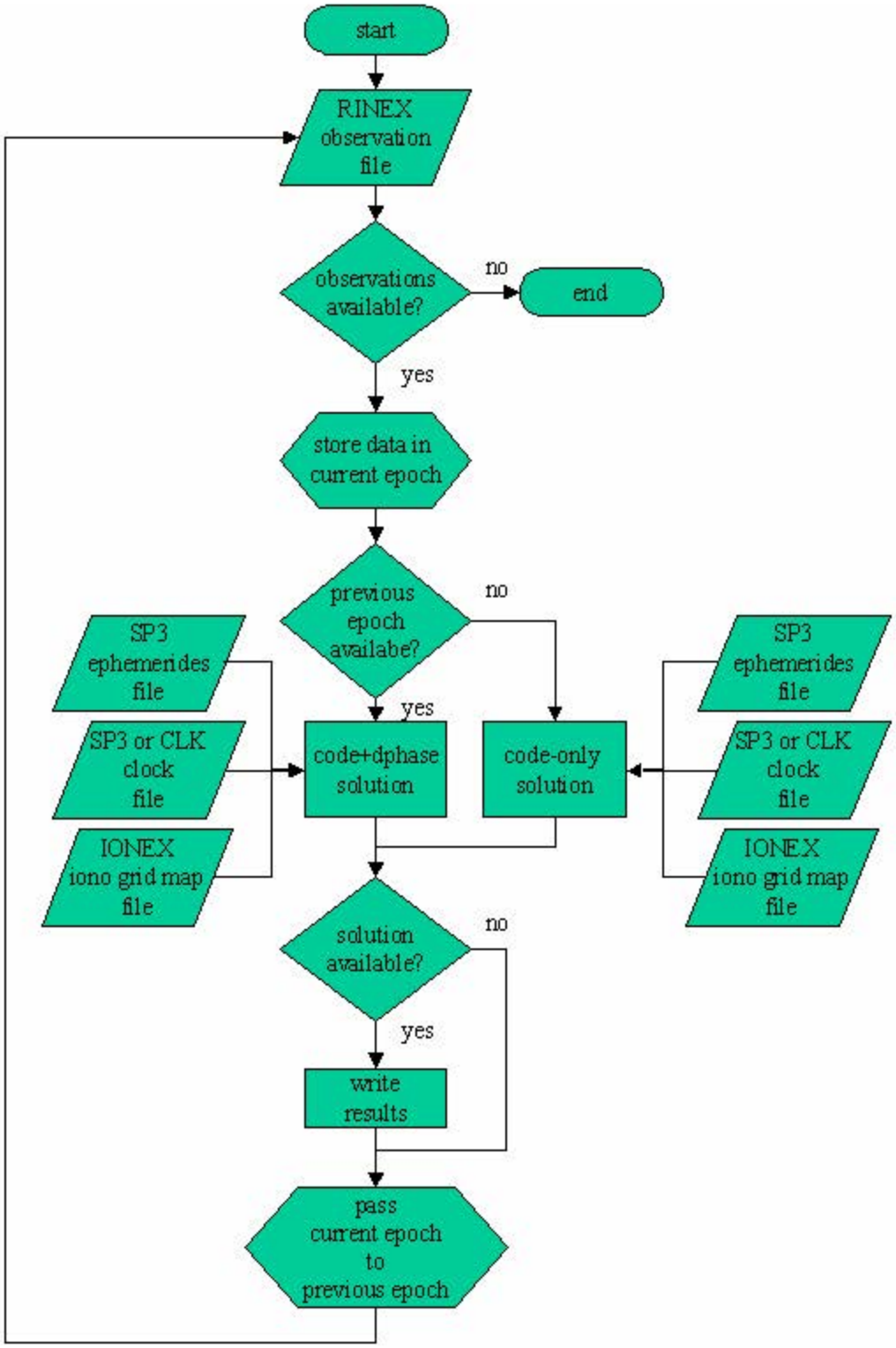

Figure 4.3: Flowchart of the main function of the point positioning software.

5 Data Testing and Analysis

Static and kinematic tests were performed to demonstrate the capabilities of the single-frequency point-positioning technique. The first few sections of this chapter focus on the filter's ability to handle the ionospheric delay; the impact of the data sampling rate on the quality of the results; and the convergence interval testing. The rest of this chapter describes the ground-based static, ground-based kinematic, and spaceborne kinematic tests in this order. The tests were performed on different days with different GPS equipment, but in all cases the IGS final ephemerides and GPS satellite high-rate clock information were used.

The fact that the tests were performed on different days with different GPS equipment will make the tests incoherent and difficult to compare. In order to keep the test results consistent between dates and sites an overlapping tests were generated. Table 5.1 shows the summary of overlapping tests performed on the same dates, at the same sites, and with the same equipment.

Test	Date	Station/ Platform	Receiver
Ionospheric Delay	26 September, 2004 2 September, 2005	CAGS ALGO	Ashtech Z-XII3 AOA Benchmark
Terrestrial Static	11 December, 2005 2 September, 2005	ALGO Lincoln Heights	AOA Benchmark Garmin GPS 35
Terrestrial Kinematic	11 December, 2005	car	Garmin GPS 35

Table 5.1: Summary of overlapping tests.

5.1 Ionospheric Delay Modelling and Estimation

There are three ways to handle an unknown parameter in the estimation process. It could be ignored; it could be modeled with an external model; it could be estimated as an additional unknown parameter in the least-squares estimation process; or it could be eliminated by a linear combination of observations. Ignoring the ionospheric delay results in metre-level or larger position variations in all position components, but the most significant effect is found in the up-component estimate. Measurements on both L1 and L2 frequencies have to be available in order to create linear combinations, which eliminate the bulk of the ionospheric delay.

In the following subsections two external ionospheric models were tested: a 2D global ionospheric grid model, and a 3D global ionospheric model.

5.1.1 Comparison of Single-Frequency Corrected by Using Global Ionosphere Maps and Ionosphere-Free Results with Geodetic-Quality GPS Receivers

As indicated in section 4.3.2, there are different models and techniques available to handle the ionospheric delay. A geodetic-quality GPS receiver was used to provide the test data in this section, because low-cost receivers, in general, are not capable of tracking the GPS signal on the second frequency. A comparison of single-frequency corrected by using the IGS's composite global ionosphere map, and ionosphere-free results from the Algonquin Park station from a 24-hour dataset on 26 September 2004 was performed to confirm the accuracy of the final ionospheric maps from the IGS products table [IGS, 2005]. Ionospheric-model-corrected single-frequency pseudorange (C1) and time-differenced carrier-phase positioning results and ionosphere-free pseudorange and ionosphere-free time-differenced carrier-phase positioning results were obtained using the point positioning filter described in chapter 4. IGS precise ephemerides and clock and a 15-degree elevation cut-off angle were used in both cases. A-priori pseudorange noise value of 1.0 m and a-priori carrier-phase noise value of 5 cm were used. ALGO IGS station coordinates at the epoch of measurement were used as reference. The initial 20 epoch solution is considered to be the filter convergence interval and these epochs are excluded from the solution statistics. Detailed analysis of the filter convergence interval can be found in section 5.2.2. The two positioning solutions are plotted in Figure 5.1 for comparison.

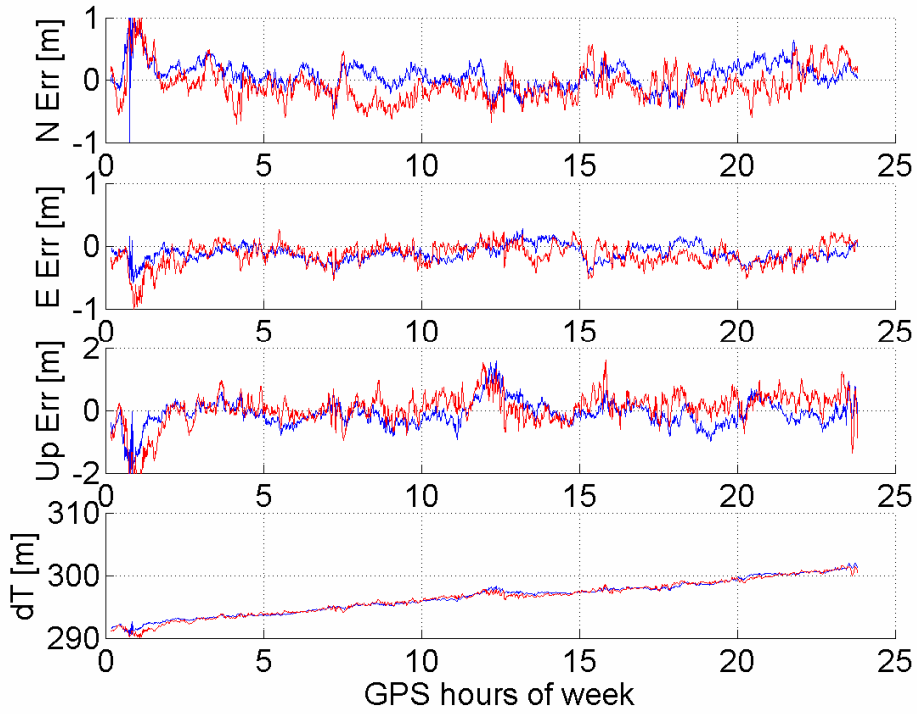

Figure 5.1: Single-frequency pseudorange (C1) and time-differenced carrier-phase positioning results corrected by using the global ionosphere map (blue) and ionosphere-free pseudorange and ionosphere-free time-differenced carrier-phase positioning results (red) for a 24-hour Algonquin Park dataset.

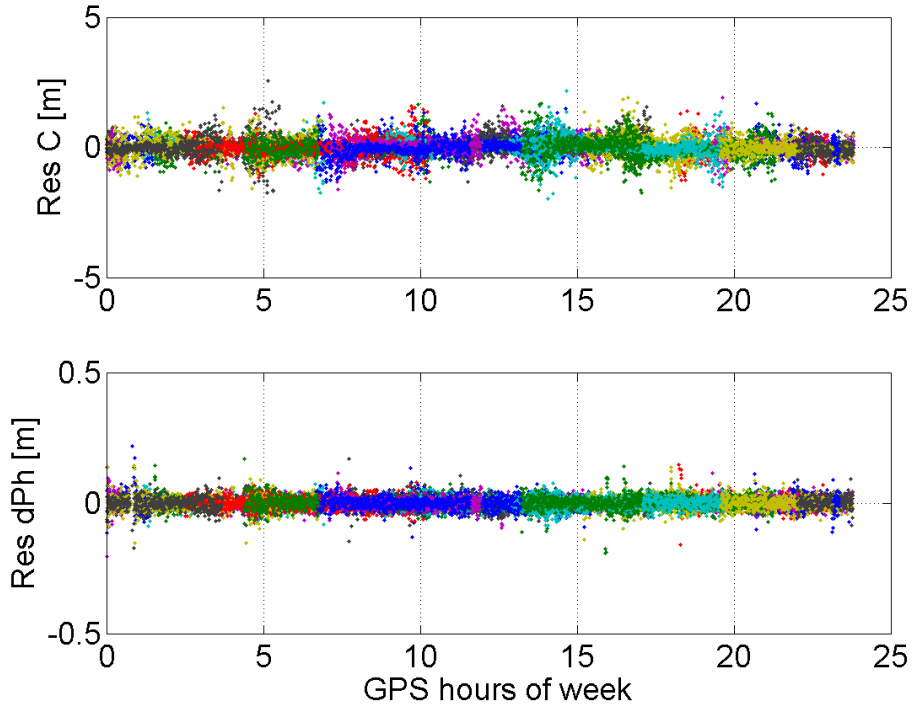

Figure 5.2: Filter residuals from the single-frequency Algonquin Park data processing.

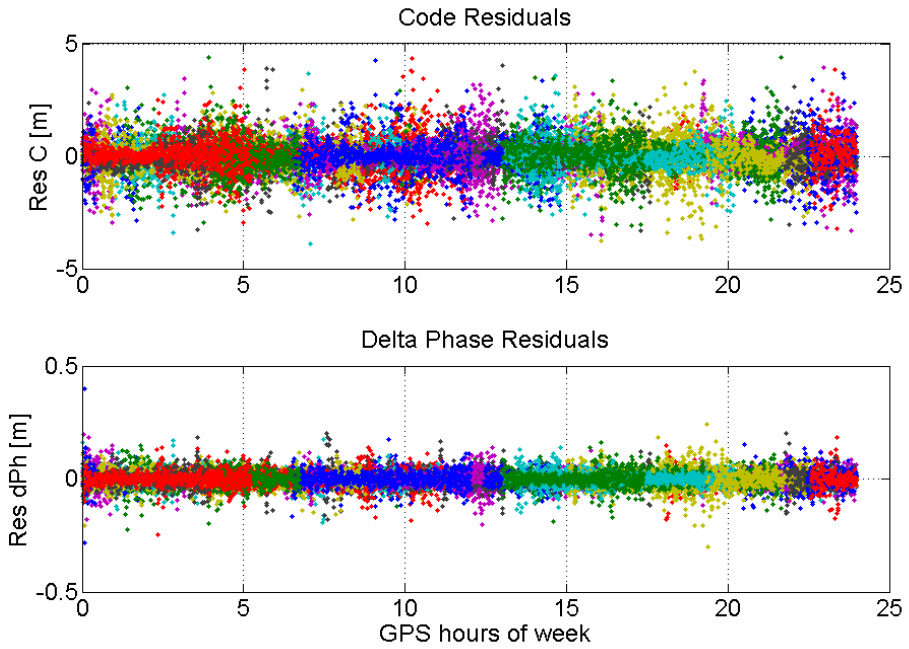

Figure 5.3: Filter residuals from the ionosphere-free Algonquin Park data processing.

Ionospheric-model-corrected single-frequency and ionosphere-free data processing statistics for the 24-hour Algonquin Park dataset in Table 5.2 show that there is no significant bias in the up component if the model-corrected measurements are used. Height-component standard deviation is bigger than the horizontal component standard deviations for both sets of results because of the absence of point positioning specific correction models listed above, and due to satellite geometry limitations. Overall the position components standard deviations and the measurement residual r.m.s. of the ionosphere-free solutions are bigger than those of the single-frequency solution because of the factor-three higher noise in the ionosphere-free measurement linear combinations.

Position Error Components [cm]			
	North	**East**	**Height**
Mean	6.8	1.5	-13.0
	-7.7	*-1.0*	*3.7*
Std.	21.8	12.5	41.8
Dev.	*26.9*	*17.3*	*52.7*
r.m.s.	22.8	12.6	43.7
	28.0	*17.3*	*52.8*
Measurement Residual r.m.s. [cm]			
Code	32.1	dPhase	2.3
	54.0		*3.4*

Table 5.2: Ionospheric model corrected single-frequency and ionosphere-free (italics) data processing statistics for a 24-hour Algonquin Park dataset ignoring the initial 20 epochs of data.

In order to validate the results Canadian Spatial Reference System Precise Point Positioning (CSRS-PPP) on-line processing engine was used [Tétreault et al., 2005]. The processing engine used static user dynamics option, ionosphere-free pseudorange and carrier-phase observations, 10 degrees elevation angle cut-off, and precise orbits and clocks. A-priori pseudorange noise value of 2.0 m and a-priori carrier-phase noise value of 1.5 cm were used. Zenith tropospheric delay parameter was estimated using 5 mm/hour random walk value.

The dual-frequency ALGO data were also processed with the CSRS-PPP engine, mean differences between the IGS reference coordinates and CSRS-PPP are 0.1 cm, 0.8 cm, and 2.7 cm in north, east, and height components, respectively. The standard deviations for the CSRS-PPP are 0.3 cm, 0.8 cm, and 1.3 cm in north, east, and height components, respectively. The more than an order of magnitude difference in the standard deviations between the CSRS-PPP and code and delta-phase filter is caused by: (1) the terms that are not included in the functional model in the code and delta-phase filter. These errors include: solid Earth tides and ocean tide loading, satellite phase wind-up and sub-diurnal variations in Earth rotation. The solid Earth tidal correction can reach up to 30 cm in radial and 5 cm in horizontal direction [Kouba and Héroux, 2001]. It consists of latitude-dependent permanent displacement and periodic part with predominantly semidiurnal and diurnal periods and changing amplitudes. The periodic part is largely averaged out over 24-hour period, however the permanent part, which can reach up to 12 cm in radial direction in mid-latitudes, still remains. (2) Different types of functional models. CSRS-PPP is a static filter estimating the tropospheric delay, while

code and delta-phase filter is a kinematic filter using tropospheric delay model. (3) Different software settings such elevation angle cut-off, and a-priori pseudorange noise value a-priori carrier-phase noise value.

5.1.2 Comparison of Single-Frequency Positioning Corrected by Using Global Ionosphere Maps and Single-Frequency Positioning Corrected by Using a Global 3D Ionospheric Model

There are different types of ionospheric models available to single-frequency GPS users. A comparison of positioning results obtained with a IGS composite global ionospheric grid map model (2D model) and a global ionospheric 3D model from Fusion Numerics Company in Boulder, Colorado, U.S.A. [Khattanov et al., 2004] is presented in this section.

The Fusion Numerics ionospheric forecasting system consists of two parts: a first principles numerical model of the ionosphere and a data assimilation component. The ionospheric model solves plasma dynamics and composition equations governing evolution of density, velocity and temperature for 7 ion species on a fixed global 3D grid in geomagnetic coordinates. The accuracy of the ionospheric model is improved by employing numerical weather forecasting techniques known as data assimilation. The core model is continuously fed data from a network of reference GPS ground stations [Khattanov et al., 2004].

One version of the point positioning software used the slant delays computed from the global 3D model. The pseudorange-only solution generates approximate receiver positions at each epoch. Computed positions are submitted to the Fusion Numerics server which computes the 3D global ionospheric model. The server returns slant ionospheric delays for each satellite in view and the delays are used in the final pseudorange and time-differenced carrier-phase filter. The Fusion Numerics 3D model is generated continuously and the data from the past two days is always available. For this test the ionospheric model data from 26 September 2004 was kept on the server.

The 2D and 3D model comparison was performed using GPS data from the Canadian absolute gravity station (CAGS) in Gatineau, Quebec, Canada. The CAGS station is equipped with an Ashtech Z-XII3 receiver and Ashtech ASH700936C_M choke ring antenna. The GPS receiver internal frequency standard was used. A 2-hour dataset from 26 September 2004, IGS precise ephemeris and clock and 15 degrees elevation cut-off angle were used in both cases. This test was performed, in part, to confirm the accuracy of the 3D global ionospheric model.

The two positioning solutions are plotted in Figure 5.4 for comparison. CAGS was selected because its data are not used to generate either of the two models compared in this experiment. A relatively short, 2-hour dataset was chosen, due to the limits of the client-server communication with the 3D ionospheric model data. The local time for the

observation was from 9 pm till 11 pm. The absence of solid Earth tide model should have maximum effect on the vertical component, because the full moon event occurred on September 28, 2004, at 13 hours UT. Given the fact that the solid Earth tide period is about 12 hours, and the fact the observation was to days and almost 12 hours before this event, it should be expected that at the time of observation the Earth tide is close to its maximum amplitude. Both positioning solutions are equally affected by the absence of the solid Earth tide effect in the functional model.

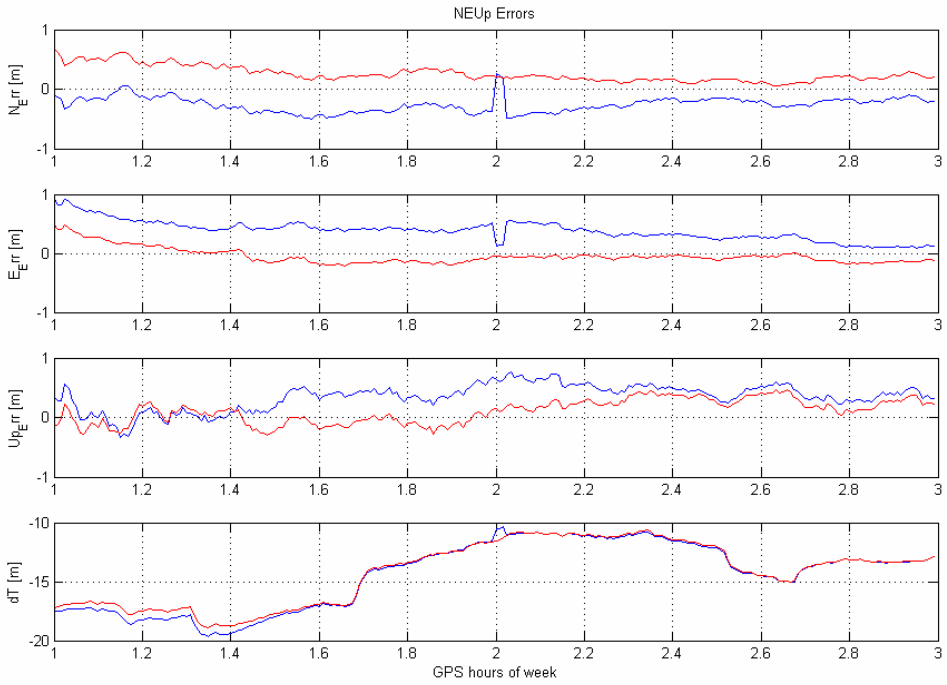

Figure 5.4: Single-frequency positioning results obtained with a global ionospheric grid map model (red) and single-frequency positioning results obtained with the global ionospheric 3D model (blue) from a 2-hour CAGS dataset.

The global ionospheric grid map and global ionospheric 3D processing statistics for the 2-hour CAGS dataset in Table 5.3 show that the ionospheric grid map model results are closer to the benchmark coordinates from the IGS network adjustment at the time of measurement. From Figure 5.4 it can be seen that the differences in r.m.s. values come from the differences in the means. It is possible that for a short-period of time at mid-latitudes, the single-frequency positioning results obtained with the global ionospheric grid map model are better than the single-frequency positioning results obtained with a global ionospheric 3D model. The 3D global ionospheric model is expected to generate better results under disturbed ionospheric conditions in low-latitude regions [Khattanov et al., 2004]. The decimetre-level jump around hour two, on the 3D north, east and receiver clock error timelines is caused by the residual outlier detection algorithm, rejecting a satellite from a solution due to missing information in the 3D ionospheric model (Figure 5.4 blue timeline). For unknown reasons, a few missing epochs were found in the 3D model output. The Earth's ionosphere was considered quiet on 26 September 2004 [NOAA Space Environment Center, 2006].

Position Error Components [cm]			
	North	**East**	**Height**
r.m.s.	17.0	9.0	28.0
	26.0	*31.0*	*48.0*
Measurement Residual r.m.s. [cm]			
Code	29.0	dPhase	1.2
	32.0		*1.3*

Table 5.3: Single-frequency positioning results obtained with a global ionospheric grid map model and single-frequency positioning results obtained with a global ionospheric 3D model (italics) from a 2-hour CAGS dataset ignoring the initial 20 epochs of data.

Four-hour period of the same dataset that was used in section 5.1.1 was also used for the 3D ionospheric model testing. Algonquin Park station from 1 am to 5 am (9 pm to 1 am local time) dataset on 26 September 2004 was processed with the same pseudorange and time-differenced carrier-phase filter settings as the CAGS station dataset. In the first case the single-frequency positioning results were obtained with a global ionospheric grid map model (Figure 5.5), and in the second case the single-frequency positioning results obtained with the global ionospheric 3D model (Figure 5.6).

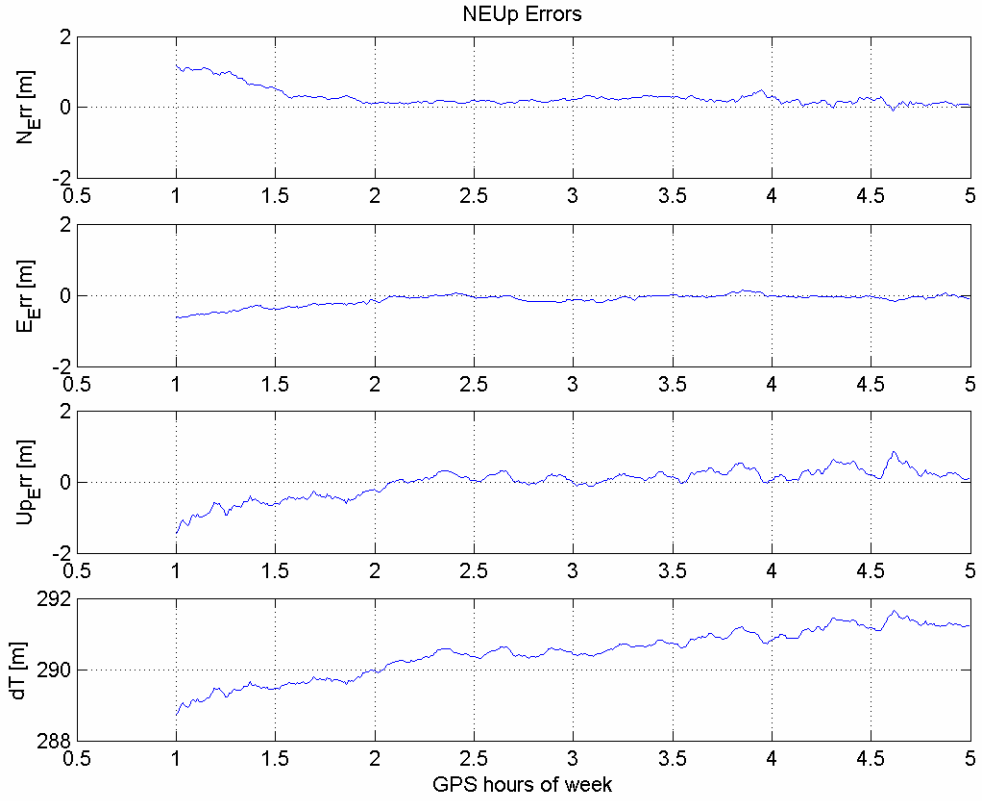

Figure 5.5: Single-frequency positioning results from 4-hour ALGO dataset obtained with a global ionospheric grid map model.

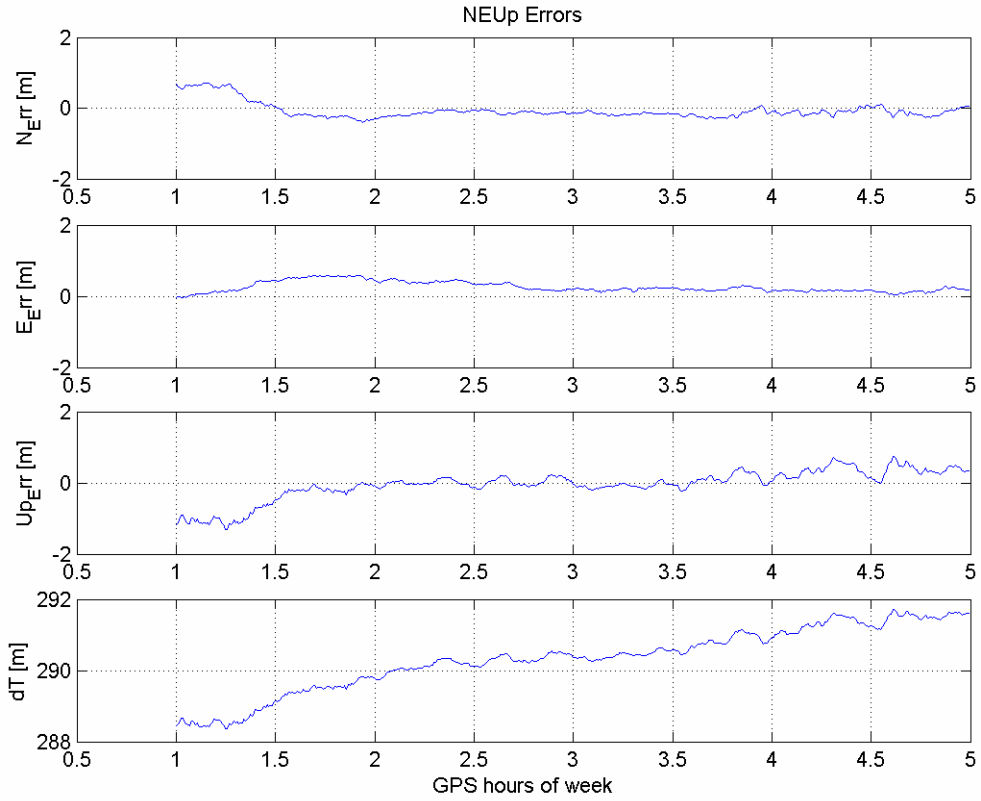

Figure 5.6: Single-frequency positioning results from 4-hour ALGO dataset obtained with a global ionospheric 3D model.

The r.m.s. of differences of the estimated positions with respect to the known coordinates for ALGO station presented Table 5.4 in horizontal components are similar to these for CAGS station presented in Table 5.3. The vertical component differences of the estimated positions using the global ionospheric grid map model for the ALGO station are also only a few centimetres different than those of the CAGS station. However, this is not the case when global ionospheric 3D model was used. The difference in the vertical component r.m.s. for the ALGO station is about 23 cm different than the one for the CAGS station. This is caused by the fact that the ALGO station does not provide grounds for independent comparison, because the ALGO station data is used

to generate the global ionospheric grid map model. The absence of solid Earth tide model will have a similar negative impact on the ALGO station data processing as on the CAGS station data processing.

Position Error Components [cm]			
	North	**East**	**Height**
r.m.s.	19.8	9.0	26.2
	16.1	*25.2*	*25.3*
Measurement Residual r.m.s. [cm]			
Code	29.4	dPhase	1.2
	32.6		*1.3*

Table 5.4: Single-frequency positioning results obtained with a global ionospheric grid map model and single-frequency positioning results obtained with a global ionospheric 3D model (italics) from a 4-hour ALGO dataset ignoring the initial 20 epochs of data.

It is recommended that more complete testing of the Fusion Numerics 3D global ionospheric model [Fusion Numerics Inc, 2005] is necessary to validate its accuracy. A full performance assessment of the 3D ionospheric model would involve tests on multiple datasets from different geographical locations, with varying latitude. Different datasets collected under different ionospheric conditions would have to be tested.

5.1.3 Ionospheric Delay Estimation

In theory, the ionospheric delay could be estimated as an additional unknown parameter in the least-squares estimation process. The mathematical model should be similar to the residual tropospheric delay estimation model [van der Wal, 1995] albeit with a different mapping function. An optional estimation of the zenith ionospheric delay was implemented in the pseudorange and time-differenced carrier-phase filter. Use of the ionospheric delay model global ionospheric grid map model is also optional, so the filter can estimate the total or the residual zenith ionospheric delay. Please note that the ionospheric delay mapping function and the tropospheric delay mapping function are similar at high elevation angles [Misra and Enge, 2001]. The residual tropospheric delay is still present in the observations and to a certain degree it will be absorbed by the zenith "ionospheric delay" estimate.

A zenith ionospheric delay estimation experiment was performed on low-cost receiver data from 26 September 2004 from ALGO station. The coordinate differences with respect to the point position solution in terms of northing, easting, and height error r.m.s. are 3.8, 2.6 and 7.2 m, respectively with no zenith ionospheric delay estimation. The coordinate differences with respect to the same position in terms of northing, easting, and height error r.m.s. are 5.8, 4.2 and 113.6 m, respectively with the zenith ionospheric delay estimation. The zenith delay estimates look like a metre-level random noise with zero mean. Positive and negative(!) hundred-metre-level spikes are also present. In general the negative zenith ionospheric delay values do not make sense, but from the residual

analysis and the statistics it can be concluded that the zenith ionospheric delay estimation weakens mainly the up-component estimation by a factor of ten. Zenith ionospheric delays from the Wide Area Augmentation System (WAAS) [UNB WAAS monitoring station, 2004] at the nearest grid point were considered as metre-level approximate values. These values provide additional proof that the zenith ionospheric delay estimates are not correct.

There is no evidence that anybody has successfully implemented the zenith ionospheric delay estimation as an additional unknown parameter in a conventional weighted least squares technique. Besides the possibility of a software implementation error, a possible reason for the failure of the zenith ionospheric delay estimation is the mathematical correlation between the up component estimates, receiver clock error estimates and the zenith ionospheric delay estimates. Further analysis is required to determine if the zenith ionospheric delay could be estimated as an additional unknown parameter in the least-squares estimation process.

The focus of section 5.1 was to assess the filter's ability to handle the ionospheric delay. The 2D global ionospheric grid model, and a 3D global ionospheric model were tested against the ionosphere-free results obtained from dual-frequency data. The results show that the filter can correct single-frequency data with a 2D or 3D model without a significant loss in accuracy in vertical coordinate component (height component r.m.s.) which leads to a conclusion that the filter is able to correct single-frequency data with either model.

5.2 Filter Performance Evaluation

Different filter performance is observed with different observations and different filter settings. Two filter performance parameters were selected for further investigation: the sampling interval and the convergence interval. During the filter development stage it was found that the data-sampling rate has a direct impact on the precision of the results, so the sub-section 5.2.1 examines this relationship.

There are different definitions of filter convergence time. In the Kalman filter problem, which is a generalisation of a least-squares problem, the filter convergence time is defined as the time interval from the start of the filter to the time when the past-estimates and the new measurements are weighted equally in the filter [Gelb, 1974]. An alternative definition for the sequential least-squares estimation and the convergence interval testing is summarized in sub-section 5.2.2.

5.2.1 Sampling Interval Testing

The relationship between the sampling rate and quality of the positioning results was

studied as a part of the point positioning filter development. One-second data from Algonquin Park station from September 2, 2005 were down sampled to 5 s, 10 s, 30 s, 1 min, 2 min, and 4 min sampling intervals and processed with the single-frequency code and time-differenced phase point positioning filter. Figure 5.7 and Figure 5.8 show position errors with respect to the known IGS position for the Algonquin Park station on different datasets with different sampling rates and code and delta-phase residuals. Table 5.5 summarizes the r.m.s. of the position component errors and the r.m.s. of the residuals.

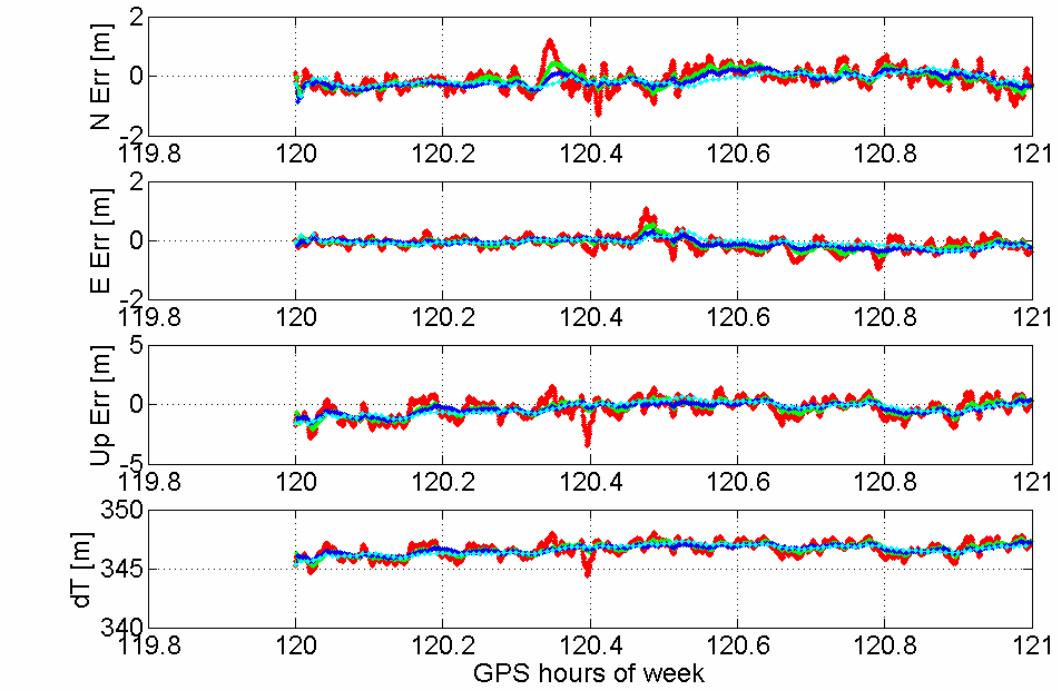

Figure 5.7: Position errors with respect to the known IGS position for the Algonquin Park station on different datasets with different sampling intervals: (red) 1 second, (green) 5 second, (blue) 10 second, and (cyan) 30 second sampling intervals respectively.

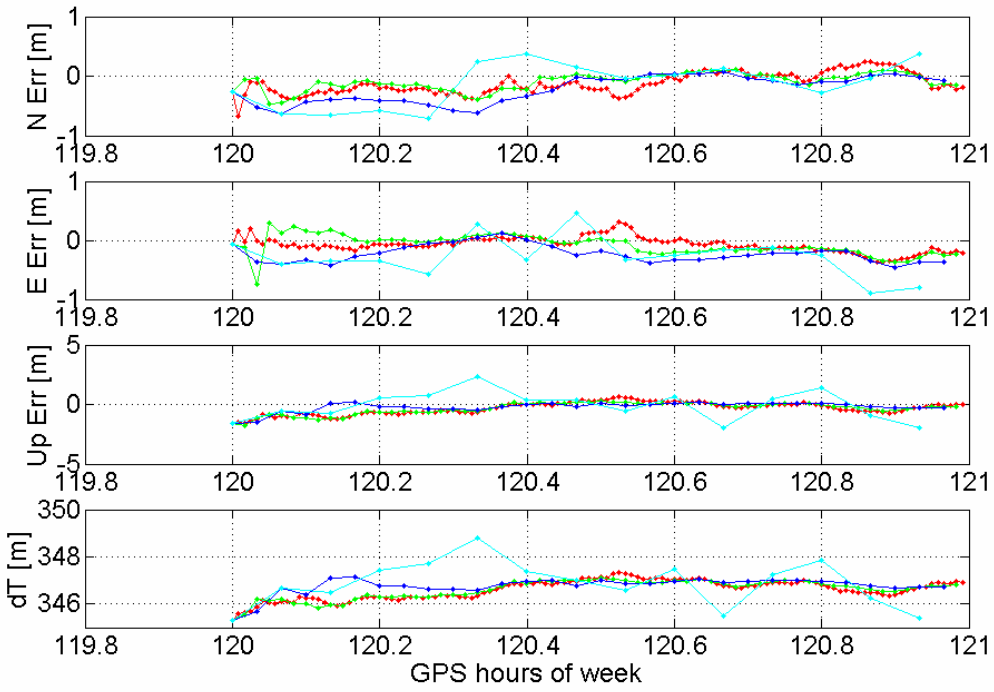

Figure 5.8: Position errors with respect to the known IGS position for the Algonquin Park station on different datasets with different sampling intervals: (red) 30 second, (green) 1 minute, (blue) 2 minute, and (cyan) 4 minute sampling intervals respectively.

The results in Table 5.5 present r.m.s. values, similar to the values in Beran et al. [2005],. Both sets of results indicate that with longer sampling intervals, there is an increase in r.m.s. of delta-phase residuals. This phenomenon is most likely caused by the discrepancy between model-derived ionospheric and tropospheric delay predicted values and the actual values which increase with larger sampling intervals. There is also a trend in the code residual r.m.s. which indicates that with increasing sampling intervals, the code residual r.m.s. is decreasing. In Beran et al. [2005] and in Figure 5.7 and Figure 5.8, it could be found that this is mainly due to the decrease in the standard deviations. This

could be explained by the second hypermatrix in equation (4.2), which includes multiplications of the t and t-1 epoch geometry matrices ($\mathbf{A}_{t-1}$ and $\mathbf{A}_t$). The matrix multiplication indicates that the more significant between-epoch geometry change which occurs, the more useful the delta-phase measurements, and subsequently the "smoother" the resulting estimate.

Sampling Interval [s]	1*	5*	10*	30*,**	60**	120**	240**
N r.m.s. [m]	0.36	0.26	0.24	0.21	0.17	0.31	0.39
E r.m.s. [m]	0.26	0.20	0.17	0.15	0.19	0.27	0.44
Height r.m.s. [m]	0.86	0.63	0.55	0.61	0.59	0.47	1.19
Code Res. [m]	0.48	0.51	0.52	0.52	0.50	0.43	0.38
dPhase Res. [cm]	2.1	2.6	2.9	4.0	5.0	6.6	8.2

Table 5.5: Sampling intervals and position error r.m.s. and code and delta-phase residual for the Algonquin Park 1 second data down-sampled to the other sampling intervals. *) Sampling intervals are shown in Figure 5.7 ; **) and Sampling intervals are shown in Figure 5.8,

Between sampling intervals of 10 and 30 seconds, results with minimum positioning differences are obtained. From Figure 5.8 it could be seen that sampling intervals of 1 minute to 4 minutes cause large variations and the filter residual outlier detection algorithm rejects too many measurements and the point positioning software produces code-only solutions.

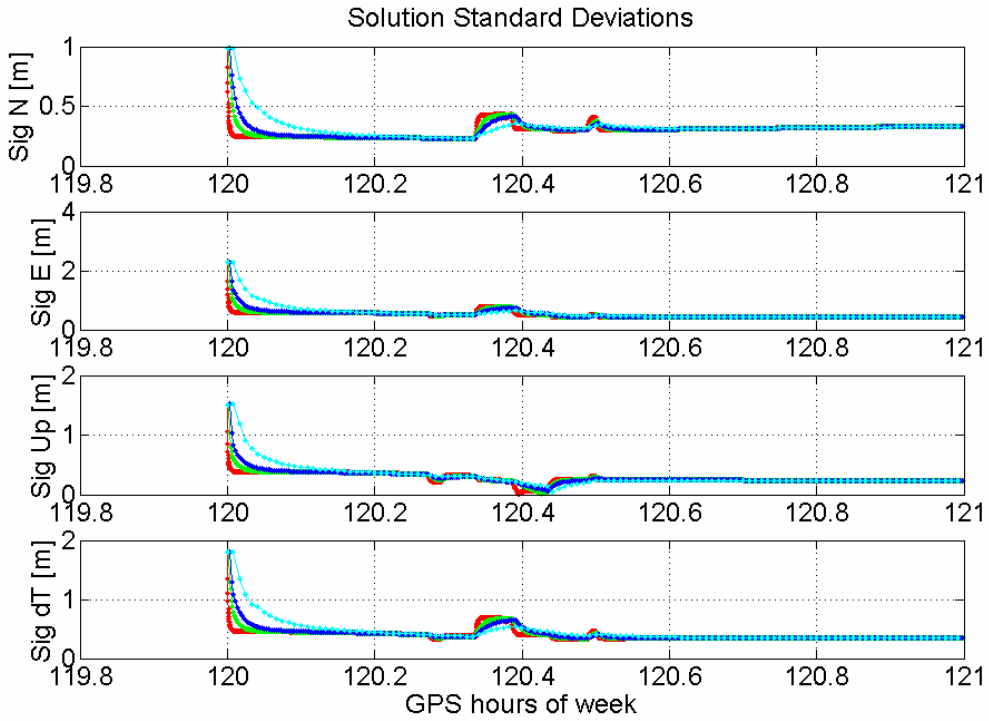

Figure 5.9: Position solution standard deviations for the Algonquin Park station on different datasets with different sampling intervals: (red) 1 second, (green) 5 second, (blue) 10 second, and (cyan) 30 second sampling rates respectively.

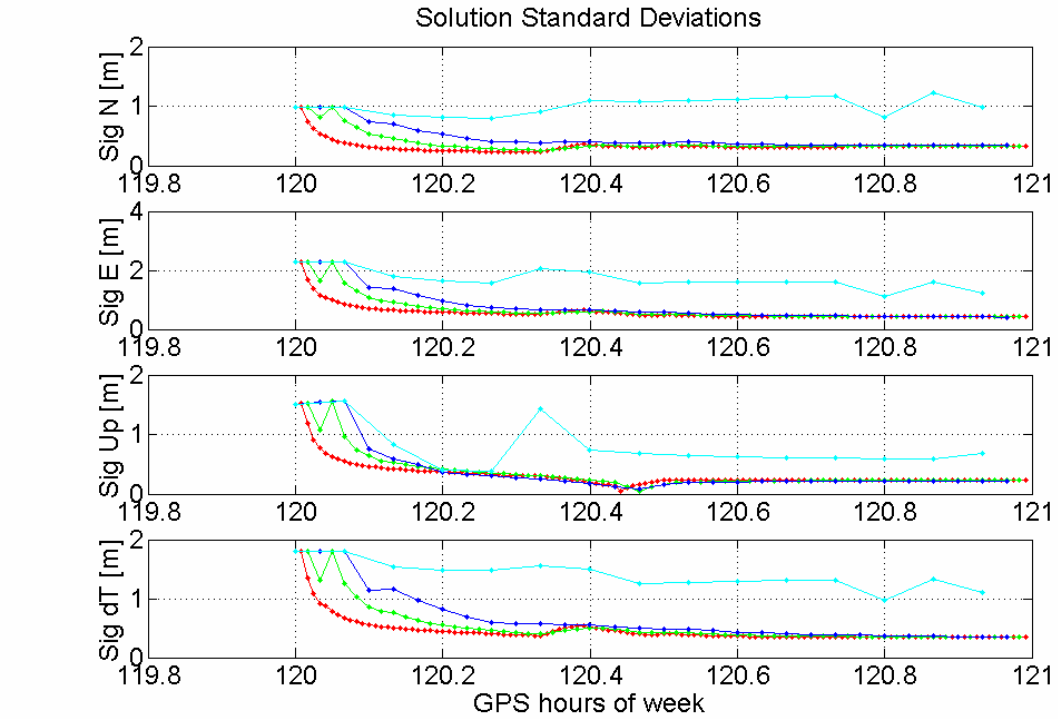

Figure 5.10: Position solution standard deviations for the Algonquin Park station on different datasets with different sampling intervals: (red) 30 second, (green) 1 minute, (blue) 2 minute, and (cyan) 4 minute sampling rates respectively.

From Figure 5.9, the filter convergence time in epochs is similar using 1 second and 30 second sampling intervals. Figure 5.10 shows that the 1 to 4 minute sampling datasets are converging with difficulties, or not converging (see the code-only solution comment above). In conclusion, the 30 second sampling interval is the largest sampling interval when the solution standard deviation still converges. It is desirable to use larger sampling intervals for static applications, but for kinematic applications this may not be an option.

The important findings in this section are that the relationship between the sampling interval and the position component r.m.s. is a result of the above opposite trends in code

residual r.m.s. and delta-phase residual r.m.s. and the sampling interval, and for that reason there is a finite range of sampling intervals where the position component r.m.s. is at a minimum. This range seems to be between 10 and 30 second sampling interval. It was also found that the filter does not converge continuously with sampling intervals larger than 30 seconds and for that reason the sampling intervals larger than 30 seconds should be avoided.

5.2.2 Convergence Interval Testing

The relationship between the pseudorange and carrier-phase weighting and filter convergence time was tested on Algonquin Park station data from September 2, 2005, using 30-second and 1-second sampling rate datasets. For the purpose of this test, the convergence time in the case of the pseudorange and time-differenced carrier-phase filter is defined as the time interval from the initial code-only solution to the time when the precision (formal standard deviation) of the estimated parameters reaches the values observed with the 24-hour data solution. Figure 5.11 and Figure 5.12 show the convergence intervals for 30-second and 1-second datasets (30 epochs in both cases) with 5 m, 2 m, 1 m and 0.5 m a priori code observation noise.

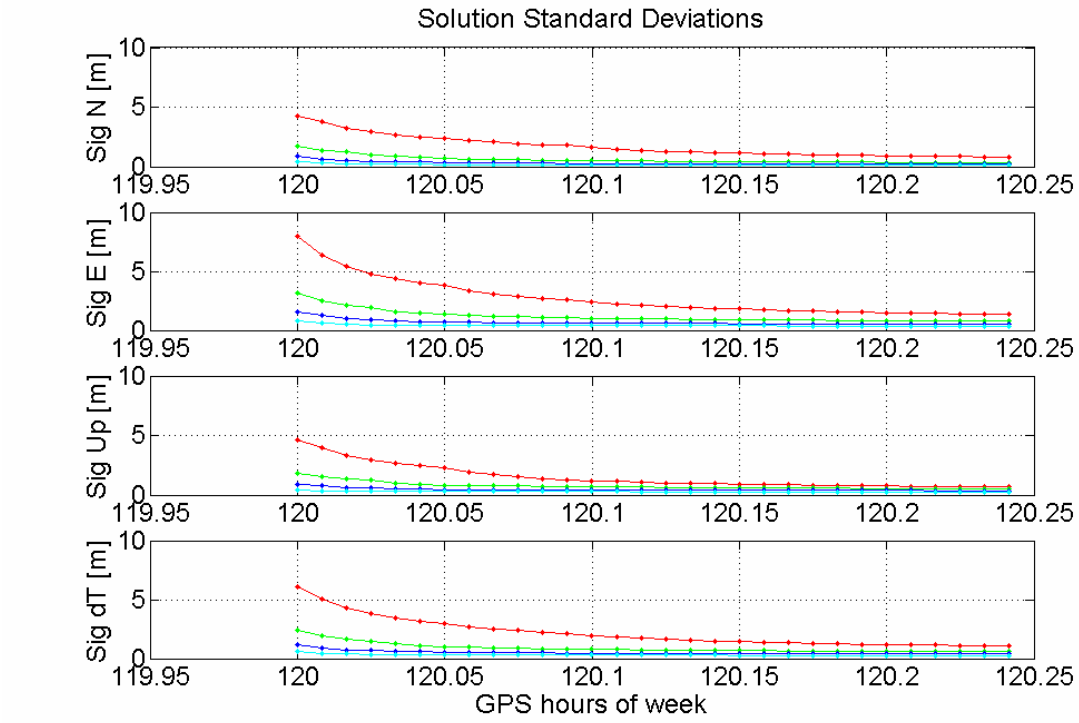

Figure 5.11: Initial 30 epochs of 30-second sampling rate data from Algonquin Park station with phase noise of 5 cm and code noise of: (red) 5 m, (green) 2 m, (blue) 1 m and (cyan) 0.5 m. Displayed period of time is about 15 minutes.

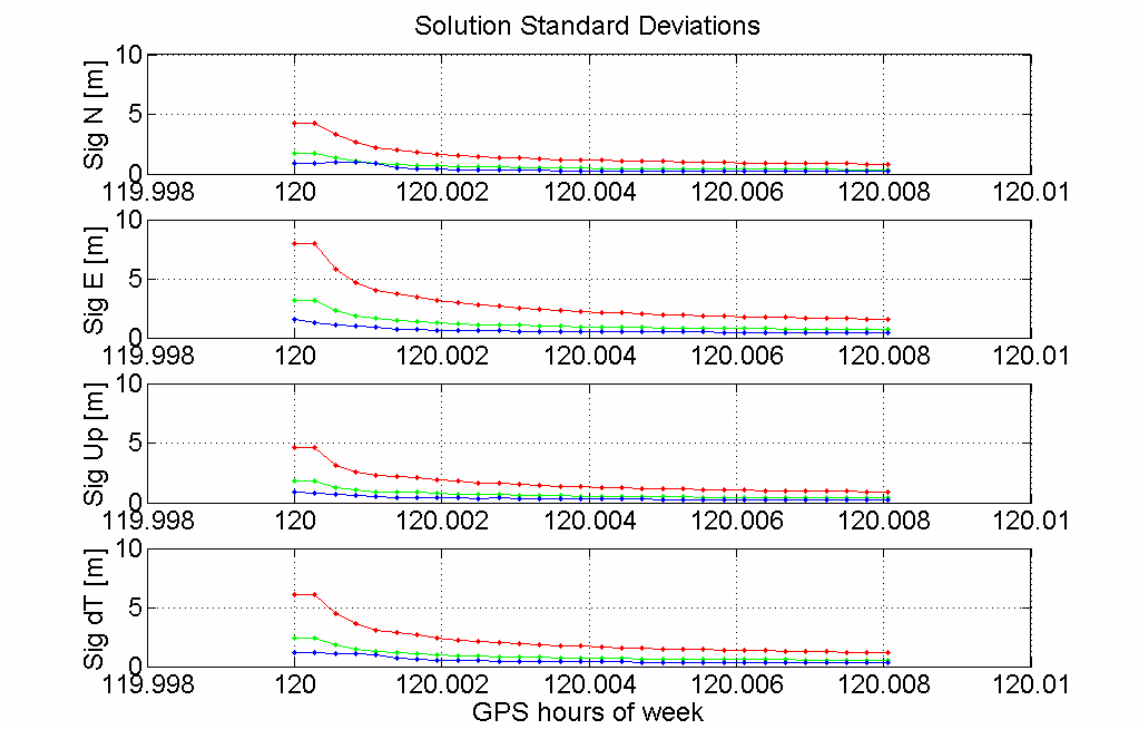

Figure 5.12: Initial 30 epochs of 1-second sampling rate data from Algonquin Park station with phase noise of 5 cm and code noise of: (red) 5 m, (green) 2 m, and (blue) 1 m. Displayed period of time is about 30 seconds.

Table 5.6 and Table 5.7 show the code and phase residual r.m.s. for different observation noise settings on the 30-second dataset. The code noise ranged from 0.5 m to 5 m. 5-metre-level code noise values are common values in multipath contaminated environments and 0.5 m is the minimum code noise value for Garmin 25LP OEM used in van Leeuwen's tests [van Leeuven, 1998]. The phase noise ranges from 5 cm to 50 cm. 50 and 20 cm are unrealistic large values that was chosen only for testing purposes. 5 cm is derived from the minimum noise value from van Leeuwen's tests [van Leeuven, 1998] according to the law of propagation of errors. Neither code nor delta-phase residual r.m.s. change significantly for different measurement noise settings if the measurement noise values are realistic.

Code Residual r.m.s. [cm]				
Phase / Code	50	20	10	5 [cm]
5	33	33	38	37
2	31	33	33	33
1	29	32	33	33
0.5 [m]	26	30	32	32

Table 5.6: Code residual r.m.s. for different code and phase observation noise settings on a 30-second dataset.

dPhase Residual r.m.s. [cm]				
Phase / Code	50	20	10	5 [cm]
5	4.7	4.9	7.0	5.8
2	7.1	4.7	4.6	4.3
1	11.2	6.2	4.7	3.9
0.5 [m]	17.1	9.6	6.2	4.2

Table 5.7: Delta-phase residual r.m.s. for different code and phase observation noise settings on a 30-second dataset.

The length of the convergence interval varies between 10 and 20 epochs for different observation noise settings. Realistic code and phase measurement noise values correspond to the upper bound of r.m.s. of measurement residuals after the adjustment. For optimal results it is recommended to use 5-metre-level values for the code measurement noise and 10-centimetre-level delta-phase measurement noise for the initial run of the filter and then repeat the filter run with the new set of measurement noise values obtained from the residuals. This is only possible when the filter is run in the post-processing mode. In theory, this type of filter can operate in real-time mode and this option will be discussed in chapter 7. If the measurement noise values are too optimistic,

the residual outlier detection algorithm rejects correct observations and the results are actually worse.

5.3 Terrestrial Data Testing

A series of tests was performed first to investigate the difference between a geodetic-quality GPS receiver and a low-cost GPS receiver. In the first test, data from a low-cost receiver and geodetic quality receiver were collected and compared in a kinematic experiment. The least-squares filter remains the same in all these tests, but different receivers, different sites and different atmospheric conditions lead to different results. In sub-section 5.3.1, 24-hour datasets from two different sites, equipped with GPS receivers of different quality will be compared.

5.3.1 Static Data Testing

The purpose of the first static test was to compare the results from high-quality (IGS reference station at the University of New Brunswick (UNB), Fredericton Campus, Canada) and low-quality (coordinated control point, Lincoln Heights, Fredericton, Canada) GPS data covering the same period of time on 2 September 2005. The IGS reference station at the University of New Brunswick (UNB1) is equipped with a Javad Legacy GPS receiver with a Javad Regant Dual-Depth choke-ring antenna. There is no

external clock on site. Only single-frequency, 30 s measurements were used in the UNB1 data processing. A Garmin GPS 35 TracPak, a complete GPS receiver and embedded antenna unit, was placed on a coordinated control point in Lincoln Heights, in Fredericton. A Garmin binary stream was collected by a PC, and the binary data was converted into RINEX 2.1 format [Gurtner, 2002] using a RINEX converter at the Geodetic Research Laboratory at the University of New Brunswick. Garmin Lincoln Heights GPS data were collected at 1-second sampling rate and down-sampled from 1 s to 30 s (see sub-section 5.2.1 for more information on the choice of the sampling rate) for one of the testing datasets. A 15-degree elevation angle cut-off was applied to both datasets. The pseudorange and time-differenced carrier-phase filter model was used for the processing. The IGS composite final ionospheric grid map was used to model the ionospheric delays. The a-priori code measurement standard deviation (σ_P) was 1 m and the a-priori delta-phase measurement standard deviation (σ_Φ) was 2 cm.

The results of the UNB1 station single-frequency processing are presented in Figure 5.13 and Figure 5.14. The north, east and up component error values were computed by subtracting the reference IGS coordinates from the estimated position. Peak-to-peak variation of 2 m in northing error time series around hour 140 is caused by ionospheric model error on a rising satellite.

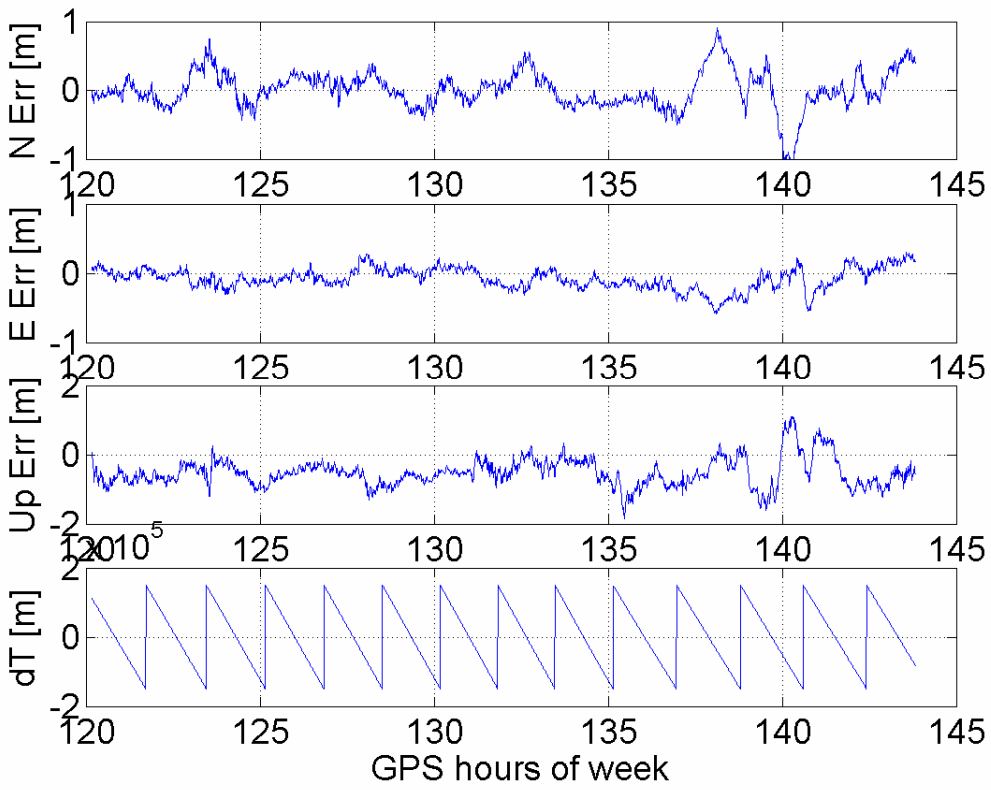

Figure 5.13: Position component and receiver clock errors of the geodetic-quality GPS receiver (UNB1 IGS station) L1 + global ionospheric model data processing, $\sigma_P = 1.0$ m; $\sigma_\Phi = 0.02$ m.

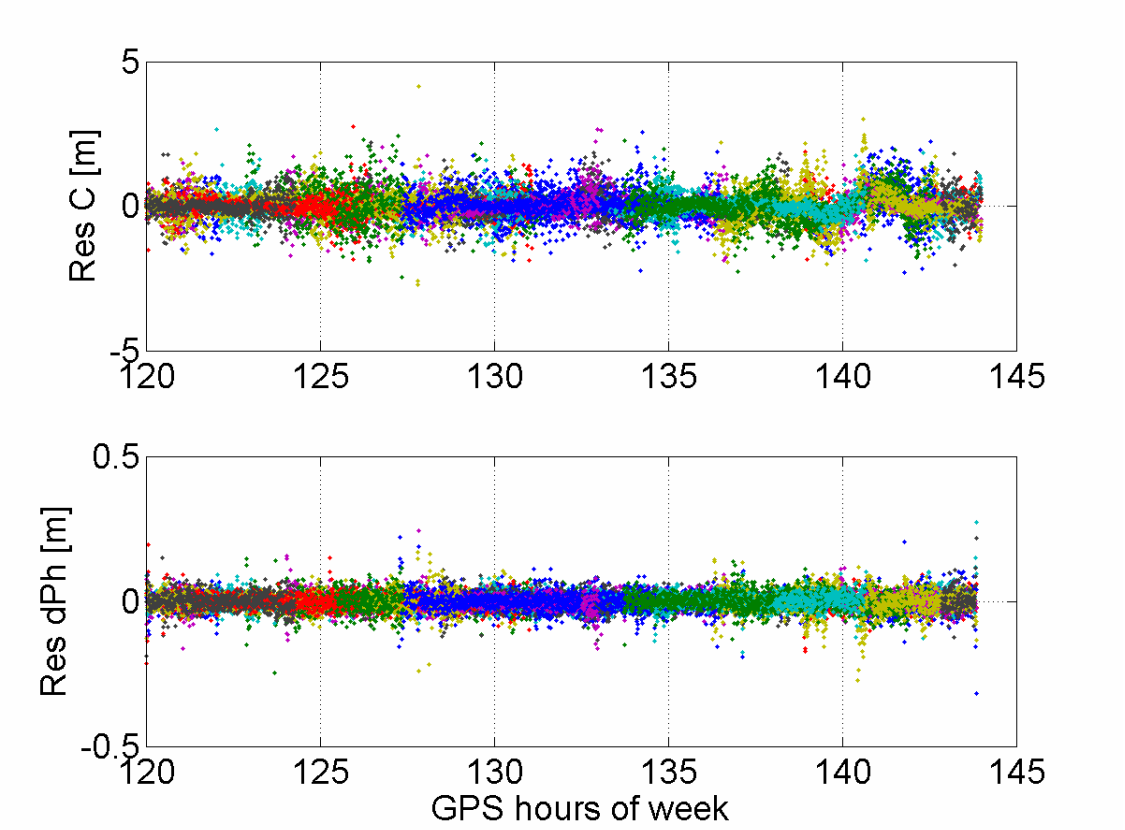

Figure 5.14: Filter residuals from geodetic-quality GPS receiver (UNB1 IGS station) L1 + global ionospheric model data processing, $\sigma_P = 1.0$ m; $\sigma_\Phi = 0.02$ m. Top: pseudoranges. Bottom: carrier-phase differences.

UNB1 results in Table 5.8 and the Algonquin Park results in the Table 5.2 vary in size of the height component biases compatible with the results for the 24-hour Algonquin Park processing (Table 5.2), because the two datasets were obtained on different days under different atmospheric conditions. On the same day, -1.4 cm , 2.3 cm and -49.4 cm are the mean difference values in north, east, and height components, respectively for the UNB1 single-frequency data and -6.2 cm, 5.5 cm, and -41.5 cm are the mean difference values in north, east, and height components, respectively for the ALGO data. Position error standard deviations and r.m.s., and code and delta-phase residual r.m.s, are also compatible. Bias in the height component for ionosphere-free data processing for ALGO

is -9.2 cm while it is about -20.2 cm for UNB1 ionosphere-free processing, which indicates that about 40 cm up component bias on both stations is caused by the ionospheric model error in the single-frequency data processing.

Position Error Components [cm]			
	North	**East**	**Height**
Mean	-1.4	-2.3	-49.4
	-3.1	*-2.0*	*-20.2*
Std. Dev.	27.3	15.4	40.5
	30.6	*18.8*	*53.4*
r.m.s.	27.3	15.5	63.9
	30.7	*18.9*	*57.1*
Measurement Residual r.m.s. [cm]			
Code	55.2	dPhase	8.0
	128.5		*14.0*

Table 5.8: Single-frequency (L1 + global ionospheric model) and ionosphere-free (italics) data processing statistics for a geodetic-quality GPS receiver (24-hour UNB1 dataset) ignoring the initial 20 epochs of data.

The dual-frequency UNB1 data were also processed with the CSRS-PPP engine. The mean differences between the IGS reference coordinates and CSRS-PPP are -0.6 cm, -1.4 cm, and 2.6 cm in north, east, and height components, respectively. The differences between the CSRS-PPP and the IGS reference position are compatible with those of the ALGO dataset. The standard deviations for the CSRS-PPP processing are 0.3 cm, 0.6 cm, and 1.3 cm in north, east, and height components, respectively, which are similar to ALGO dataset processing results.

The CSRS-PPP was used to process the data from the low-cost receiver from Lincoln Heights. The CSRS-PPP software was able to process the pseudorange data, but it was not able to process the carrier-phase data. This is likely caused by the cycle-slips and the noise in the carrier-phase observations which is about three-times larger in low-cost receivers than in geodetic quality receivers. The ability of our software to handle carrier-phase data is critical, so the low-cost receiver data processing analysis starts with an examination of the delta-phase residual outlier detection algorithm.

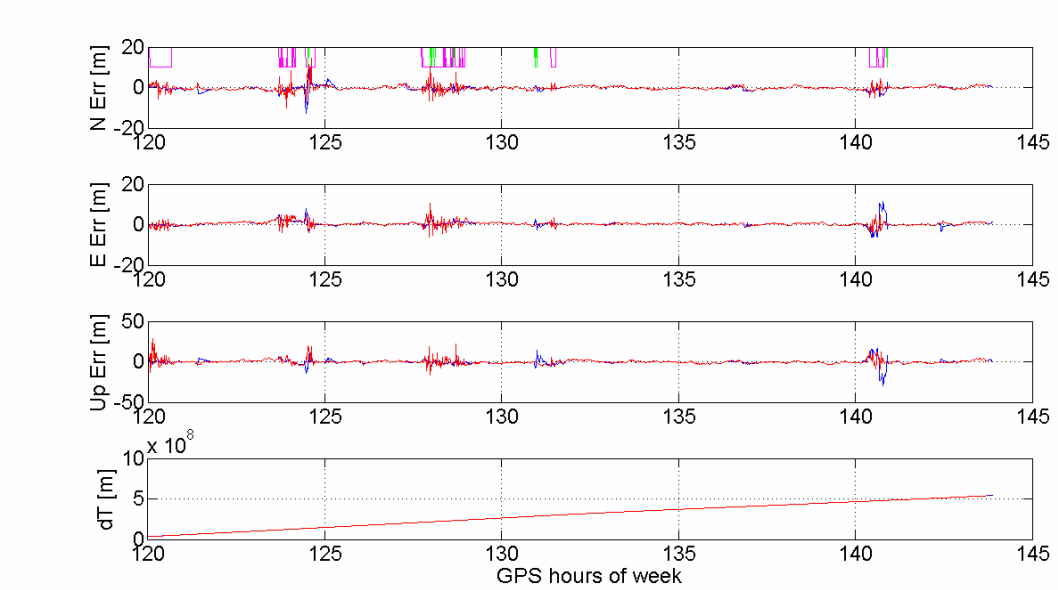

Figure 5.15: Position component and low-cost GPS receiver clock errors when the outlier detection algorithm is disabled (blue; sol. type: green) and when it is enabled (red; sol. type: magenta) in -20 to 20 m horizontal scale. Green and magenta lines: 20 m code and delta-phase solution; 10 m code-only solution, $\sigma_P = 2.0$ m; $\sigma_\Phi = 0.1$ m for both solutions.

The functionality of the delta-phase residual outlier detection algorithm on low-cost receiver data is demonstrated on Figure 5.15. Blue line shows the position component and receiver clock errors of the Lincoln Heights station data when the outlier detection

algorithm is disabled and red line shows the same results when the outlier detection algorithm is enabled. Green line at the top of the north error plot has a value of 20 m for code and delta carrier solutions and value 10 m for code only solutions corresponding to the outlier detection algorithm is disabled (blue) time series. Magenta line with the same values corresponds to the outlier detection algorithm is enabled (red) time series.

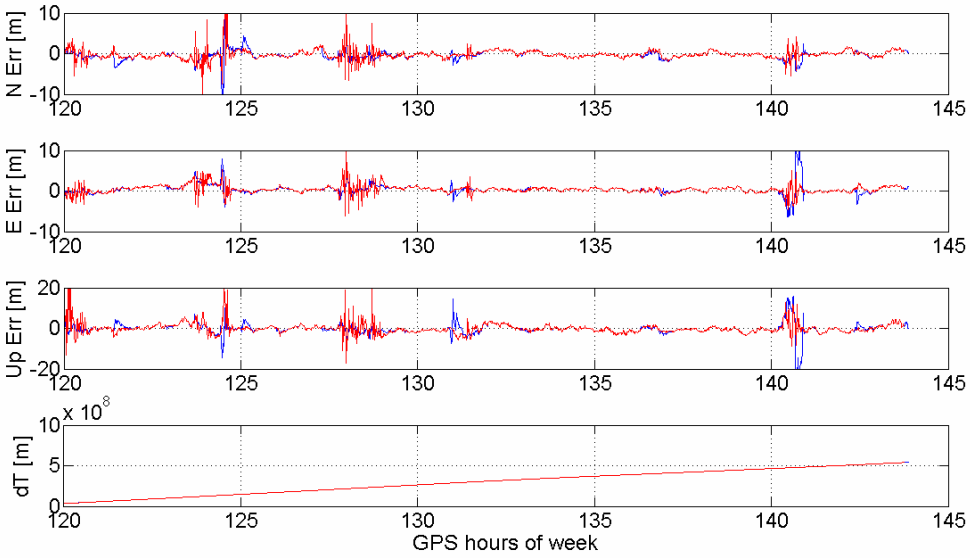

Figure 5.16: Position component and low-cost GPS receiver clock errors when the outlier detection algorithm is disabled (blue) and when it is enabled (red) in -10 to 10 m horizontal scale, $\sigma_P = 2.0$ m; $\sigma_\Phi = 0.1$ m for both solutions.

The results in Table 5.9 show a significant difference in the position error r.m.s. when the outlier detection algorithm is disabled and when it is enabled. This difference is caused by presence of discontinuities (cycle slips or lost of lock events) in the delta carrier phase observations. Lost of lock events, indicated by a square on the elevation angle time series, for the first 12 hours of data are shown in Figure 5.17. From this plot

one can see that the residual outlier detection algorithm is mostly triggered by low elevation angle satellites. Presence of cycle slips on 4-hour part of the Lincoln Heights dataset is shown on Figure 5.18. Cycle slips on this plot are shown as sudden shifts that are larger than 1 cycle. From this plot it can be concluded that e.g. the discontinuity at hour 124 in Figure 5.16 is caused by a cycle slip on PRN 23. The total number of solutions in this dataset is 2880. Once the residual outlier detection algorithm is enabled the code and delta-phase solutions are available only in 93% of all solutions. If the apriori measurement noise values are too optimistic, i.e. the noise value used in the filter is lower than the actually value, the outlier detection algorithm starts rejecting measurements and the filter eventually resets itself to the code only solutions.

Position Error Components r.m.s. [cm]				
Outlier Detection	**North**	**East**	**Height**	**Number of Code-dPhase Solutions**
Disabled	162	136	422	2851 (99%)
Enabled	76	76	167	2672 (93%)

Table 5.9: Position component and low-cost GPS receiver clock error r.m.s.s and number of code and delta-phase solutions (L1 + global ionospheric model) when the outlier detection algorithm is disabled and when it is enabled, $\sigma_P = 2.0$ m; $\sigma_\Phi = 0.1$ m for both solutions.

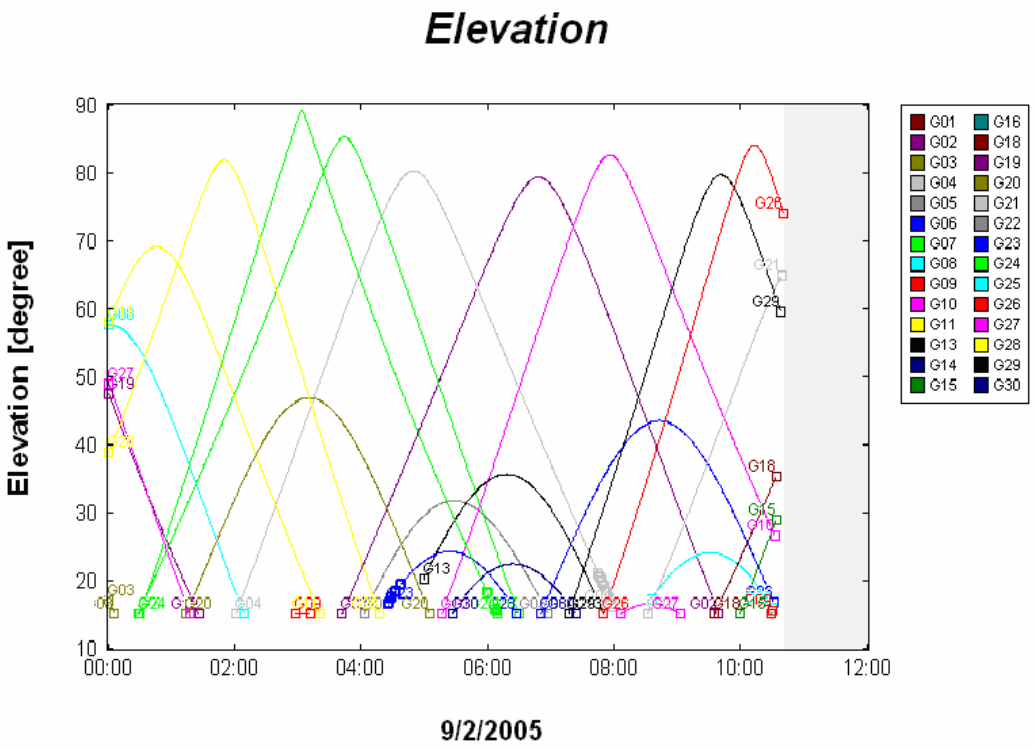

Figure 5.17: Elevation angles of satellites above 15 ° observed by the low-cost GPS receiver (Lincoln Heights station). Squares indicate loss of lock events.

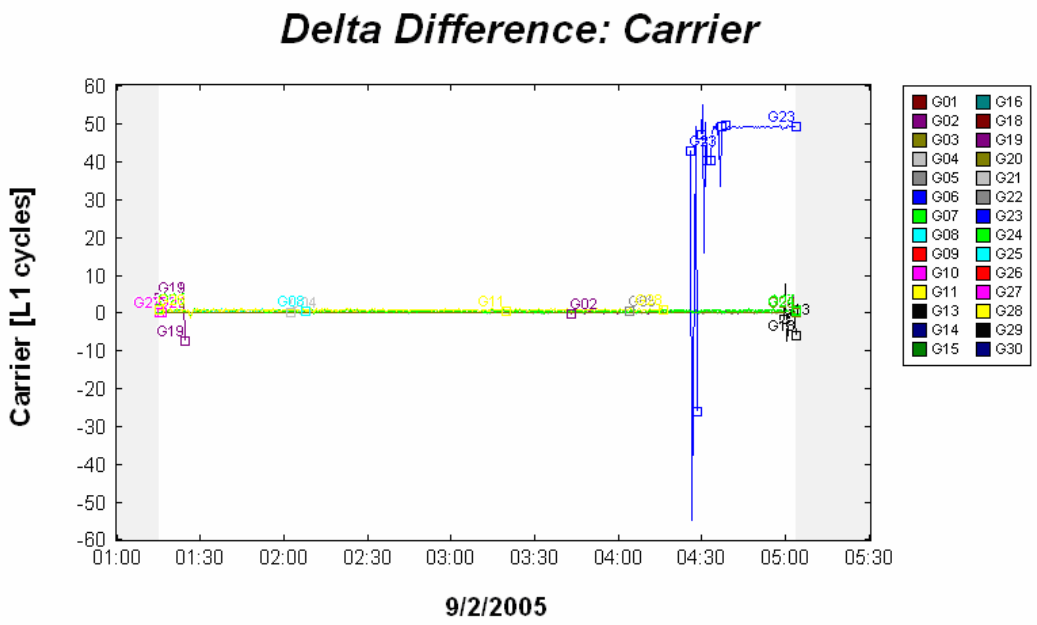

Figure 5.18: Between satellites single-differenced (ref. satellite PRN 20), time difference carrier-phase observations above 15° elevation angle observed by the low-cost GPS receiver (Lincoln Heights station).

The sensitivity of the delta-phase residual outlier detection algorithm on low-cost receiver data depends on the choice of the assumed apriori phase-measurement noise values. The following set of plots shows the results of the Lincoln Heights dataset processing with carrier-phase measurement noise values from 0.06 m to 0.10 m. A carrier-phase measurement noise value of 0.12 m was tested, but plot is not included. Similar testing using different pseudorange measurement noise values from 2.0 m to 10.0 m range were also performed, but there was no significant difference in the delta-phase outlier detection function. Pseudorange measurement noise values lower than 2.0 m cause numerical problems in the solution.

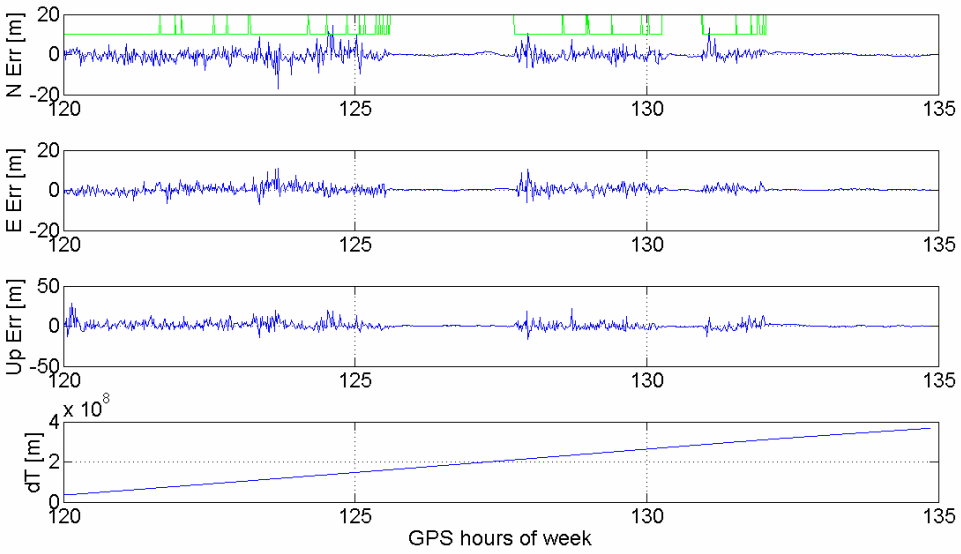

Figure 5.19: Position component and clock errors from low-cost GPS receiver data processing (Lincoln Heights station) with $\sigma_P = 2.0\,\text{m}; \sigma_\Phi = 0.06\,\text{m}$ for both solutions. Green line: 20 m code and delta-phase solution; 10 m code-only solution (both solutions use L1 + global ionospheric model).

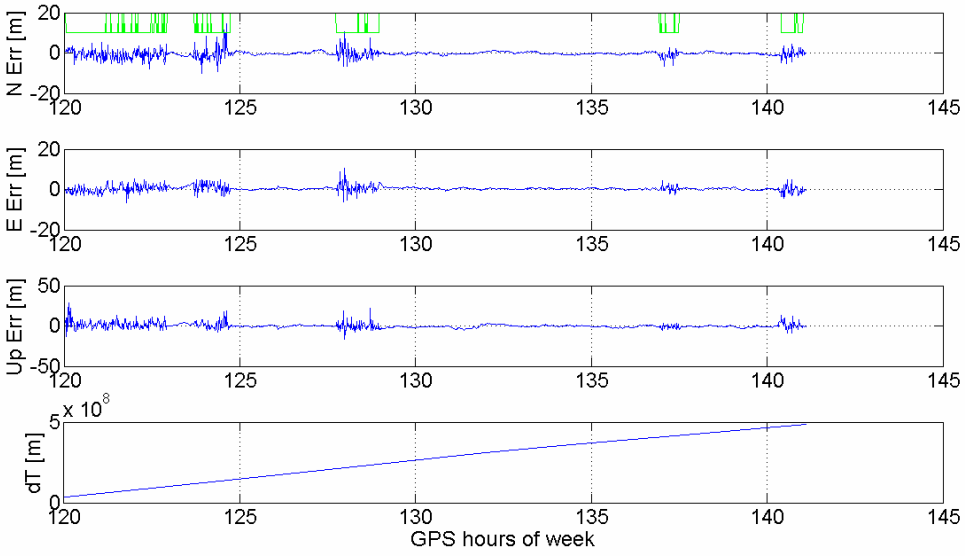

Figure 5.20: Position component and clock errors from low-cost GPS receiver data processing (Lincoln Heights station) with $\sigma_P = 2.0\,\text{m}; \sigma_\Phi = 0.08\,\text{m}$. Green line: 20 m code and delta-phase solution; 10 m code-only solution (both solutions use L1 + global ionospheric model).

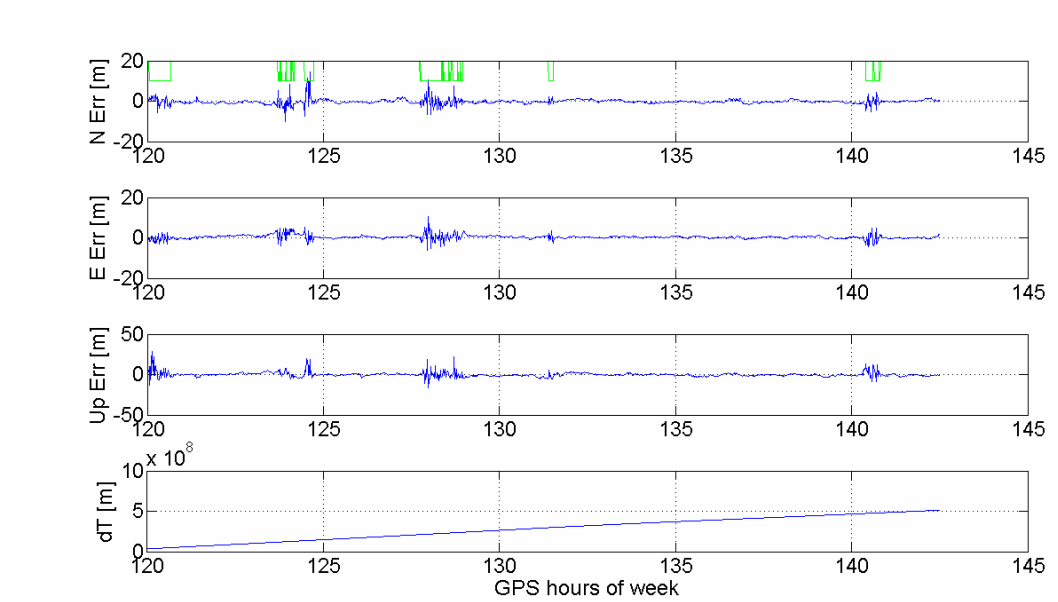

Figure 5.21: Position component and clock errors from low-cost GPS receiver data processing (Lincoln Heights station) with $\sigma_P = 2.0\,\text{m}; \sigma_\Phi = 0.10\,\text{m}$. Green line: 20 code and delta-phase solution; 10 code-only solution (both solutions use L1 + global ionospheric model).

The summary statistics in Table 5.10 shows position component r.m.s. and the percentage of the results with code and delta-phase solutions. The summary statistics in Table 5.10 reflects code and delta-phase solutions only. In order to choose the optimal measurement noise, maximum availability of code and delta-phase solutions and minimum position component r.m.s. criteria were used. Pseudorange measurement noise of 2.0 m and carrier-phase noise of 0.1 m satisfy both criteria.

Position Error Components r.m.s. [cm]				
Measurement Noise	North	East	Height	Number of Code-dPhase Solutions
$\sigma_P = 200$ $\sigma_\Phi = 6$	76	51	126	1203 (42%)
$\sigma_P = 200$ $\sigma_\Phi = 8$	72	71	162	2141 (74%)
$\sigma_P = 200$ $\sigma_\Phi = 10$	76	76	167	2672 (93%)
$\sigma_P = 200$* $\sigma_\Phi = 12$*	89*	83*	216*	2615* (91%)

Table 5.10: Position component r.m.s. and the percentage or the results with code and delta-phase solutions (all solutions use L1 + global ionospheric model) from low-cost GPS receiver data processing (Lincoln Heights station). Note: * values do not have a corresponding plot.

The single-frequency code and single-frequency code and delta-phase processing results of the Lincoln Heights data processing are presented in Figure 5.22 and Figure 5.23. Green line with value of 10 m on Figure 5.22 and missing data in the bottom plot in Figure 5.24 reflect a code-only solution, selected by the filter because of rejected measurements in the outlier detection algorithm and subsequent returns to code-only solution. Rejected measurements are caused by the presence of cycle slips or other errors resulting in residual outliers. Residual outliers are identified using measurement noise values specified in a priori filter settings. Reference coordinates of the Lincoln Heights control point monument were obtained from UNB1 - Lincoln Heights control point baseline processing. A Trimble 5700 GPS receiver with the Zephyr geodetic antenna at

the Lincoln Heights control point collected data for 24 hours at 30 second sampling interval. UNB1 IGS station equipment has been described earlier. The Trimble Total Control GPS processing software was used for the baseline processing. L1 fixed solution was generated. UNB1 IGS coordinates were used in the processing.

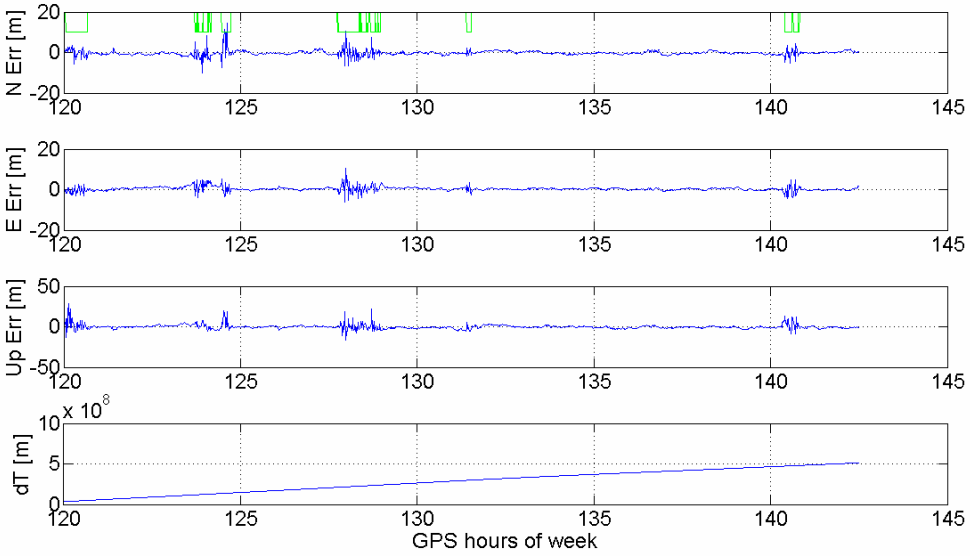

Figure 5.22: Position component and clock errors from low-cost GPS receiver data processing (Lincoln Heights station) in -20 to 20 m horizontal scale. Green line: 20 m code and delta-phase solution; 10 m code-only solution, $\sigma_P = 2.0\,\text{m}; \sigma_\Phi = 0.10\,\text{m}$ (both L1 + global ionospheric model).

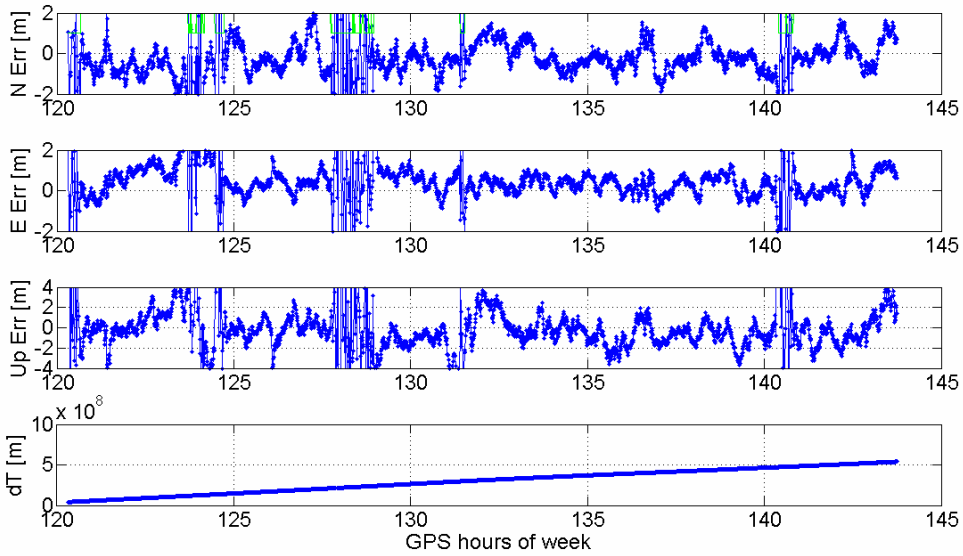

Figure 5.23: Position component and clock errors from low-cost GPS receiver data processing (Lincoln Heights station), $\sigma_P = 2.0\,\text{m}; \sigma_\Phi = 0.10\,\text{m}$ (both solutions use L1 + global ionospheric model).

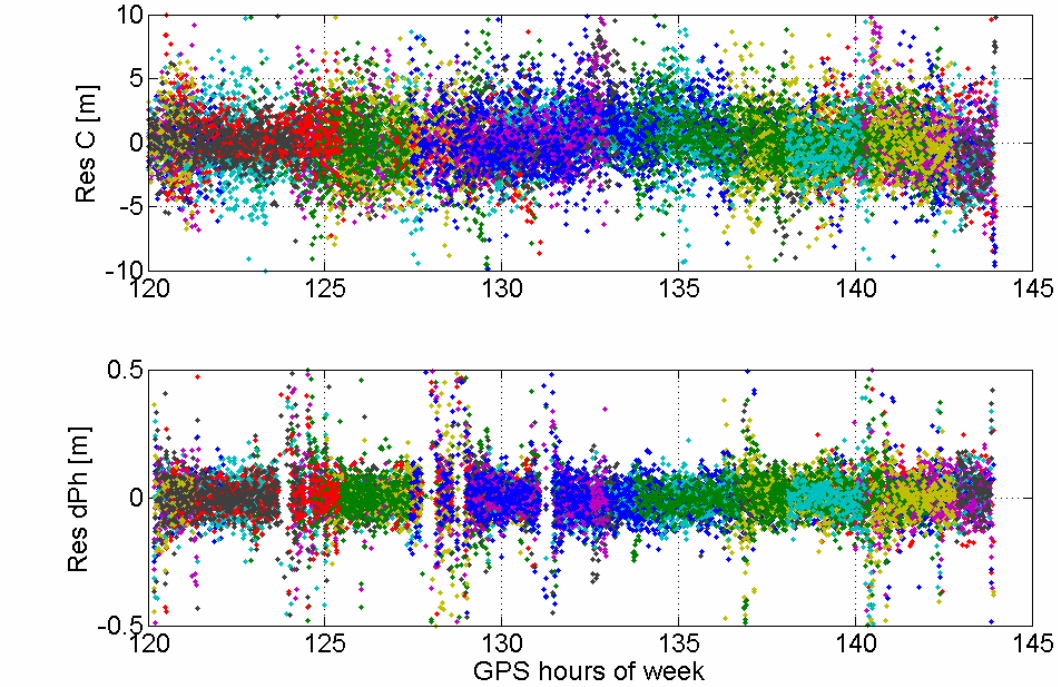

Figure 5.24: Filter residuals from low-cost GPS receiver data processing (Lincoln Heights station, $\sigma_P = 2.0\,\text{m}; \sigma_\Phi = 0.10\,\text{m}$, L1 + global ionospheric model). Top: pseudoranges. Bottom: carrier-phase differences. Please note the different scales when comparing these results with Figure 5.14.

Table 5.11 shows the statistics of the results from epoch 21 to the end of the dataset. Initial 20 epochs are excluded from the statistics because of the filter convergence period. The values in the table are still affected by the filter resets to the code-only solution, which cause multiple convergence periods to occur in the data processing statistics. During the 24-hour period of data, these resets occur more than eleven times, when the delta-phase residual outlier is not identified. The resets occur nine times because of the presence of cycle slips on low elevation angle satellites and two times the reset was caused by false outlier detection (for more details, see the analysis above). Decimetre-level horizontal position biases are present because some point positioning specific

considerations that are not included in the model and errors in the external atmospheric models. Ionospheric model errors could be an order of magnitude larger than tropospheric model errors. It is important to keep in mind that the measurement noise standard deviations in this case are more than twice the sizes the values used in the UNB1 dataset. The noticeable trend in code measurement residuals (top portion of Figure 5.24) is caused by the errors in the ionosphere model used in the single frequency processing and by site-specific phenomena such as code and carrier-phase multipath. A priori measurement noise values were chosen to be $\sigma_P = 2.0\,\text{m}; \sigma_\Phi = 0.10\,\text{m}$ to reflect findings described in sub-section 5.2.2 and the criteria described earlier in this section. Code and delta-phase measurement residuals (Figure 5.24) and the code and delta-phase measurement residual statistics (Table 5.11) reflect the differences in the measurement quality. These differences are caused by use of different antennas, different receivers, and different multipath conditions.

Position Error Components [cm]			
	North	East	Height
Mean	-22.7	41.6	-29.5
Std. Dev.	72.9	64.2	164.8
r.m.s.	76.3	76.4	167.4
Measurement Residual r.m.s. [cm]			
Code	222.6	dPhase	14.4

Table 5.11: Data processing statistics from low-cost GPS receiver data processing (Lincoln Heights station). L1 code and delta-phase (L1 + global ionospheric model) processing statistics ignoring the initial 20 epochs of data.

5.3.2 Kinematic Data Testing

Kinematic data were collected on 11 December 2005. A Trimble 5700 dual-frequency, geodetic-quality GPS receiver with a Zephyr antenna and a Garmin GPS 35 TracPak, a complete GPS receiver and embedded antenna unit, were mounted on the roof of a car. The car was driven on two and four-lane highways and residential areas of Fredericton, New Brunswick, Canada for more than 2 hours.

The reference solution for the Trimble antenna position was a kinematic baseline solution obtained with commercial GPS processing software with a static reference station at Lincoln Heights control monument equipped with a Trimble 5700 GPS receiver with the Zephyr geodetic antenna. The Trimble Total Control (TTC) GPS processing software was used for the kinematic baseline processing and for the generation of figures for the data analysis (Figure 5.25, Figure 5.26, Figure 5.27 and other figures). Reference coordinates for the Lincoln Heights control monument were obtained from the UNB1 - Lincoln Heights baseline determination described in the previous section.

Figure 5.25 shows the timelines of the base and rover observation data with yellow marks indicating loss of lock events. Kinematic rover timeline shows more loss of lock events than the static base timeline which is expected. It seems that the second half of the rover timeline has less loss of lock events than the first half, but the processing results

represented by the plot of the L1 fixed residuals (Figure 5.26) shows more successful ambiguity resolution, and therefore a more reliable solution, in the first hour. Reliable ambiguity fixed solution seems to be available only in the first 15 minutes of the data. It is shown on Figure 5.26 between 18:30 and 18:45.

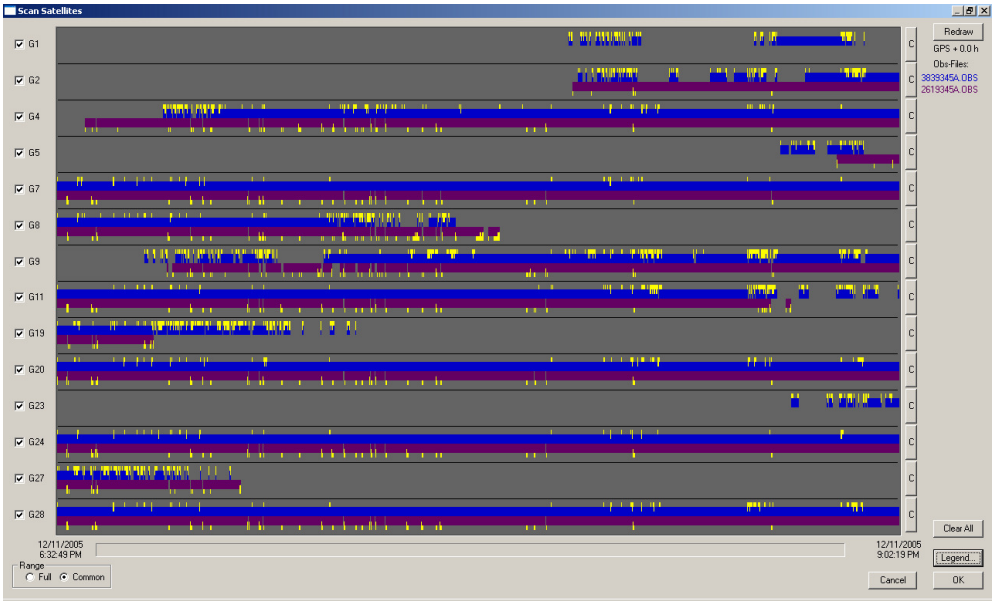

Figure 5.25: Geodetic-quality GPS receiver (Trimbe 5700) observations timeline: blue line shows the kinematic rover data and magenta line shows the static base data. Yellow marks indicate loss of lock events.

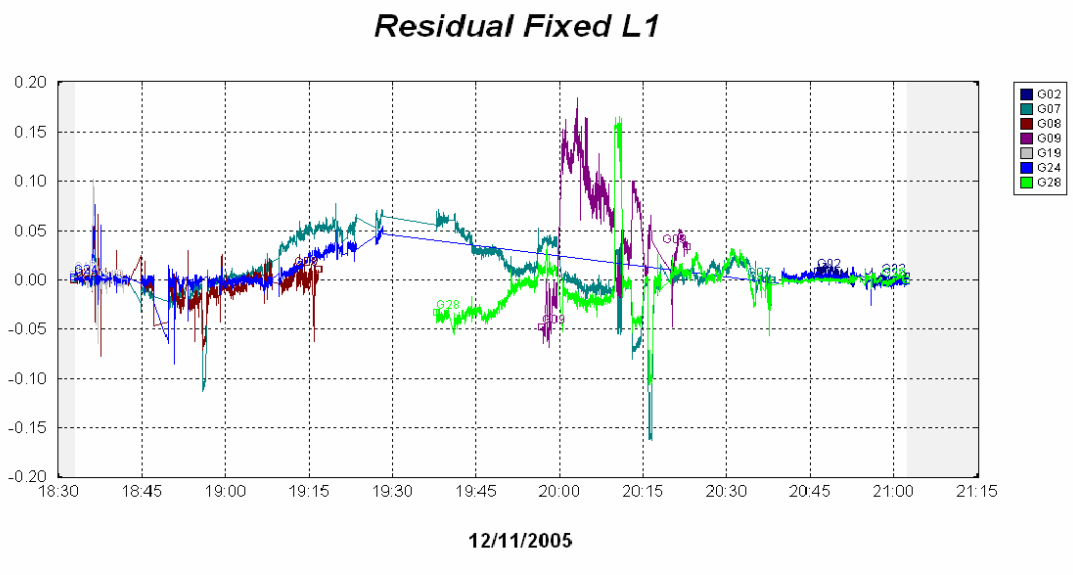

Figure 5.26: Geodetic-quality GPS receiver (Trimbe 5700) L1 fixed residuals [m] from the TTC kinematic processing.

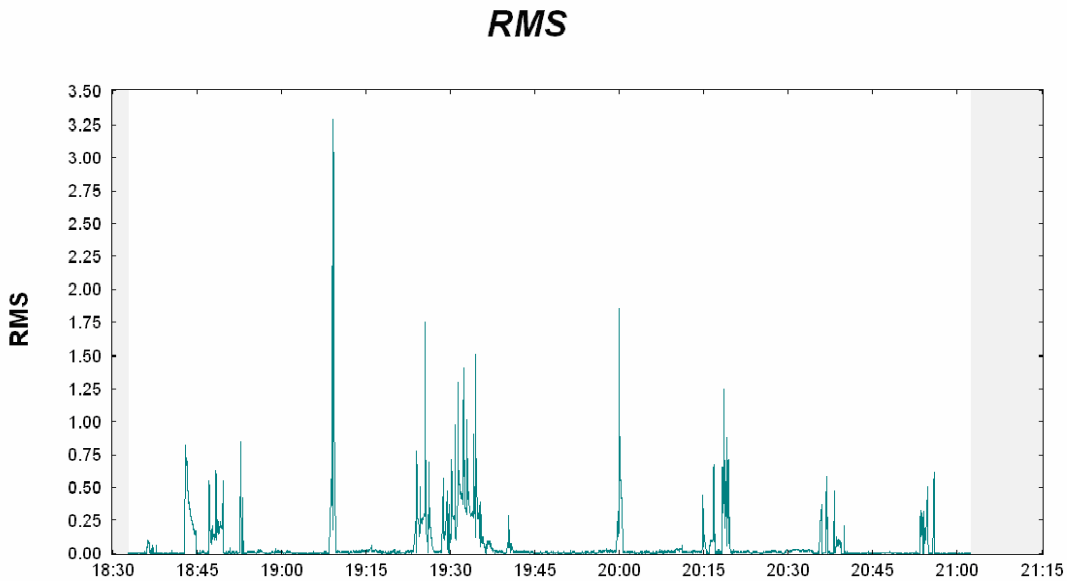

Figure 5.27: Geodetic-quality GPS receiver (Trimbe 5700) estimated position residuals [m] from the TTC kinematic processing.

Overall quality of the kinematic reference solution is shown on the plot of the r.m.s of estimated position residuals in Figure 5.27. Spikes in the plot indicate periods of time when the reference solution is not of cm level accuracy. An attempt was made to process the kinematic data with NovAtel's (formerly Waypoing Consulting Inc.) GrafNav processing software but the differences between the forward and reverse solutions show that the solution is not of cm level accuracy either.

There are multiple reasons why the Trimble 5700 reference kinematic dataset causes problems in the processing. The first reason is that the vehicle carrying the GPS receivers was passing under bridges which causes loss of lock events on all satellites. All passes under bridges were registered, so it is possible to identify these events from the timeline and from the background satellite image which was used in the TTC software. The second reason is satellite signal blockages caused by obstacles along the roads and highways. These events result in loss of lock, cycle slips, or increased multipath on low elevation angle satellites. The third reason is the reference baseline length. The maximum baseline length in this project is about 35 km which may cause further difficulties and less reliability in the ambiguity estimation process because of the presence of differential atmospheric errors.

The position differences between the single-frequency point positioning solution and the reference solution for a selected 1 hour of Trimble receiver data are presented in Figure 5.28. During the selected time interval, the test vehicle was driven mostly on four-lane highways. Variations and spikes on the time series are caused by point positioning

filter resets to code-only solutions. The first such reset happened just after hour 19.1 when the test vehicle passed underneath a bridge and the receivers lost the GPS signals. Figure 5.30 shows two loss of lock events just before 19:10. Filter resets to the code-only solutions are also apparent from the plot of time-differenced carrier-phase residuals, shown in the bottom part of Figure 5.29. The top part of the Figure 5.29 also shows a period of time after hour 19.8 when PRN 9, a rising low-elevation angle satellite, influenced the solution. This can be seen on PRN 9 timeline on Figure 5.30. The spikes at bottom part of the Figure 5.29 and the loss of lock and cycle slip events (see the explanation in Static Data Testing section) on Figure 5.31 coincide.

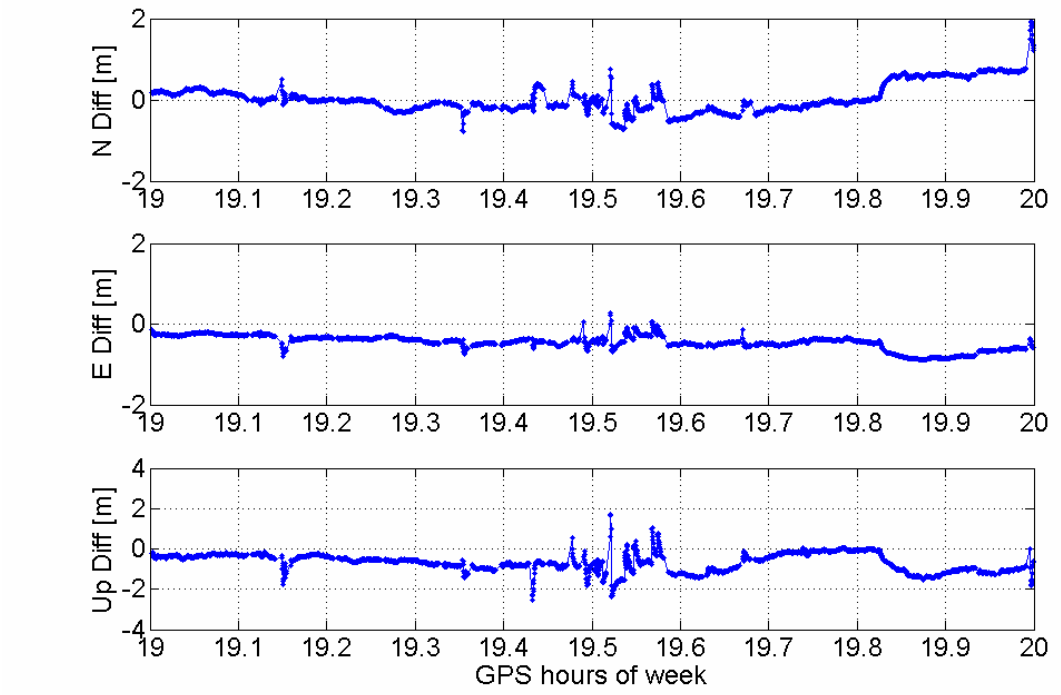

Figure 5.28: Position differences between the single-frequency (L1 + global ionospheric model) point positioning solution and the reference solution for Geodetic-quality GPS receiver (Trimbe 5700) receiver 1-hour data, $\sigma_P = 2.0\,\text{m}; \sigma_\Phi = 0.10\,\text{m}$.

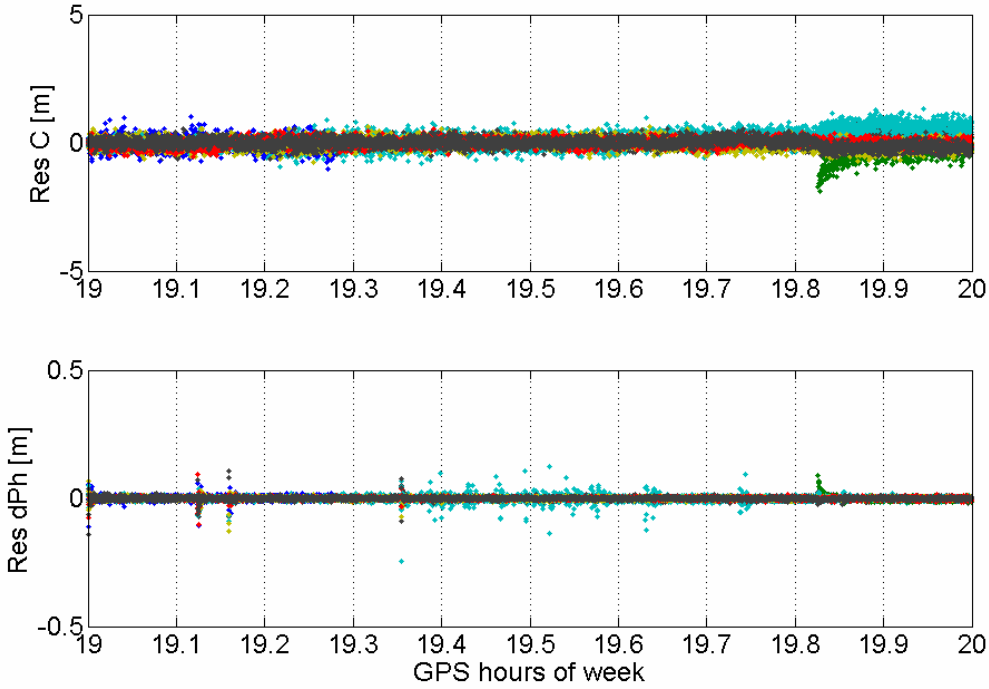

Figure 5.29: Filter residuals from the single-frequency point positioning solution (L1 + global ionospheric model) for Geodetic-quality GPS receiver (Trimbe 5700) receiver 1-hour data, $\sigma_P = 2.0\,\text{m}; \sigma_\Phi = 0.10\,\text{m}$. Top: pseudoranges. Bottom: carrier-phase differences

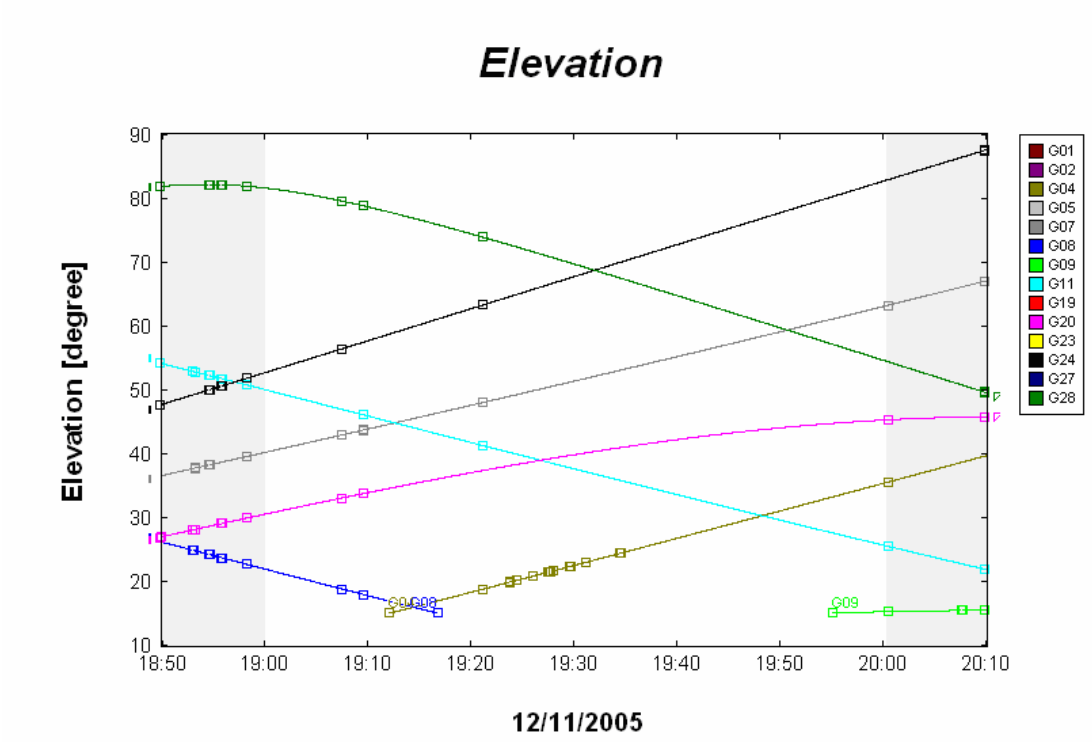

Figure 5.30: Elevation angles of satellites above 15° observed by the Geodetic-quality GPS receiver (Trimbe 5700) GPS receiver on the moving vehicle. Squares indicate loss of lock events.

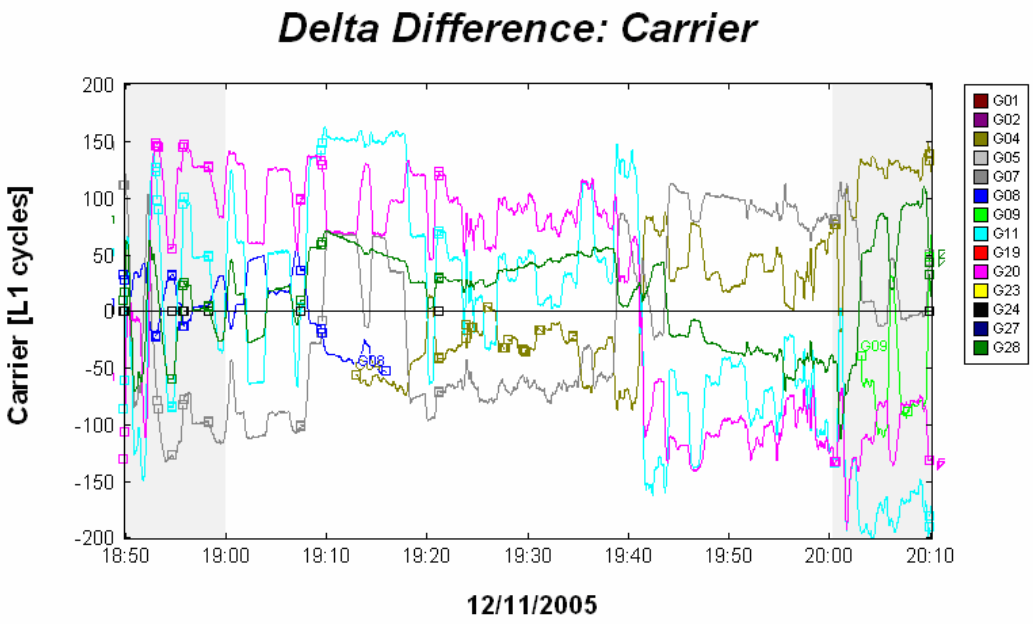

Figure 5.31: Between satellites single-differenced, time difference carrier-phase observations above 15° elevation angle observed by the Geodetic-quality GPS receiver (Trimbe 5700) on the moving vehicle.

Table 5.12 presents the statistics of the position difference between the point positioning solution and the reference solution for the selected 1-hour of Trimble data. The statistics from 1-hour data processing reflects more frequent resets to the code-only solution when compared with the static data processing. Total number of resets is 14. They are caused by cycle slips or complete loss of lock events. Decimetre-level east and height-component bias during this time interval is caused by unmodeled errors in the solution, of which the ionospheric grid model error and the omission of the solid Earth tides are the most significant ones. The solid Earth tidal correction can reach up to 30 cm in radial and 5 cm in horizontal direction [Kouba and Héroux, 2001]. It consists of latitude-dependent permanent displacement and periodic part with predominantly semidiurnal and diurnal periods and changing amplitudes. In the above solution the periodic part of the solid Earth tide does not average out and the permanent part still remains.

Position Error Components [cm]			
	North	**East**	**Height**
Mean	6. 8	-51.6	-46.1
Std. Dev.	35.0	17.5	44.6
r.m.s.	35.2	48.7	60.8
Measurement Residual r.m.s. [cm]			
Code	25.6	dPhase	0.8

Table 5.12: Position differences between the single-frequency point positioning solution (L1 + global ionospheric model) and the reference solution for Geodetic-quality GPS receiver (Trimbe 5700) 1-hour data from the kinematic test, $\sigma_P = 2.0\,\mathrm{m}; \sigma_\Phi = 0.10\,\mathrm{m}$.

The reference solution for the Garmin unit position was also obtained by the kinematic baseline solution with commercial GPS processing software with a static reference station at Lincoln Heights control monument. Problems in the TTC reference solution processing that were described in the Trimble data processing above occurred in the Garmin data processing as well. The difference between low-cost receiver and geodetic-quality data further complicated the situation. The difference in the data quality can be seen when Figure 5.31 and Figure 5.35 are compared. Note the difference in the y-axis scale when comparing the two figures. The position differences between the point positioning solution and the reference solution for the 1 hour of Garmin receiver data, corresponding with the selected period of Trimble data, are presented in Figure 5.33. Variations and spikes in the time series, caused by the residual outlier detection algorithm resetting the point positioning filter to code-only solutions, are more frequent and of higher magnitude when compared with Figure 5.28. This is due to the receiver hardware differences discussed in section 4.6, resulting in lower carrier-phase measurement quality in the case of the Garmin GPS 35 TracPak. The plot does not show the 15-metre peak-to peak variations in the up component differences, because of the y-axis scale that was chosen to be compatible on the two figures. Less frequent variations and spikes in the interval between 19.2 and 19.3 h compared to the interval between 19.4 and 19.7 hours are caused by cycle slips (shown on Figure 5.35) and loss of lock events (shown on Figure 5.32) on PRN 4. Note the similar difference can be seen on Figure 5.28. Pseudorange residuals in Figure 5.34 show larger variations and are about three times larger in size when compared with Figure 5.29. This is another consequence of the

receiver hardware differences discussed in section 4.6, resulting in lower pseudorange measurement quality in the case of the Garmin GPS 35 TracPak. Lower-quality carrier phase measurements also cause larger carrier-phase difference residuals in the bottom of Figure 5.34. Large spikes in carrier-phase difference residuals are due to larger cycle slips in the carrier-phase measurements when compared with Figure 5.29. The spikes in the bottom part of Figure 5.34 and the loss of lock and cycle slip events on Figure 5.32 coincide.

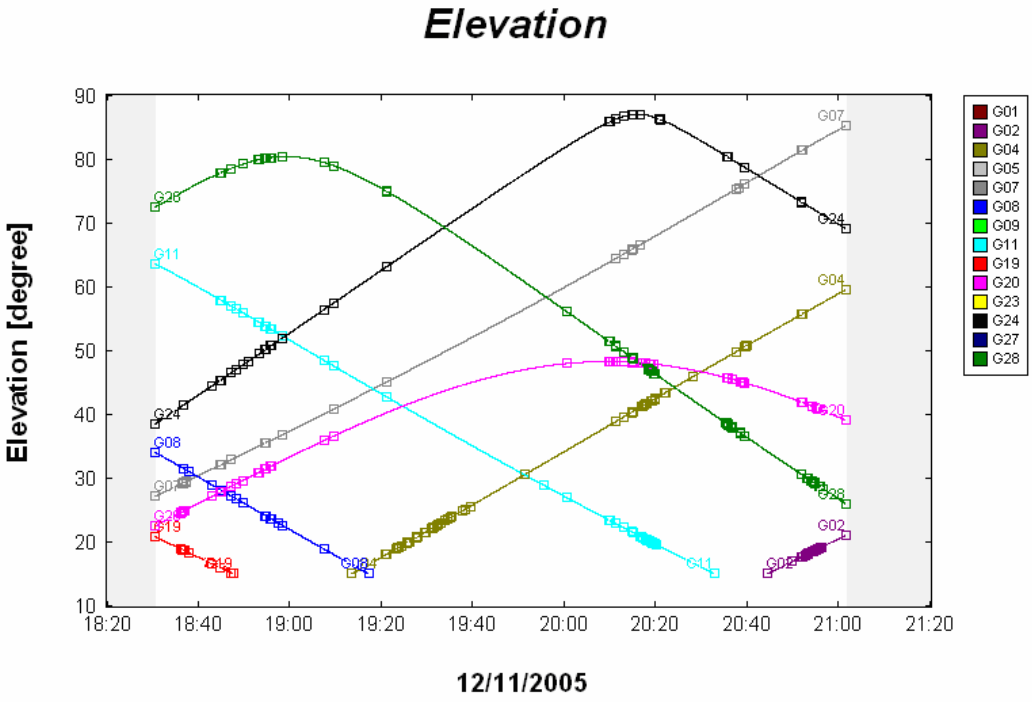

Figure 5.32: Elevation angles of satellites above 15° observed by the low-cost GPS receiver (Garmin GPS 35) on the moving vehicle. Squares indicate loss of lock events.

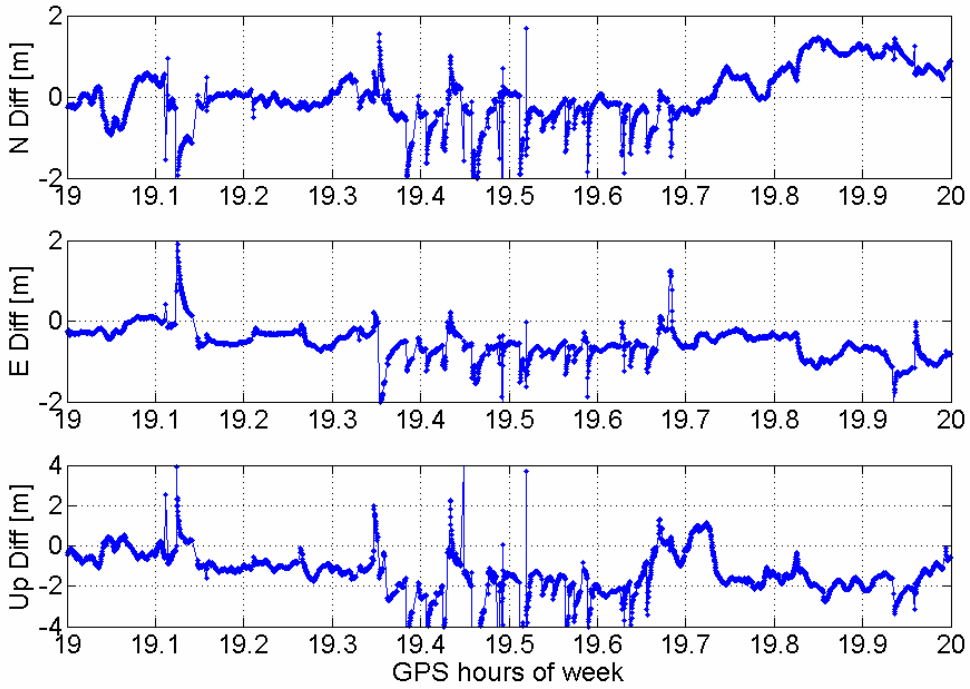

Figure 5.33: Position differences between the single-frequency point positioning solution (L1 + global ionospheric model) and the reference solution for the low-cost GPS receiver (Garmin GPS 35) receiver 1-hour data, $\sigma_P = 6.0$ m; $\sigma_\Phi = 0.10$ m.

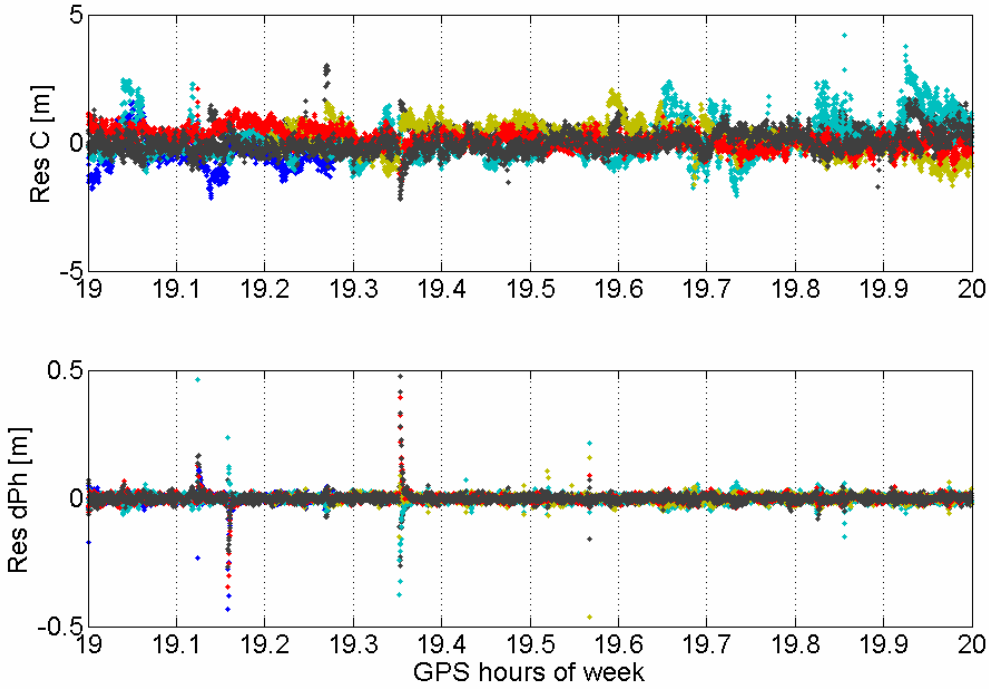

Figure 5.34: Filter residuals from the single-frequency point positioning solution (L1 + global ionospheric model) for the low-cost GPS receiver (Garmin GPS 35) 1-hour data, $\sigma_P = 6.0$ m; $\sigma_\Phi = 0.10$ m. Top: pseudoranges. Bottom: carrier-phase differences.

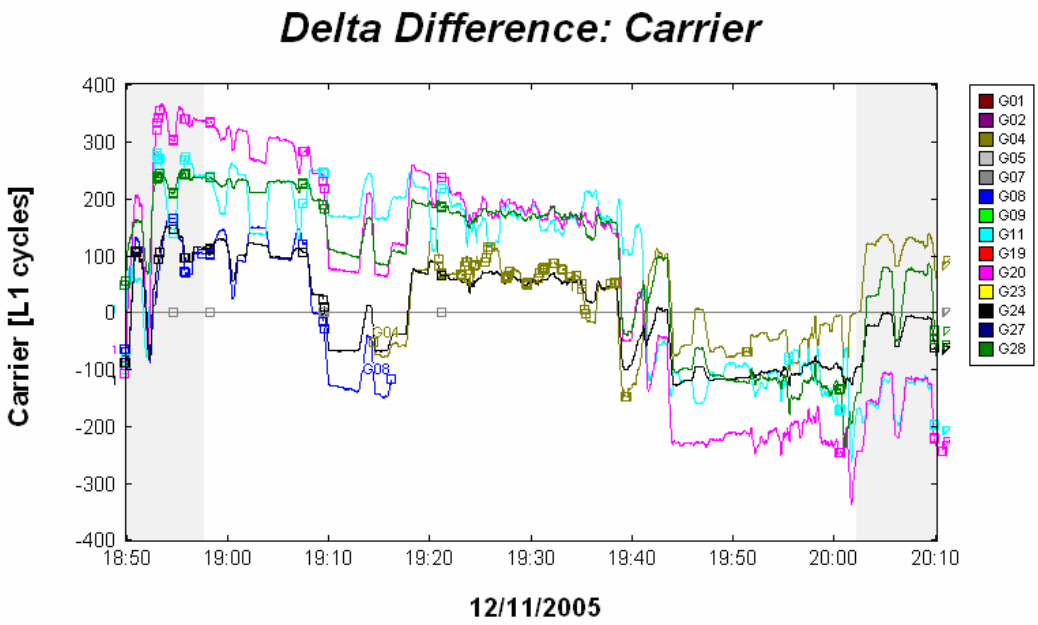

Figure 5.35: Between satellites single-differenced, time difference carrier-phase observations above 15° elevation angle observed by the low-cost GPS receiver (Garmin GPS 35) on the moving vehicle.

Table 5.13 shows the statistics of position component differences between the relative carrier-phase solution and the point-positioning solution for a 1-hour period of data. The statistics from 1-hour data processing reflects frequent resets to the code-only solution. Total number of resets is 28. Resets are caused by unrecognized cycle slips or complete loss of lock events. 60 cm east and 120 cm height component bias during this time interval is caused by unmodeled errors in the solution. Double in size height component bias when compared with the Trimble receiver results is caused by lower-quality pseudorange measurements. The difference in the data quality can be seen when Figure 5.31 and Figure 5.35 are compared. Note the difference in the y-axis scale when

comparing the two figures. The difference in data quality is also apparent from pseudorange and time-differenced carrier-phase residuals in Figure 5.34 which are about three times larger than those plotted in Figure 5.29. The spikes in the bottom part of the Figure 5.34 and the loss of lock and cycle slip events on Figure 5.35 coincide. Figure 5.35 shows between satellites single-differenced (PRN 7 is used as a reference satellite), time difference carrier-phase observations above 15 degrees elevation angle with the loss of lock indicators (square marks on the plot). This observable is showing cycle-slips (sudden shifts that are larger than 1 cycle) which can also trigger the residual outlier detection algorithm.

Position Error Components [cm]			
	North	East	Height
Mean	7.6	-60.0	-120.4
Std. Dev.	66.6	39.8	116.4
r.m.s.	66.8	67.0	158.5
Measurement Residual r.m.s. [cm]			
Code	61.3	dPhase	2.7

Table 5.13: Position differences between the single-frequency point positioning solution (L1 + global ionospheric model) and the reference solution for the low-cost GPS receiver (Garmin GPS 35) 1-hour data $\sigma_P = 6.0$ m; $\sigma_\Phi = 0.10$ m.

The 3D distances between the Garmin antenna and the Trimble antenna on the roof of the car is known to be 0.95 m. The 3D distance was also computed from the differences between the TTC double-differenced ambiguity-fixed kinematic baseline solution and the L1+GIM code and time-differenced carrier-phase point position solution. The error in the distance, which is mostly caused by the errors in the L1+GIM point position solution, is shown on

Figure 5.36. The statistics of the error are: mean = 1.85 m, standard deviation = 0.77 m

and r.m.s. = 1.95 m. The gaps in the solution around hour 19.4 and 19.5 are caused by the absence to the TTC ambiguity-fixed kinematic baseline solution most-likely cused by cycle-slips indicated in Figure 5.35. The gaps do not occur in Figure 5.28 because all TTC solutions, ambiguity-fixed and ambiguity-float solutions were used.

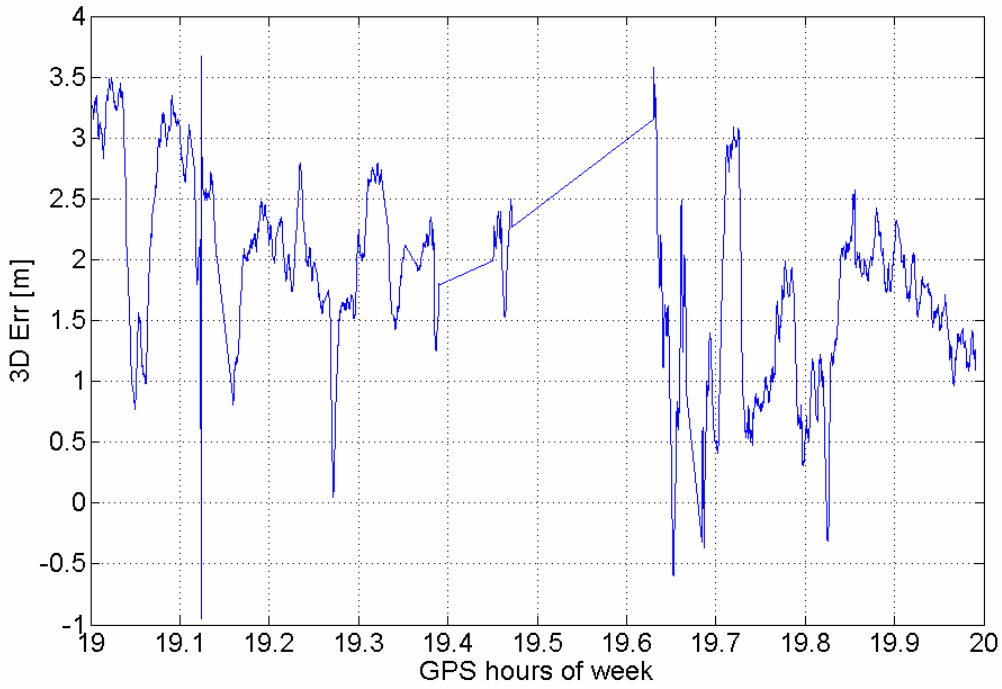

Figure 5.36: Error in 3D distance between the TTC double-differenced ambiguity fixed baseline solution and the L1+GIM code and time-differenced carrier-phase point position solution.

5.4 Spaceborne Data Testing

The purpose of these tests is to evaluate the performance of the filter on spaceborne datasets, which are unique in many aspects, e.g.: few-orders of magnitude higher platform velocities; smaller atmospheric error effects; unique GPS constellation geometry in the case of polar and near-polar orbits; and receiver hardware requirements, when

compared to the terrestrial GPS datasets. There are two LEO datasets which have been tested and are reported on in this section. The first dataset was collected by the GPS receiver on board of the Challenging Minisatellite Payload (CHAMP) satellite, and the second dataset was collected by a GPS receiver connected to a GPS signal simulator modelling GPS signals that will be collected onboard a future remote sensing satellite.

5.4.1 Spaceborne Geodetic Quality GPS Receiver

The purpose of this test is to compare the dual-frequency and single-frequency data with the reference solution. Due to the absence of an accurate ionospheric model for the upper portion of the Earth's ionosphere, the single frequency positioning results are expected to have significantly larger errors than the single frequency positioning results from a terrestrial GPS dataset.

The dataset used in the following tests was collected by the GPS receiver on board the CHAMP satellite. CHAMP is a German small satellite mission for geoscientific and atmospheric research and applications, managed by Germany's National Research Centre for Geosciences (GFZ) [GFZ, 2005]. The satellite orbits in a near-polar orbit with low altitude (inclination 87º, altitude at launch 454 km) and its main objectives are to collect high-precision gravity observations, magnetic field observations and radio occultation measurements over a five year period. The satellite orbital period is about 90 minutes. The CHAMP satellite is equipped with a JPL BlackJack dual-frequency spaceborne GPS

receiver and a choke ring GPS antenna for the satellite's precise orbit determination.

One hour of dual-frequency GPS data from January 5, 2002, was selected due to reference orbit information availability. The GFZ rapid science orbit (reduced dynamic orbits) was used as a reference; its 3D accuracy is better than 10 cm (1σ) when compared with satellite laser ranging results [Ritschel, 2006]. 10-second sampling rate data were first processed in ionosphere-free mode and then in the single frequency mode with the a-priori pseudorange and carrier-phase noise values were $\sigma_P = 2.0\,\mathrm{m}$, and $\sigma_\Phi = 0.10\,\mathrm{m}$ respectively.

The Cartesian component position differences between the ionosphere-free point positioning result and the GFZ orbit are plotted in Figure 5.37. The quasi-sinusoidal behaviour in Figure 5.37 is caused by the differences in the reference point in the GFZ solution (its reference is the satellite centre of mass) and the point positioning solution (its reference is the GPS antenna phase centre). The quasi-sinusoidal behaviour has a 1.5 hour period which corresponds with the CHAMP orbital period. The 3D distance between the satellite centre of mass and the GPS antenna reference point is about 1.54 m. The statistics of the distance calculated from the Cartesian coordinate differences are: mean = 1.52 m, standard deviation = 0.20 m and r.m.s. = 1.53 m. The resulting 3D distance computed from Cartesian coordinate differences reduced to the GPS antenna reference point is plotted in Figure 5.39. The spikes in the plot correspond with epochs where code-phase solution is not available, because of no redundancy to perform residual

outlier detection algorithm. These situations occur when the residual outlier detection algorithm fails to identify a problematic measurement caused by presence of cycle slips. From Figure 5.39 it can be seen that decimetre-level accurate solution can be accomplished if the ionospheric delay error is eliminated.

Figure 5.37 also shows outliers which are caused by the reset to the code-only position solution discussed in the previous paragraph. Note that the GPS hour 130 on Figure 5.37 corresponds with hour 10 on Figure 5.39. Even though some of these events are apparent in the position solution differences, most of them are more apparent in the time-differenced residual plot (bottom plot in Figure 5.38). The last 15 minutes in Figure 5.37 and in Figure 5.38 show divergence and large residual values, respectively due to the lack of data for the GPS satellite orbit interpolation. A statistical summary of the Cartesian component position differences between the ionosphere-free point positioning result and the GFZ orbit is in Table 5.14 in italics.

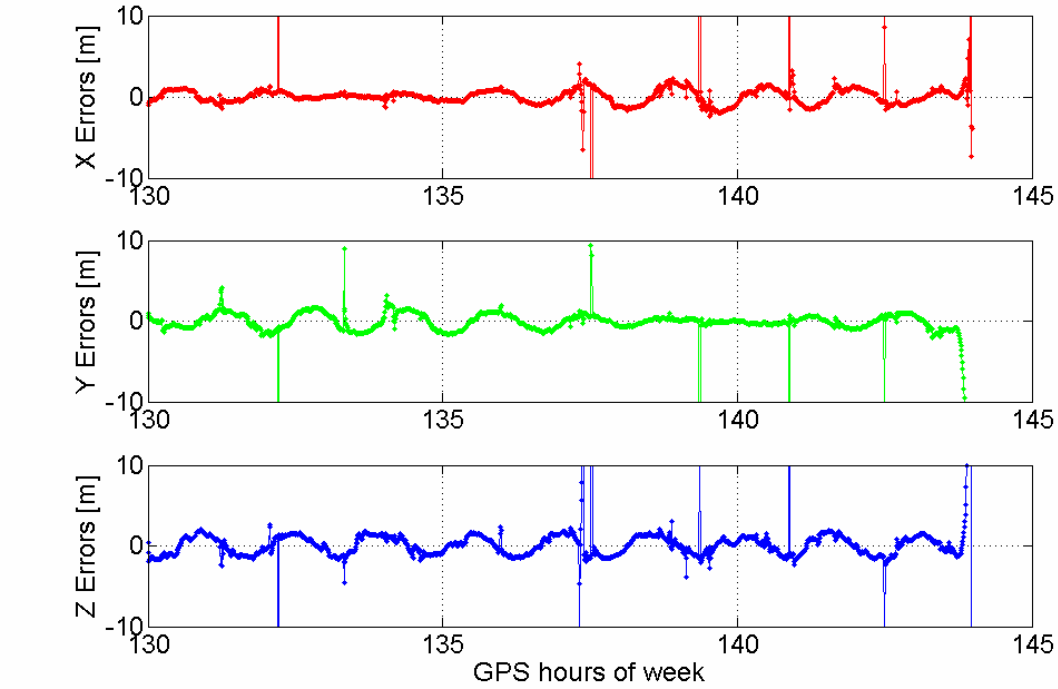

Figure 5.37: Position differences between the CHAMP ionosphere-free point positioning results and the reference trajectory on January 5, 2002.

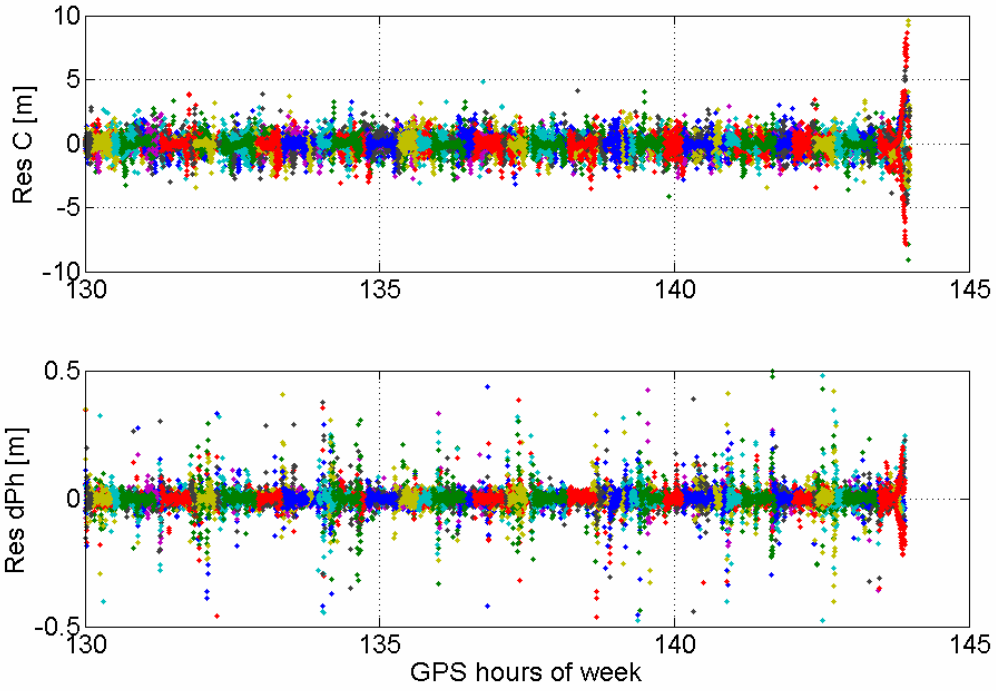

Figure 5.38: Filter residuals from the ionosphere-free point positioning solution for the CHAMP 1-hour data from January 5, 2002. Top: pseudoranges. Bottom: carrier-phase differences.

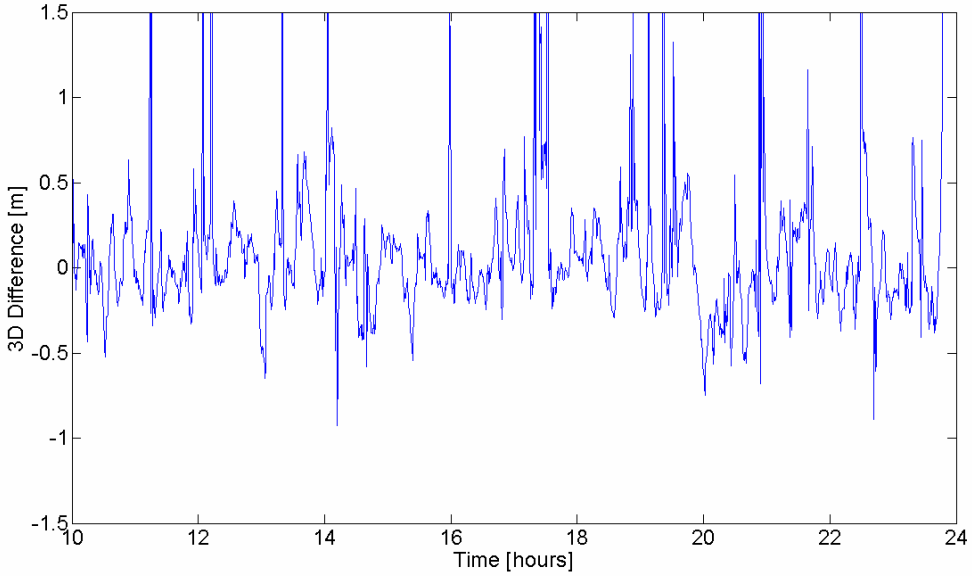

Figure 5.39: 3D distance w.r.t. GPS antenna reference point computed from Cartesian differences for CHAMP data.

The Cartesian component position differences between the single-frequency point positioning result and the GFZ orbit are plotted in Figure 5.40. Variations and discontinuities in Figure 5.40 are significantly larger than those in the ionosphere-free solution differences (Figure 5.37). The fact that the observed measurements are having difficulties to fit the mathematical model is also apparent in the plot of the least-squares adjustment residuals (Figure 5.41). This phenomenon is caused by the full impact of the ionospheric delay errors originating in the portion of the ionosphere, which is above the CHAMP satellite. The size of the ionospheric delay varies rapidly in size during CHAMP's orbit, e.g. during one orbit period of about 90 minutes, the satellite travels above the Earth's north and south polar regions, and the Earth's magnetic equator on day time-side and on the night time-side, which inherently causes at least five extremes in the ionospheric delay time series. A statistical summary of the Cartesian component position differences between the single-frequency point positioning result and the GFZ orbit for the initial 90-minute interval is in Table 5.14. The statistical summary is provided only for one orbit due to the difficulties of obtaining CHAMP reference solutions for all observation epochs for other orbits.

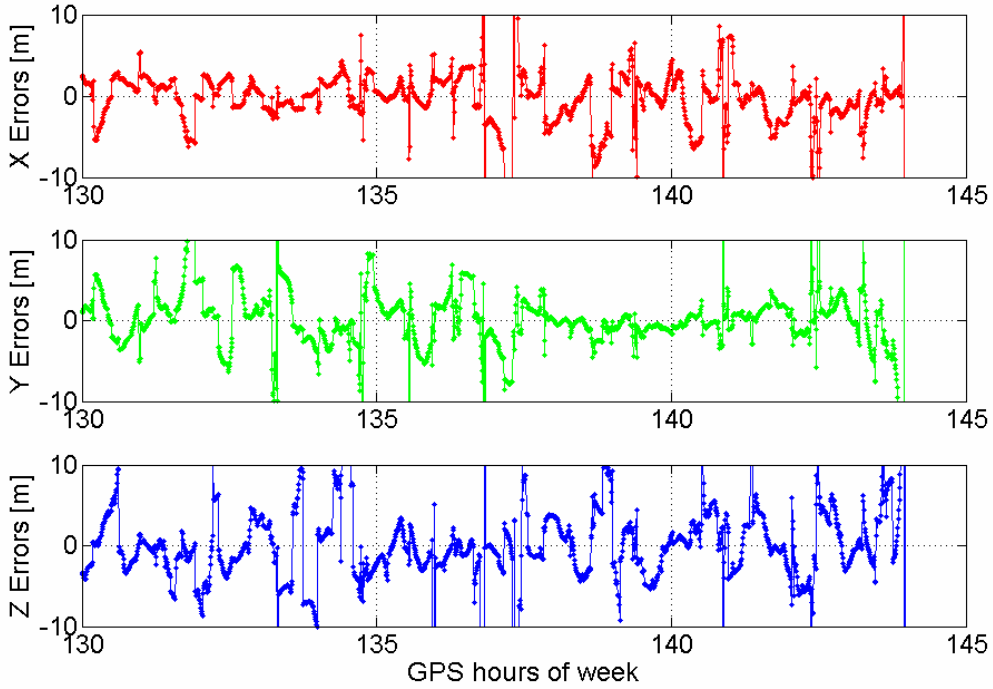

Figure 5.40: Position differences between the CHAMP single-frequency (L1-only) point positioning results and the reference trajectory on January 5, 2002.

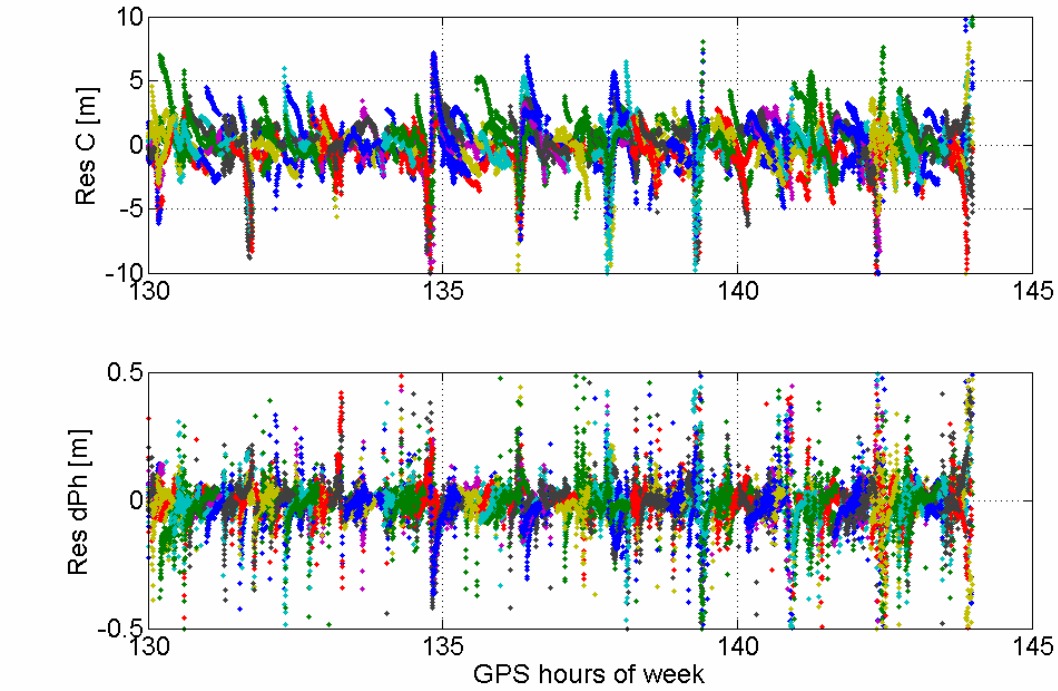

Figure 5.41: Filter residuals from the single-frequency (L1-only) point positioning solution for the CHAMP 1-hour data from January 5, 2002. Top: pseudoranges. Bottom: carrier-phase differences.

A direct comparison of the spaceborne point positioning results (Table 5.14) with the terrestrial point positioning results (Table 5.2 and Table 5.8) is not possible because of the differences in the reference points (i.e. antenna phase centre versus the centre of mass) and the differences in the coordinate reference frames. Ionosphere-free pseudorange and delta carrier-phase residuals (Figure 5.38 and Figure 5.3) and their r.m.s. values (Table 5.14 and Table 5.2) show the ability of the data to fit the mathematical model. Both code and time-differenced phase residual r.m.s. are compatible: 68.0 cm versus 53.2 cm for the ionosphere-free pseudorage residuals, respectively, and 3.0 cm and 3.7 cm for the ionosphere-free time-differenced phase residuals, respectively. This indicates that the mathematical model fits the static

terrestrial data as well as the kinematic spaceborne data. Close comparison of the time-differenced phase residuals (bottom part of Figure 5.38 and Figure 5.3) shows outliers in Figure 5.38 that are caused by the reset to the code-only position solution caused by outliers in the carrier-phase difference observation. Even though different filter settings were tested during the spaceborne data processing, the cause of the outliers in carrier-phase observations was not found.

Cartesian Error Components [cm]			
	X	**Y**	**Z**
Mean	75.4	47.1	2.6
	4.9	*-39.2*	*-2.3*
Std. Dev.	215.0	255.3	283.6
	67.2	*33.1*	*121.8*
r.m.s.	227.2	258.9	283.6
	67.2	*51.2*	*121.8*
Measurement Residual r.m.s. [cm]			
Code	169.2	dPhase	9.5
	53.2		*3.7*

Table 5.14: Cartesian component position differences between the single-frequency (L1-only) and ionosphere-free (*italics*) point positioning result and the GFZ orbit for the initial 180 epochs (1 orbit period).

5.4.2 Spaceborne Low-Cost Receiver

The purpose of this test is to evaluate the performance of a low-cost GPS receiver in the spaceborne environment. At the time of this test, real spaceborne data from such a receiver with a reliable reference solution was not available so simulated spaceborne GPS

data were used instead. The testing scenario was designed to provide a proper framework for GPS receiver performance testing in the context of the TerraSAR-X mission.

TerraSAR-X is a German radar satellite which was launched on June 15, 2007 [Infoterra GmbH, 2007] and the testing scenario describes a Sun-synchronous, dusk-dawn orbit with frozen perigee at 515 km altitude. The epoch was chosen as 30 May, 2006, 3:17 GPS Time (week 1377, 184620 s) and the GPS constellation model is based on the actual GPS almanac for week 1310, which is propagated to the scenario time within the signal simulator. The STR4760 simulator is configured to generate signals for all GPS satellites above the 5˚ obstruction angle measured from the Earth tangent [Montenbruck et al., 2005]. A little over 2 hours of data at 1 second sampling interval data were collected by the Phoenix single-frequency GPS receiver [Ardaens et al., 2007].

The Phoenix receiver includes the GP4050 chip from Zarlink capable of 12 channel tracking of L1 C/A code and L1 carrier-phase [Montenbruck et al. 2004]. Two manufacturers, Sigtec and NovAtel, employed the GP4050 chip in the commercial receiver boards (MG5001, Superstart II) for terrestrial mass market applications. The base of the Phoenix receiver is the commercial-off-the-shelf MG5001 OEM receiver from Sigtec, with specialized software designed for navigation of low Earth satellites and sounding rockets. The Phoenix receiver provides raw pseudorange, carrier-phase and Doppler measurements with noise levels of 0.3 m, 0.5 mm and 0.06 m/s at a carrier-to-noise ratio of 45 db-Hz [Montenbruck et al. 2004]. The pseudorange and carrier-phase noise level of the Phoenix receiver seems to be significantly lower than the Garmin GPS

25 receiver. It is not clear what noise values of the Garmin GPS 25 receiver [van Leeuven, 1998] correspond to the 45 db-Hz, but the pseudorange noise level seems to be two times lower and the carrier-phase noise level almost four times lower. The cost of the Garmin GPS 25 receiver is in the $100 range, and the Phoenix (MG5001) is in the $200 range.

The simulator generates a GPS signal strength compatible with the minimum signal-level conditions specified for the GPS. The average pseudorange noise r.m.s. is almost 1 metre, which is about twice as much as is experienced under good signal conditions using actual satellite signals. The application of ionospheric path delays (and a corresponding carrier-phase advance) is controlled by the simulator's Atmosphere File Editor. The "Spacecraft" ionosphere model and a constant total electron content (TEC) of 1 x 10^{17} electrons/m^2 were selected for the simulated scenario. The Klobuchar model coefficients for ionospheric refraction correction were available, but they were not in the solution used to provide ionospheric corrections for spaceborne single-frequency data. A-priori pseudorange and carrier-phase noise values were $\sigma_P = 2.0\,\mathrm{m}$, and $\sigma_\Phi = 0.10\,\mathrm{m}$ respectively. They are higher than the actual vales and purposely kept on the same level as in section 5.4.1.

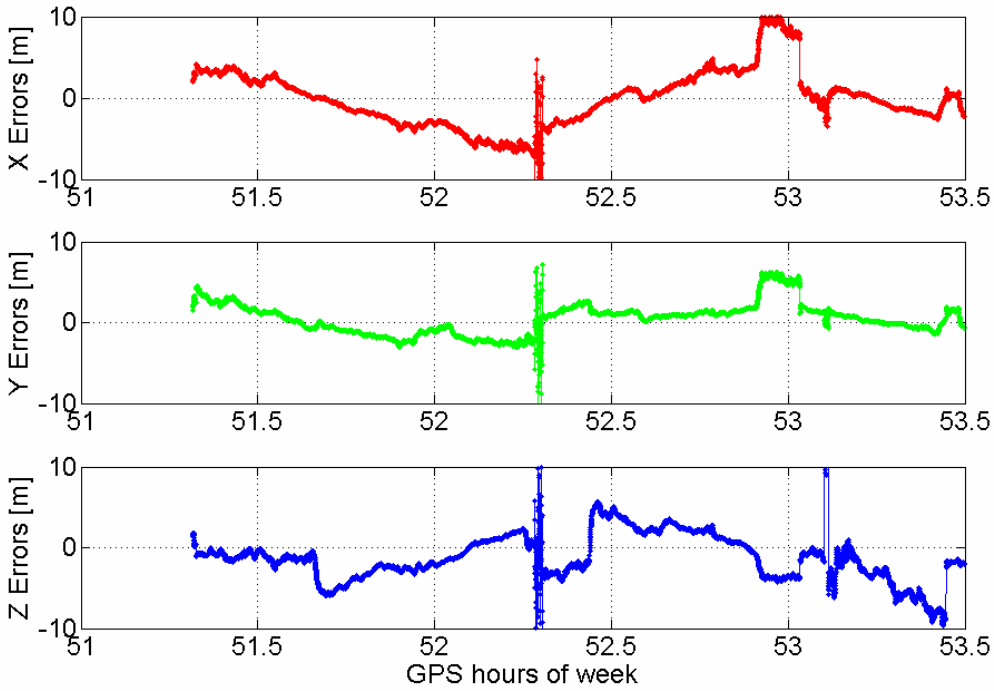

Figure 5.42: Position differences between the TerraSAR-X single-frequency (L1-only) point positioning results and the reference trajectory on May 30, 2006.

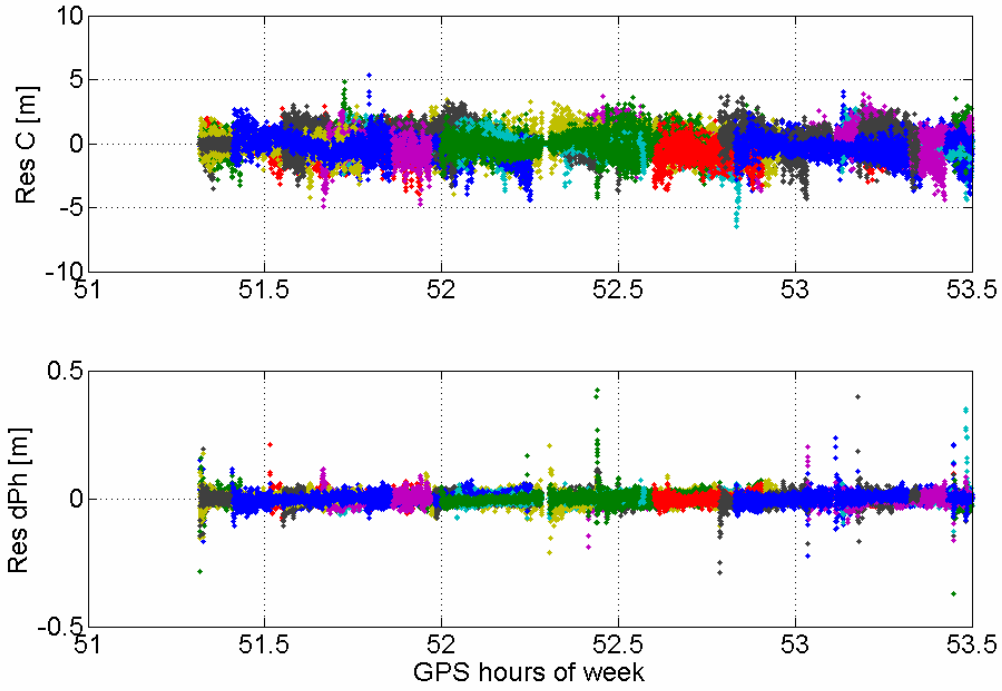

Figure 5.43: Filter residuals from the single-frequency (L1-only) point positioning solution for the TerraSAR-X data from May 30, 2006. Top: pseudoranges. Bottom: carrier-phase differences.

The Cartesian component differences between the point positioning solution and the simulated orbit for more than a two-hour period of time is plotted in Figure 5.42. The two-hour period covers only one orbit, because the orbital period of TerraSAR-X is 95 minutes. Position errors in Figure 5.42 are caused by ionospheric delay errors. Sudden metre-level discontinuities in Figure 5.42 are caused by the filter resets to the code-only solutions. The statistics of the differences between the point positioning solution and the simulated orbit are presented in Table 5.15. The standard deviations of the 2-hour solutions show metre-level standard deviations and about metre-level bias of the Cartesian component differences between the L1-only point position solution and the reference solution due to increased pseudorange and carrier-phase observation noise and

the ionospheric delay errors. Figure 5.43 shows the pseudorange and time-differenced carrier-phase residuals for the entire data period. There is about half of an hour period of time in the middle of the dataset when solutions were not available due to the presence of residual outliers. Solution statistics for a continuous code and time differenced phase solution for this period are presented in Table 5.15. in *italics*. Standard deviations of Cartesian component errors of the selected period of specific solution type are lower than the standard deviations of Cartesian component errors of the entire data series (combined solutions). Overall statistics for the two sets of results are compatible and they both reflect the need for ionospheric delay corrections.

Cartesian Error Components [cm]			
	X	**Y**	**Z**
Mean	9.6	48.1	-120.0
	-130.3	*-47.6*	*-151.7*
Std. Dev.	349.1	196.0	319.3
	317.1	*184.0*	*184.5*
r.m.s.	349.2	201.2	341.1
	342.7	*190.0*	*238.8*
Measurement Residual r.m.s. [cm]			
Code	90.1	dPhase	1.8
	86.3		*1.7*

Table 5.15 Cartesian component position differences between the single-frequency (L1-only) point positioning result and the reference orbit for the entire dataset and for the continuous code and delta-phase solution period (*italics*).

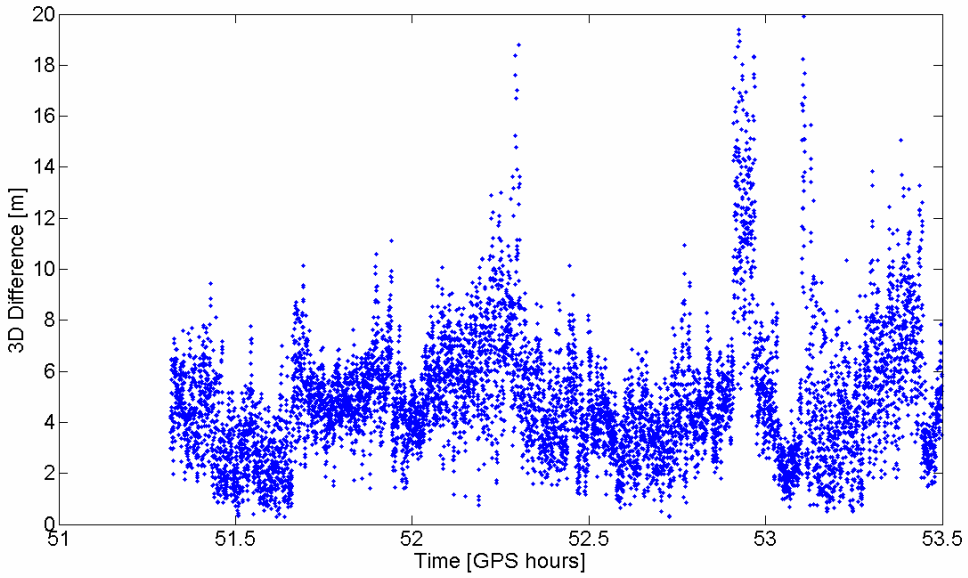

Figure 5.44: 3D distance w.r.t. GPS antenna reference point computed from Cartesian differences between code-only solution and the reference trajectory for Phoenix data.

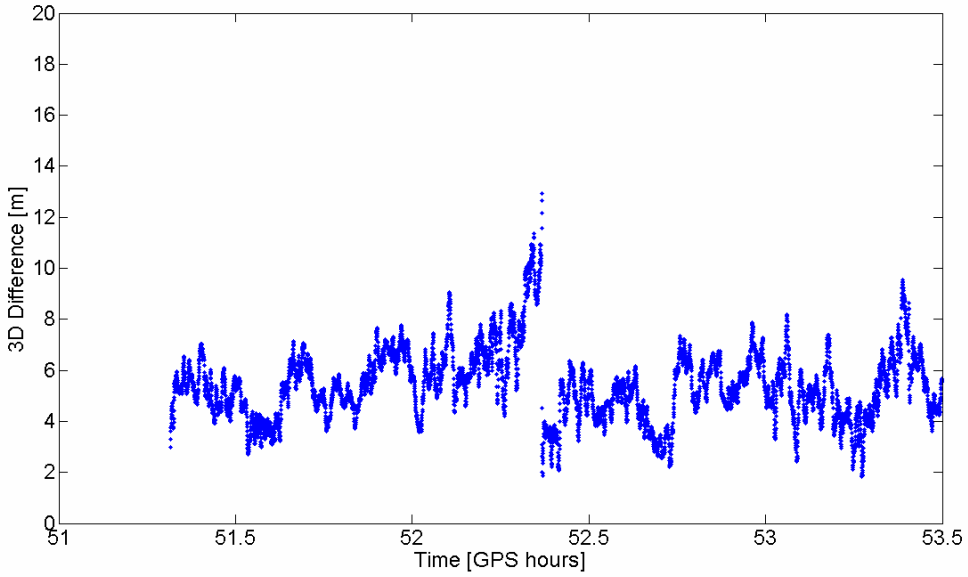

Figure 5.45: 3D distance w.r.t. GPS antenna reference point computed from Cartesian differences between code-phase solution and the reference trajectory for Phoenix data.

The 3D distance computed from Cartesian coordinate differences of code-only solution and the reference trajectory is plotted in Figure 5.44. The 3D distance computed from Cartesian coordinate differences of code-phase solution and the reference trajectory is plotted in Figure 5.45. From the comparison of Figure 5.44 and Figure 5.45 one can see that the code-phase solution is more precise, but it is of similar accuracy. This is verified by the statistics. The statistics of the distance calculated from the Cartesian coordinate differences of code-only solution are: mean = 4.9 m, standard deviation = 2.7 m and r.m.s. = 5.6 m. The statistics of the distance calculated from the Cartesian coordinate differences of code-phase solution are: mean = 5.0 m, standard deviation = 1.5 m and r.m.s. = 5.6 m. Major of the offset between the code-phase solution and the reference trajectory is caused by the ionospheric error. There are examples of a 3 metre-level systematic offset for a satellite orbiting at altitude of 650 km [Montenbruck et al. 2004].

The conclusion from spaceborne data testing with a geodetic-quality GPS receiver is that the point positioning technique is capable of delivering decimetre-level accurate results if the ionospheric delay error does not contaminate the solution. The single-frequency results obtained with geodetic-quality GPS receiver suffer from frequent resets to code-only solution. With the low-cost GPS receiver, single-frequency results, seem to be more continuous, but only represent one orbital period of simulated data. In any case the point positioning filter is still capable of providing a solution.

5.5 Algorithm Processing Capability

The point positioning software is capable of processing single and dual-frequency data from geodetic quality and low-cost receivers regardless of the platform dynamics. Single and dual-frequency data can be processed in code-only or in code and time-differenced carrier processing modes. The ionosphere-free linear combination is formed when dual-frequency data is available. The software takes care of C1-L1 biases and satellite hardware delays if the single frequency data is used.

High accuracy single-frequency processing requires input from the global ionospheric models. Global ionosphere maps, 2D grid map models, are used to generate zenith ionospheric delays at ionospheric pierce points. The zenith ionospheric delay values are converted to the slant delays using the ionospheric mapping function specified in the ionospheric data file. This procedure is completed inside the first version of the single-frequency point positioning software. A global ionospheric 3D model computes slant ionospheric delays on a server upon request when the specific single-frequency point positioning software version is run.

Data quality control is maintained by the residual outlier detection algorithm. The algorithm runs separately on code and carrier-phase data. An additional between-satellite time-difference carrier-phase algorithm could control the carrier-phase data to detect

cycle-slips, but this procedure works only for static data. The residual outlier detection algorithm is set to detect outliers with 95% confidence interval. The algorithm is especially important for low-cost GPS receiver data processing when receiver internal cycle-slip detection algorithms are not available. Software processing values such as observation type, the elevation angle cut-off angle, code and carrier-phase observation noise values etc. are specified in the processing configuration file. The point positioning software can deliver pseudorage and delta-carrier-phase solutions for low-cost receiver data for which a different state-of-art software package delivers code solution only.

Overall chapter 5 provided the summary of the geodetic quality, low-cost receiver, static, kinematic, terrestrial and spaceborne, single and dual-frequency data testing. Section 5.5 provided a summary of software processing capabilities. Comparison of the positioning results obtained on different datasets under different settings is provided in chapter 6.

6 Summary and Conclusions

The previous chapter described different tests that were performed to demonstrate the capabilities of the point positioning filter. This chapter will provide a summary of the results of all these tests and well as a description of the single-frequency point positioning research endeavour.

6.1 Data Testing Summary

The first sub-section in the previous chapter presented the results of different techniques of handling the ionospheric delay error in the single-frequency point positioning filter. The comparison of the positioning results obtained from fixed-site geodetic quality single-frequency measurements corrected by a global ionosphere grid map and dual frequency measurements using the ionosphere-free linear combination show decimetre-level agreement in terms of the mean errors with respect to the reference solution (Table 5.2). This example demonstrates the capability to use the global ionosphere grid map for the single-frequency data processing.

Comparison of the positioning results obtained from single-frequency measurements corrected by a global ionospheric grid map and by a global 3D ionospheric model also leads to decimetre-level disagreement of the r.m.s. errors with respect to the reference solution (Table 5.3). In this test the single-frequency measurements corrected by the

global 3D ionospheric model (Figure 5.4) have larger height component r.m.s. than the single-frequency measurements corrected by a global ionospheric grid map. The accuracy of the zenith ionospheric delay obtained from the final global ionosphere grid map model is between 2 and 9 TECU (1 TECU = 16 cm on L1) and the accuracy of the global 3D ionospheric model was not yet verified. Please note that this and the previous test were performed on datasets collected on ionospherically quiet days by a geodetic-quality GPS receiver on a CAGS station which is a few tens of kilometres away from the NRC1 station that is used to provide data for at least one of these models. Zenith ionospheric delay estimation described in the sub-section 5.1.3 was not successful. Besides the possibility of a software implementation error, a possible reason for the failure of the zenith ionospheric delay estimation is the mathematical correlation between the position height component estimates, receiver clock error estimates and the zenith ionospheric delay estimates.

During the filter performance evaluation, it was discovered that 30-second or 1-minute sampling intervals give optimal results in terms of the positioning differences (Table 5.5). The r.m.s. of the carrier-phase differences in the same table (Table 5.5) show that closer agreement between the measurements and the adjustment model is achieved with higher sampling rates. The convergence interval testing results in Table 5.6 and Table 5.7 demonstrate that a convergence period between 10 and 20 epochs is achievable regardless of the measurement sampling interval.

Test results from static geodetic-quality and low-cost GPS receivers on the Earth's

surface were presented in section 5.3.1 In order to minimize the influence of different atmospheric conditions, both static datasets were collected on the same day on stations about 10 km apart. A 30 second sampling interval was used by geodetic-quality and low-cost GPS receivers. Table 6.1 shows the r.m.s. of the position differences with respect to the reference solutions for the single-frequency positioning results. The horizontal error components for static data have about two to three-decimetre r.m.s. in the case of geodetic-quality GPS receiver and about eight-decimetre r.m.s in the case of low-cost GPS receiver. The r.m.s. of the vertical error components is about 6 decimetres and about 1.7 metres in both cases. More detailed statistics were given in Table 5.8 and Table 5.11. The most significant difference between the geodetic-quality and low-cost GPS receivers is in the standard deviation, the precision, of horizontal and vertical components. This is caused by the hardware differences explained in section 4.6. The difference in the GPS equipment causes the difference in quality of the GPS observations and subsequently the difference in the positioning results. The static geodetic-quality GPS receivers are nearly twice as accurate than the low-cost GPS receivers in horizontal components and almost three-times more accurate in the vertical component.

Position Error Components [cm]			
Data Type	**North r.m.s.**	**East r.m.s.**	**Height r.m.s.**
Geodetic-quality	27.3	15.5	63.9
Low-cost	76.3	76.4	167.4

Table 6.1: Position errors in static single-frequency data from geodetic-quality and low-cost GPS receivers.

Table 6.2 shows the r.m.s. of the position differences with respect to the reference solutions for the single-frequency positioning results. More detailed statistics can be found in Table 5.12 and Table 5.13. Similar to the static results, the kinematic geodetic-quality GPS receivers are nearly twice as accurate as the low-cost GPS receivers in horizontal components and almost three-times more accurate in vertical component due to differences in the quality of the observations, which are explained in the previous paragraph. Further comparisons between the static and kinematic results should not be made because the conditions are very different. There is a significant difference in: the amount of data collected, 24 hours versus 1 hour; the data sampling interval 30 s versus 1 second; and the atmospheric conditions, datasets were collected on different days. It is also expected that there should be a difference in terms of quality between the static and kinematic results; kinematic results are expected to be less accurate than the static results. There is a small difference in precision of the geodetic quality results (Table 5.8 and Table 5.12), but overall the difference between the static and kinematic results is not clearly indicated by the results in Table 6.1 and Table 6.2. For this reason more kinematic data testing is recommended.

Position Error Components [cm]			
Data Type	**North r.m.s.**	**East r.m.s.**	**Height r.m.s.**
Geodetic-quality	35.2	48.7	60.8
Low-cost	66.8	67.0	158.5

Table 6.2: Position errors in kinematic single-frequency data from geodetic-quality and low-cost GPS receivers.

Spaceborne GPS results in terms of the 3D error statistics are summarized in Table 6.3. The reason for a 3D error comparison is to remove the effect of the satellite centre of mass – GPS antenna phase center offset in the case of geodetic-quality receiver data. Direct comparison between the results from the geodetic-quality GPS receiver and in the low-cost GPS receiver is not recommended because of the following reasons: First, the geodetic quality data are real while the low-cost receiver data are simulated. Second, the geodetic data results were obtained using the ionosphere-free linear combination while in the low-cost data the effects of the simulated ionospheric delay were ignored. Third, the data sampling rate and the amount of data is different. Geodetic-quality data has 10 s sampling rate and almost 14 hours of data is available while the low-cost data has 1 s sampling rate and less than 2.5 hours of data is available. A limited comparison between the geodetic-quality terrestrial (Table 5.8) and geodetic-quality spaceborne data (Table 6.3) could be made because both sets of results were obtained using the ionosphere-free linear combination. This comparison is limited, because the error components in the two tables are different. The geodetic-quality spaceborne results seem to be better than the terrestrial results because of the terrestrial point positioning specific effects that are not included in the functional model (e.g. residual tropospheric delay, Earth tides and ocean tide loading). These effects are discussed in section 4.2.

GPS Receiver Type	3D Error [cm] Mean	Std.Dev.	r.m.s.
Geodetic-quality (IF)	-1.8	20	20.1
Low-cost (L1)	496	149	555

Table 6.3: 3D errors in geodetic-quality (ionosphere-free) and low-cost (single-frequency) spaceborne GPS data.

6.2 Point Positioning Research Summary

The point positioning algorithm development started with a question if it is possible to use low-cost GPS receivers for high-accuracy GPS point positioning and with the goal to investigate the positioning capabilities of low-cost GPS receivers. There were three receivers tested during this research. In order to reach the goal, a software processing the original GPS observations had to be implemented. Leading-edge software in terms of accuracy and low-cost data processing capability was developed. To the author's knowledge the software described in this dissertation is the only software capable of reliably processing pseudorange and carrier-phase data from low-cost GPS receivers.

The impact of different ionospheric delay models on the point positioning results was

investigated because of the focus of this dissertation on low-cost GPS receivers Ionospheric delay models include the Klobuchar, or the broadcast ionospheric delay model, 2D global ionospheric grid model, and 3D global ionosphere model. The 3D global ionosphere model was tested as part of the high-accuracy point positioning algorithm for the first time. The ionospheric model was tested on geodetic-quality receiver datasets and it shows potential to be used with low-cost receivers. There was only day with few-hour day available data for the 3D global ionosphere model. The station data were tested and one of the stations was used for 2D model testing on different dates for compatibility purposes. It was also found that 2D ionospheric models are sufficient for low-cost-receiver static positioning with few decimetre-level height component r.m.s.

Selection of a point positioning software solution started with one epoch code-only position solution. In the next step, the solution is carried from one epoch to the next by the sequential least-squares estimation. If the process which generated the current epoch solution from the previous epoch solution (system dynamics) is known, it is possible to replace the sequential least-squares estimation with the Kalman filter. Suitable Kalman filter models were investigated in Beran et al. [2003]. The system dynamics implemented in the Kalman filter reduces the number of suitable GPS applications. In order to keep the point positioning filter more general, it was decided to use the time differenced carrier-phase measurements. The time differenced carrier-phase measurements relate one epoch to the next and provide the system (platform) dynamic information to the filter.

A common application requirement is to keep the user intervention to a minimum. This is usually accomplished though automated data quality control. Independent data quality controls on the pseudorange measurements and on the time-differenced carrier-phase measurements have been implemented in the software. The algorithms are based on the residual outlier detection theory. It was confirmed that the algorithm is capable of detecting 95% of pseudorange and carrier-phase outliers while the filter maintains maximum use of carrier-phase measurements. The quality control algorithm also rejects all results where statistical testing was not available due to lack of redundancy. This provides a high degree of confidence in the results which is critical for low-cost applications.

There are several limitations in the single-frequency point positioning software. Point positioning tests show that kinematic datasets with short periods of continuous carrier-phase observations are more difficult to handle than static datasets with continuous carrier-phase tracking. A highway drive with frequent passes under bridges created a worst case scenario for GPS signal tracking. It is possible that these outages can be overcome with a low-cost inertial measurement unit (IMU), because the drift over a few-second periods of time would not be significant. Fewer multipath induced problems were found in the kinematic datasets than in the static datasets. It was also found that pseudorange multipath creates a limitation in precision and accuracy of the positioning results in static datasets. The majority of the results presented in this dissertation are terrestrial, because the spaceborne applications are far more challenging than the terrestrial. Spaceborne single-frequency point positioning results are worse than the

terrestrial results, because of absence of the ionospheric modeling.

The overall state of the art of precise point positioning indicated in the literature search shows 5 to 10 cm-level horizontal precision and 30 to 60 cm vertical precision, and 15 to 20 cm horizontal accuracy and 50 to 90 cm vertical accuracy for the static and kinematic single-frequency point positioning. Lower boundaries apply to static applications and upper boundaries apply to kinematic applications (see section 2.2 for more information). The precision of the results is represented by a standard deviation and the accuracy is represented by values at 95% probability level. These results were accomplished with geodetic-quality GPS receivers and the terrestrial results presented in this dissertation are compatible with the leading edge results. The research presented advanced the state of the art in the area of low-cost point positioning, with the ability of the software to process data from a variety of platforms with a high degree of confidence.

This section summarized the over-arching research endeavour, listed the contributions to the leading edge research in the field of high precision GPS point positioning and provided limitations of the low-cost positioning technique. The following chapter provides ideas that may overcome some of the problems found during the research on the single frequency point positioning technique.

7 Future Research

This chapter has three sections on the future recommendations for the algorithm, software development and testing data collection. The paragraphs in each section are organized in the order of importance from highly recommended topics to topics to be considered as possible avenues for future research.. Section 7.1 provides recommendations for future work on the point positioning algorithm such as cycle slip handling, pseudorange multipath mitigation and residual ionospheric delay estimation. The last paragraph in this section indicates future work areas in the single-frequency spaceborne point positioning. Section 7.2 gives suggestions for future data collection and further software development. The last section in this chapter gives the reader an idea about the evolution in the Global Positioning System and the future of the single-frequency point positioning technique.

7.1 Point Positioning Algorithm Recommendations

The cycle slip detection algorithm works for static applications. In a kinematic scenario, measurements to different satellites experience different accelerations and the algorithm fails. The present solution is to leave the cycle slip corrupted measurements to be detected by the residual outlier detection algorithm, which depends on the

measurement noise values of a particular receiver. An alternative method, which works regardless of the platform dynamics, is the use of the code minus phase observable for the cycle slip detection. A major problem with this observable is the pseudorange noise, and consequently the technique fails to detect cycle slips with a size of up to a few cycles.

Pseudorange multipath seems to cause a problem on some static sites with above average multipath. Since the receiver tracking loop improvement or multipath-mitigating antennas are not an option, the technique will still have to rely on a multipath de-weighting function. An exponential elevation-angle weighting function requires one additional run of the filter, so an alternative method could use the signal-to-noise ratio measurements for the stochastic modelling. It would have to be verified that the low-cost GPS receiver actually includes the signal-to-noise measurement in the binary data stream and the binary to RINEX [Gurtner, 2002] converter would have to be modified to output these measurements as additional observations.

Once the errors from atmospheric delays are completely removed, it will be desirable to incorporate missing point positioning corrections for terrestrial applications to the functional model. A software implementation of these corrections would not be overly difficult due to the C++ class structure and the software design. Additional terrestrial point positioning considerations include: solid Earth tides and ocean tide loading, satellite phase wind-up and sub-diurnal variations in Earth rotation. Depending on the time of observation and the geographical location, the expected size of the up component bias is on a decimetre level.

Spaceborne point positioning requires more sophisticated ionospheric error modelling. Previous research described by Montenbruck and Gill [2001] shows that scaling Earth surface TEC values according to a vertical ionospheric profile does not provide decimetre-level accuracy. A 3D global ionosphere model for spaceborne GPS applications qualifies as a more sophisticated model, but there are no results available in this dissertation because the model was geared toward the real-time applications and did not store data for post processing. Spaceborne datasets which are kinematic by default are subject to the same data quality control issues as the terrestrial kinematic datasets. Further assessment would require a consistent reference point for GPS observations and the reference trajectory which was not available. The main limitation for the spaceborne single-frequency GPS positioning is the quality of the ionospheric error model.

7.2 Data Collection and Software Development Recommendations

It is recommended to use a low-cost receiver with an external antenna. This would allow splitting the GPS signal into two receivers for kinematic testing and determine a reference solution with a geodetic-quality GPS receiver. It would also allow connecting the low-cost receiver to the GPS signal simulator and comparing the results with the reference trajectory in different testing scenarios (including terrestrial, airborne and spaceborne GPS scenarios) or for performing zero-baseline tests to assess the low-cost

receiver performance.

A number of improvements could be made to the processing software. It is recommended to continue the software development process, because there is always a potential to make the algorithm more efficient and make it run with less user interaction. The point positioning software is run in the integrated development environment and it has to be compiled every time the processing parameters are changed. Once the results are generated in the form of multiple text files, additional Matlab scripts are run to generate plots and statistics for further analysis. It will be beneficial to isolate the processing parameters in a separate text file and compile or link the Matlab plotting scripts directly to the main executable.

Real-time implementation of the point-positioning software developed at UNB would be relatively simple. Once the interface with the real-time orbit, clock and ionospheric corrections is built, the software will be ready for real-time processing. The software currently does not include any pre-processing or backward smoothing. The exponential elevation angle weighting, which requires the residuals, is not essential.

7.3 Future Concerns in Single-Frequency Point Positioning

In the Proceedings of the IEEE “Special issue on global positioning system” P. Misra and P. Enge wrote “Global positioning system (GPS) is the most important gift of the Department of Defense to the civil world, perhaps with the exception of the Internet. Civil applications unforeseen by developers of the system are thriving and many more are on the way. Commerce in GPS equipment and services continues to grow rapidly and this success has created expectations and demands that the system was not designed to meet.” [Misra and Enge, 1999]. It is natural that just like any successful technological invention GPS is still evolving. Some expect that GPS navigation could become the next "breakout" cell phone feature.

The sixth modernized GPS Block IIR-M satellite broadcasting the second civil signal (L2C) was launched from Cape Canaveral Air Force Station on March 15, 2008. The U.S. Air Force is expected to launch the remaining two GPS IIR-M satellites in 2008. The next GPS IIR-M launch is anticipated for June 2008 from Cape Canaveral Air Force Station. Even though the U.S. Air Force does not guarantee the availability or quality of the L2C signal until Initial Operational Capability (IOC), the newest GPS receivers from all major commercial manufacturers are now capable of receiving the L2C signals. It is likely that single-frequncy receivers will continue to be produced due to lower price and better power utilization [Khattanov et al., 2004]. The determing factor would be the price of dual-frequency receivers versus the cost of auxilary data transmission, such as the ionosperic delay predictions, on the cellular network.

Initial research in spaceborne single-frequency point positinning was conducted by Montenbruck and Gill [2001] and others. In this dissertation it has been established that it is possible to process the data from low-cost spaceborne receivers with the minimum signal-level conditions specified for the GPS. This is useful information for researchers in the space industry resolving engineering challenges such as power consumption and financial challenges due to budget restrictions. There is definitely a future for single-frequency spaceborn positioning.

8 References

Ardaens J.S., S. D'Amico, B. Kazeminejad, O. Montenbruck, and E. Gill (2007). "Spaceborne Autonomous And Ground Based Relative Orbit Control for the TerraSAR-X/Tandem-X Formation." Proceedings of the 20th International Symposium on Space Flight Dynamics; 24-28 Sep. 2007, Annapolis, Maryland U.S.A., pp. 1-13.

Axelrad, P. and R.G. Brown (1996). "GPS Navigation Algorithms." in *Global Positioning System: Theory and Applications Volume 1*, Eds. B.W. Parkinson, J.J. Spilker Jr., Progress in Astronautics and Aeronatics Volume 164, American Institute of Aeronatics and Astronautics, Inc., Washington, D.C., U.S.A., pp. 409-433.

Bae T., D. Grejner-Brzezinska, and J.H. Kwon (2007). "Efficient LEO Dynamic Orbit Determination with Triple Differenced GPS Carrier Phases." Journal of Navigation, Vol. 60, May 2007, Cambridge University Press, pp. 217-232.

Beran, T., D. Kim, and R.B. Langley (2003). "High-Precision Single-Frequency GPS Point Positioning." Proceedings of the 16th International Technical Meeting of the Satellite Division of The Institute of Navigation, Portland, Oregon, U.S.A., 9-12 September 2003; The Institute of Navigation, Alexandria, Virginia, U.S.A., pp. 1192-1200.

Beran, T., S.B. Bisnath, and R.B. Langley (2004). "Evaluation of High-Precision Single-Frequency GPS Point Positioning Models." Proceedings of the 17th International Technical Meeting of the Satellite Division of The Institute of Navigation, Long Beach, California, U.S.A., 21-24 September 2004; The Institute of Navigation, Alexandria, Virginia, U.S.A., pp. 1892-1901.

Beran, T., R.B. Langley, S.B. Bisnath, and L. Serrano (2005). "High-Accuracy Point Positioning with Low-Cost GPS: How Good Can It Get." Proceedings of the 18th International Technical Meeting of the Satellite Division of The Institute of Navigation, Long Beach, California, U.S.A., 13-16 September 2005; The Institute of Navigation, Alexandria, Virginia, U.S.A., pp. 1524-1534.

Bisnath, S.B. and R.B. Langley (1999). "Precise a Posteriori Geometric Tracking of Low Earth Orbiters with GPS." *Canadian Aeronautics and Space Journal,* Vol. 45, pp. 245-252.

Bisnath, S.B., D. Kim, and R. B. Langley (2001). "A New Approach to an Old Problem: Carrier-Phase Cycle Slips". *GPS World*, May, Vol. 12, No. 5, pp. 46-51.

Bisnath, S.B. and R.B. Langley (2002). "High-Precision, Kinematic Positioning with a Single GPS Receiver." *Navigation: Journal of the Institute of Navigation*, Vol. 49, No. 3, Fall 2002; The Institute of Navigation, Alexandria, Virginia, U.S.A., pp. 161-169.

Bisnath S.B., D. Wells, and D. Dodd (2003). "Evaluation of Commercial Carrier-Phase-Based WADGPS Services for Marine Applications." Proceedings of the 16th International Technical Meeting of the Satellite Division of The Institute of Navigation, Portland, Oregon, U.S.A., 9-12 September, 2003, The Institute of Navigation, Alexandria, Virginia, U.S.A., pp. 17-27.

Bisnath, S.B. (2004). *Precise Orbit Determination of Low Earth Orbiters with a Single GPS Receiver-Based, Geometric Strategy.* Ph.D. Dissertation, Department of Geodesy and Geomatics Engineering Technical Report No. 220, University of New Brunswick, Canada, 143 pp.

Bona, P. and Ch. Tiberius (2001). "An Experimental Comparison of Noise Characteristics of Seven High-End Dual Frequency GPS Receiver Sets." Series on Mathematical Geodesy and Positioning of Delft University of Technology, 2001, No. 22, pp. 154-161.

Borre, K. and G. Strang (1997). "Autocorrelation Functions in GPS Data Processing: Modeling Aspects." Proceedings of the 10th International Technical Meeting of the Satellite Division of The Institute of Navigation, Kansas City, Missoury, U.S.A., 16-19 September 1997; The Institute of Navigation, Alexandria, Virginia, U.S.A., pp. 1143-1150.

Brown, R.G. and P.Y.C. Hwang (1992). *Introduction to Random Signals and Applied Optimal Estimation.* 2nd ed., Willey, New York 1992, 502 pp.

Castleden, N., G.R. Hu, D.A. Abbey, D. Weihing, O. Øvstedal, C.J. Earls, and W.E. Featherstone (2005). "First results from Virtual Reference Station (VRS) and Precise Point Positioning (PPP) GPS Research at the Western Australian Centre for Geodesy." Journal of Global Positioning Systems, Vol. 3., No. 1-2; Journal of the International Association of Chinese Professionals in Global Positioning Systems, pp. 79-84.

Center for Orbit Determination in Europe (CODE) (2006). "Global Ionosphere Maps Produced by CODE" [On-line] 26 January, 2006.
http://www.aiub.unibe.ch/ionosphere.html

Chen, K. and Y. Gao (2005). "Real-Time Precise Point Positioning Using Single Frequency Data." Proceedings of the 18th International Technical Meeting of the Satellite Division of The Institute of Navigation, Long Beach, California, U.S.A., 13-16 September 2005; The Institute of Navigation, Alexandria, Virginia, U.S.A., pp. 1514-1523.

Collins, J.P. (1999). *Assessment and Development of the Tropospheric Delay Model for Aircraft Users of the Global Positioning System.* M.Sc.E. Thesis, Department of Geodesy and Geomatics Engineering Technical Report No. 203, University of New Brunswick, Canada, 174 pp.

European Space Operations Centre (ESOC) (2003). "IGS LEO JASON-1 Orbit Campaign 2003." [On-Line] January 16, 2003. http://nng.esoc.esa.de/gps/J1_campaign.html

FusionNumerics (2005). "GPS Corrections & Ionospheric Forecasting Portal" [On-line] April 7, 2005. http://gpscorrections.com/

Gao, Y., Y. Zhang and K. Chen (2006). "Development of a Real-Time Single-Frequency Precise Point Positioning System and Test Results." Proceedings of the 19th International Technical Meeting of the Satellite Division of The Institute of Navigation, Fort Worth, Texas, U.S.A., 26-29 September 2006; The Institute of Navigation, Alexandria, Virginia, U.S.A., pp. 2297-2303.

Gelb, A. (Ed.) (1974). *Applied Optimal Estimation.* The MIT Press, Massachusetts Institute of Technology, Cambridge, 374 pp.

GeoForschungsZentrum (GFZ) (2005). "Challenging Minisatellite Payload for Geophysical Research and Applications (CHAMP), The CHAMP Misssion." [On-Line] 29 November, 2005. http://www.gfz-potsdam.de/pb1/op/champ/index_CHAMP.html

GeoForschungsZentrum (GFZ) (2006). "Challenging Minisatellite Payload (CHAMP) Information System and Data Center (ISDC)." [On-Line] 26 January, 2006. http://isdc.gfz-potsdam.de/champ/

Goad, C.C. (1990). "Optimal Filtering of Pseudorages and Phases from Single-Frequency GPS Receivers." Navigation: Journal of the Institute of Navigation, Vol. 37, No. 3, Fall 1990; The Institute of Navigation, Alexandria, Virginia, U.S.A., pp. 249-262.

Gold, K., W.I. Bertiger, S.C. Wu, and T.P. Yunck (1994). "GPS Orbit Determination for the Extreme Ultraviolet Explorer." Navigation: Journal of the Institute of Navigation, Vol. 41, No. 3, Fall 1994; The Institute of Navigation, Alexandria, Virginia, U.S.A., pp. 337-351.

Gurtner, W. (2002). "RINEX: The Receiver Independent Exchange Format Version 2.10." Astronomical Institute of University of Berne. [On-Line] 25 January 2002. http://igscb.jpl.nasa.gov/igscb/data/format/rinex210.txt

Haines, B., W. Bertiger, S. Desai, D. Kuang, T. Munson, L. Young, and P. Willis (2003). "Initial Orbit Determination Results for JASON-1: Towards a 1-cm Orbit." Navigation: Journal of the Institute of Navigation, Vol. 50, No. 3, Fall 2003; The Institute of Navigation, Alexandria, Virginia, U.S.A., pp. 171-180.

Hatch, R. (1982). "The Synergism of GPS Code and Carrier Measurements." Proceedings of the Third International Geodetic Symposium on Satellite Doppler Positioning, Las Cruces, New Mexico, U.S.A., 8-12 February 1982, Vol. II, pp. 1213-1232.

Hill, C. J., T. Moore, M. Dumville (1999). "GRINGO A RINEX logger for hand-held GPS receivers." Proceedings of the 12th International Technical Meeting of the Satellite Division of the Institute of Navigation, Nashville, Tennessee, U.S.A., 14-17 September 1999; The Institute of Navigation, Alexandria, Virginia, U.S.A., pp. 1647 - 1652.

Hofmann-Wellenhof, B., H. Lichtenegger, and J. Collins (2001). *Global Positioning System: Theory and Practice.* (5th edition) Springer-Verlag, New York, 382 pp.

IS-GPS-200D (2004). Navstar GPS Space Segment/Navigation User Interface Control Document. ARINC Research Corporation, El Segundo, California, U.S.A., 138 pp.

Infoterra GmbH (2007). "Infoterra GmbH TerraSAR-X Exploitation Website." [On-Line] 12 Spetember, 2007.
http://www.terrasar.de/

International GNSS Service (IGS) (2005). "IGS Products Table." IGS. [On-line] 21 November, 2005.
http://igscb.jpl.nasa.gov/components/prods.html

Jin, X. (1996). *Theory of Carrier Adjusted DGPS Positioning Approach and Some Experimental Results.* Delft University Press, Delft, The Netherlands, 162 pp.

Khattanov, B., M. Murphy, M. Gnedin, B. Cruickshank, J. Boisvert, J. Sheffel, V. Jayaraman, V. Yudin, T. Fuller-Rowell (2004). "An Ionospheric Forecasting System." Proceedings of the 17th International Technical Meeting of the Satellite Division of The Institute of Navigation, Long Beach, California, U.S.A., 21-24 September 2004; The Institute of Navigation, Alexandria, Virginia, U.S.A., pp. 408-419.

Klobuchar, J.A. (1987). "Ionospheric Time Delay Algorithm for Single Frequency GPS Users." *IEEE Transactions on Aerospace and Electronic Systems*, Vol. AES-23, No. 3, pp. 325-331.

Klobuchar, J.A. (1996). "Ionospheric Effects on GPS." in *Global Positioning System: Theory and Applications Volume 1*, Eds. B.W. Parkinson, J.J. Spilker Jr., Progress in Astronautics and Aeronatics Volume 164, American Institute of Aeronatics and Astronautics, Inc., Washington, D.C., U.S.A., pp. 485-514.

Komjathy, A. (1999). *Global Ionospheric Total Electron Content Mapping Using the Global Positioning System.* Ph.D. Dissertation, Department of Geodesy and Geomatics Engineering Technical Report No. 188, University of New Brunswick, Fredericton, New Brunswick, Canada, 248 pp.

Kouba, J. and P. Héroux (2001). "Precise Point Positioning Using IGS Orbit and Clock Products." GPS Solutions, Vol. 5, No. 2, pp.12-28.

Langley, R.B. (1997). "GPS receiver system noise." *GPS World*, June, Vol. 8, No. 6, pp. 40-45.

Langley, R.B. (1998). "A primer on GPS antennas." *GPS World*, July, Vol. 9, No. 7, pp. 73-77.

Langley, R.B. (2000). "Smaller and smaller: The evolution of the GPS receiver." *GPS World*, April, Vol. 11, No. 4, pp. 54-58.

Le, A.Q. (2004). "Achieving Decimetre Accuracy with Single Frequency Standalone GPS Positioning." Proceedings of the 17th International Technical Meeting of the Satellite Division of The Institute of Navigation, Long Beach, California, U.S.A., 21-24 September 2004; The Institute of Navigation, Alexandria, Virginia, U.S.A., pp. 1881-1892.

Leandro, R., M. Santos, and R.B. Langley (2007). "GAPS: The GPS Analysis and Positioning Software - A Brief Overview." Proceedings of the 20th International Technical Meeting of the Satellite Division of the Institute of Navigation, Fort Worth, Texas, U.S.A.; The Institute of Navigation, Alexandria, Virginia, U.S.A., pp. 1807-1811.

Mendes, V.B. (1999). *Modelling the Neutral-Atmosphere Propagation Delay in Radiometric Space Techniques.* Ph.D. Dissertation, Department of Geodesy and Geomatics Engineering Technical Report No. 199, University of New Brunswick, Fredericton, New Brunswick, Canada, 353 pp.

Misra, P. (1996). "The Role of the Clock in a GPS Receiver." *GPS World*, April Vol. 7, No. 4, pp.60-66.

Misra, P. and P. Enge (1999). "Special Issue on Global Positioning System." Proceedings of the IEEE. Vol. 87, Issue 1, January 1999, pp. 3-15.

Misra, P. and P. Enge (2001) *Global Positioning System: Signals, Measurements, and Performance.* Ganga-Januma Press, Lincoln, Massachusetts, 390 pp.

Montenbruck, O. and E. Gill (2000). *Satellite Orbits Models, Methods and Applications.* 1st ed., Springer, 369 pp.

Montenbruck, O. and E. Gill (2001). "Ionospheric Error Removal in the Positioning of LEO Satellites on Low Cost GPS Receivers." Proceedings of the 16th International Symposium on Spaceflight Dynamics, Pasadena, California, U.S.A. 3-7 December, Pasadena, California, U.S.A. [On-line] 31 October, 2007. http://www.weblab.dlr.de/rbrt/pdf/ISSFD_XVI13.pdf

Montenbruck, O., B. Nortier, and S. Mostert (2004). "A Miniature GPS Receiver for Precise Orbit Determination of the Sunsat 2004 Micro-Satellite." Proceedings of the 2004 National Technical Meeting of the Institute of Navigation, San Diego, California, U.S.A. January 26 - 28, 2004; The Institute of Navigation, Alexandria, Virginia, U.S.A., pp. 636-642.

Montenbruck, O., J. Williams, T. Wang and G. Lightsey (2005). "Preflight Validation of the IGOR GPS Receiver for TerraSAR-X." DLR/GSOC Document No: GTN-TST-0200, Issue 1.2, May 2, 2005, 36 pp.

Muellerschoen, R., B. Iijima, R. Meyer, Y. Bar-Sever, and E. Accad (2004). "Real-Time Point Positioning Performance Evaluation of Single-Frequency Receivers Using NASA's Global Differential GPS System." Proceedings of the 17th International Technical Meeting of the Satellite Division of The Institute of Navigation, Long Beach, California, U.S.A., 21-24 September 2004; The Institute of Navigation, Alexandria, Virginia, U.S.A., pp. 1872-1880.

National Oceanic and Atmospheric Administration (NOAA) (2006). "National Weather Service Space Environment Center" [On-Line], 5 May, 2006. http://www.sec.noaa.gov/

Ritschel, B., C. Bruhns, P. Burgess, S. Freiberg, L. Gericke, S. Kase, R. Kopischke, S. Loos, S. Lowisch, H. Palm (2006). "The integration of CHAMP and GRACE products as well as associated scientific services in the new ISDC portal" [On-Line], 16 March, 2006. http://isdc.gfz-potsdam.de/

Schaer, S. (1997). "How to Use CODE's Global Ionosphere Maps." Astronomical Institute, University of Berne, Switzerland, [On-line], 31 October, 2007 http://www.aiub.unibe.ch/ionosphere/gimman.pdf

Schaer, S., W. Guntner, and J.Feltens (1998). "IONEX: The IONosphere Map Exchange Format Version 1." Proceedings of the IGS AC Workshop, Darmstadt, Germany, 9-11 February, 1998, ESA/ESOC, Darmstadt, Germany, pp. 233-237.

Seeber, G. (1993). *Satellite Geodesy: Foundations, Methods and Applications.* Walter de Gruyter, Berlin New York, 531 pp.

Simsky, A. (2003). "*Standalone Real-Time Positioning Algorithm Based on Dynamic Ambiguities (DARTS).*" Proceedings of the 16th International Technical Meeting of the Satellite Division of The Institute of Navigation, Portland, Oregon, U.S.A., 9-12 September, 2003, The Institute of Navigation, Alexandria, Virginia, U.S.A., pp 1211-1221.

Švehla, D. and M. Rothacher (2003). "Kinematic and Reduced-Dynamic Precise Orbit Determination of Low Earth Orbiters." Advances in Geosciences (2003), European Geosciences Union, Volume 1, pp. 47–56.

Tétreault, P., J. Kouba, P. Héroux, and P. Legree (2005). "CSRS-PPP: An Internet Service for GPS User Access to the Canadian Spatial Reference Frame." *Geomatica*, Vol. 59, No. 1, pp. 17-28.

Teunissen, P.J.G. and A. Kleusberg (1998). *GPS for Geodesy*. Springer, Berlin, New York, 650 pp.

van der Wal, A. D. (1995). *Evaluation of Strategies for Estimating Residual Neutral-Atmosphere Propagation Delay in High-Precission Global Positioning System Data Analysis.* M.Sc.E. Thesis, Department of Geodesy and Geomatics Engineering Technical Report No. 177, University of New Brunswick, Fredericton, New Brunswick, Canada, 106 pp.

van Leeuven, S. (1998). "Garmin 25LP OEM Receiver Tested." [On-Line] 17 November 1998.
http://home-2.worldonline.nl/~samsvl/25lptest.htm

University of New Brunswick (UNB) WAAS Monitoring Station (2004). "UNB Wide Area Augmentation System Monitoring Station." [On-Line] 6 October, 2004.
http://gauss.gge.unb.ca/WAAS/UNB.WAAS.html

Vaníček P., R.B. Langley, D.E. Wells, D. Delikaraoglou (1984). "Geometrical Aspects of Differential GPS Positioning." *Bulletin Géodésique*, Vol. 58, pp. 37-52.

Weil, L. (1992). "Submeter Positioning With a Low-Cost Hand-Held Receiver." Proceedings of the 5th International Technical Meeting of the Satellite Division of The Institute of Navigation, Albuquerque, New Mexico, U.S.A., 16-18 September, 1992, The Institute of Navigation, Alexandria, Virginia, U.S.A., pp 647-654.

Wells, D. and E. Krakiwsky, (1971). *The Method of Least-Squares.* Department of Geodesy and Geomatics Engineering Lecture Notes No. 18, University of New Brunswick, Fredericton, New Brunswick, Canada, 180 pp.

Wielgosz, P, D. Grejner-Brzezinska, I. Kashani (2005). "High-Accuracy DGPS and Precise Point Positioning Based on Ohio CORS Network". Navigation: Journal of the Institute of Navigation, Vol. 52, No. 1, Spring 2005; The Institute of Navigation, Alexandria, Virginia, U.S.A., pp. 23-28.

Wu, S-C. and Y.E. Bar-Sever (2006). "Real-Time Sub-cm Differential Orbit Determination of Two Low-Earth Orbiters With GPS Bias Fixing." Proceedings of the 19th International Technical Meeting of the Satellite Division of The Institute of Navigation, Fort Worth, Texas, U.S.A., 26-29 September 2006; The Institute of Navigation, Alexandria, Virginia, U.S.A., pp. 2515 - 2522.

Yunck, T.P. (1996). "Orbit Determination." in *Global Positioning System: Theory and Applications Volume 2*, Eds. B.W. Prkinson, J.J. Spilker Jr., Progress in Astronautics and Aeronatics Volume 164, American Institute of Aeronatics and Astronautics, Inc., Washington, D.C., U.S.A., pp. 559-592.

Appendix I: Call Graph for the Main Function

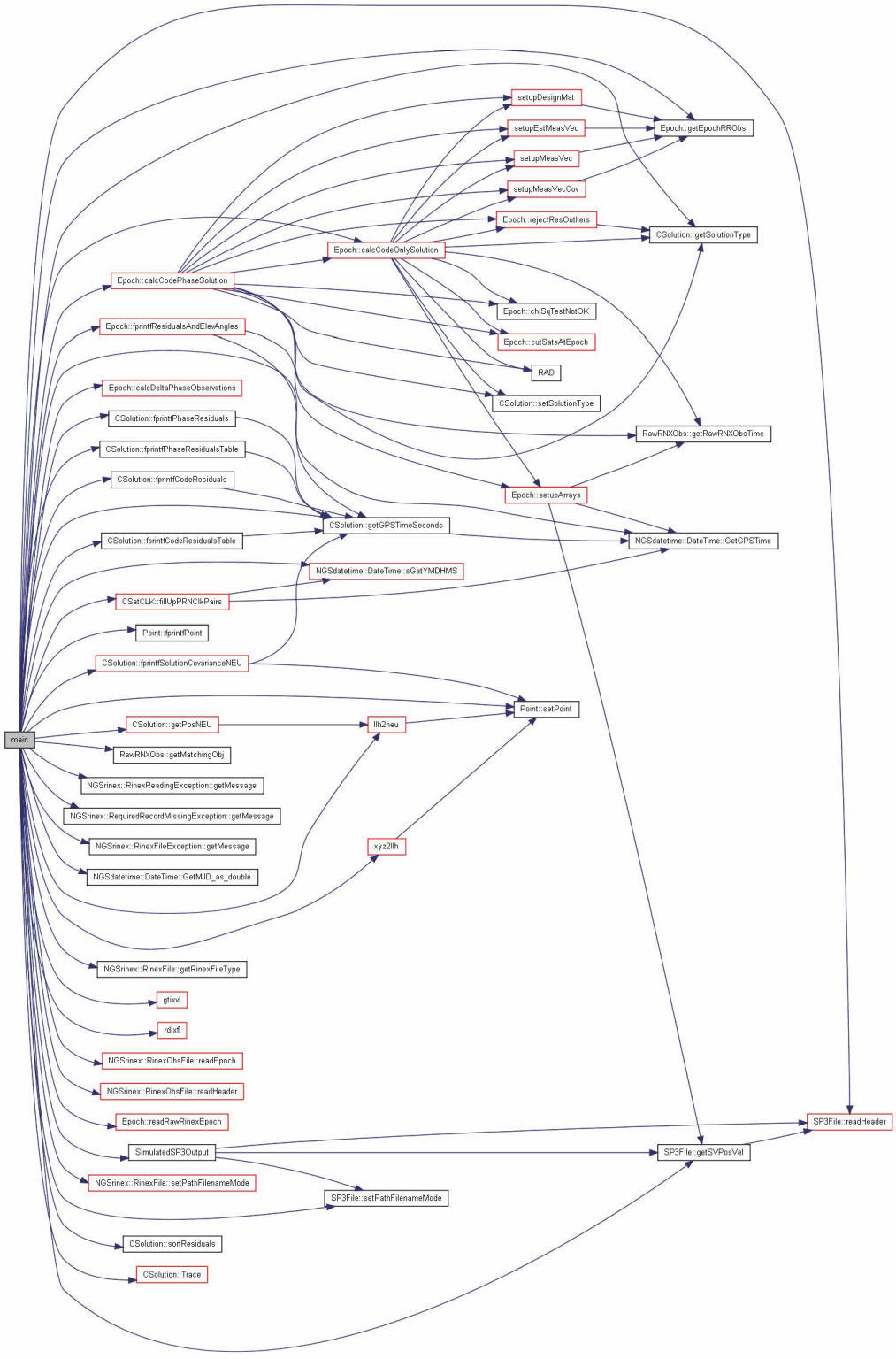

Appendix II: Call Graph for the calcCodePhaseSolution() Function

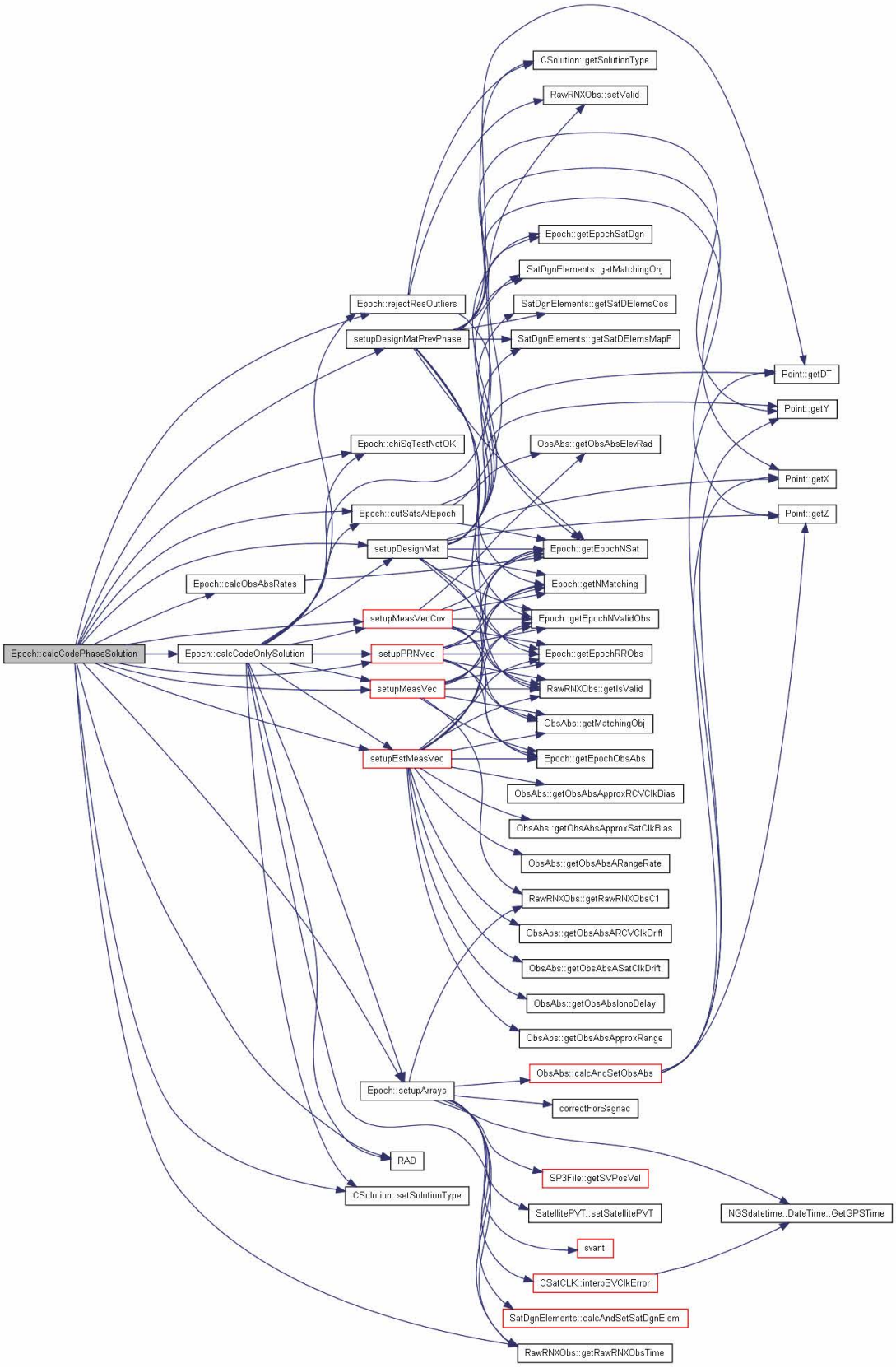

Appendix III: Example of Configuration File

```
#ifndef __CONFIG_h
#define __CONFIG_h

#include "newmat.h"
#include "constants.h"


#define NUMOFUNKNOWNS_NORMAL     4    /* number of unknown states -- x,
y, z, dt */
#define NUMOFUNKNOWNS_CALC_IONO  5    /* number of unknown states -- x,
y, z, dt, diono_zenith */


#define NUMOFUNKNOWNS (CONFIG.m_iNumUnknowns)  /* number of unknown
states */


class CConfig
{
  public:

      const bool   m_bIonoFree;                                  /* flag
to use iono-free data */
      const bool   m_bUseP1Pseudorange;                  /* flag to
use P1 pseudorange */
      const bool   m_bUseCodeOutlierDetection;       /* flag to enable
code residual outlier detection */
      const bool   m_bUsePhaseOutlierDetection;      /* flag to enable
phase residual outlier detection */
      const bool   m_bUseHighRateClock;                  /* flag to
use high rate clock file */
      const bool   m_bCodeOnlySolution;                  /* flag to
use only code observations */
      const int    m_iElevationCutoffAngleDeg;       /* elevation angle
cut-off [deg] */
      const int    m_iNumUnknowns;                           /* 5 for
Iono Estimation, 4 otherwise */
      const double m_dSigmaPseudorange;                  /*
pseudorange standard deviation [m] */
      const double m_dSigmaCarrierPhase;                 /* carrier
phase standard deviation [m] */
      const double m_dAprioriVarianceFactor;             /* apriori
variance factor */
      const double m_dResOutlierTreshold;                /* residual
outlier treshold [m] */
      const double m_dPhaseDiffThreshold;                /* phase
diff outlier threshold */
      ColumnVector m_CVBlockIIAPRN;                      /* Block
II/IIA PRN's as of (05/02/01) */

     CConfig( const char *csFilename )
```

```
            : m_bIonoFree( false )                                  /* do
you want to use iono-free y/n */
            , m_bUseP1Pseudorange ( false )                          /* do
you want to use P1 pseudorage */
            , m_bUseCodeOutlierDetection( true )            /* do you
want to enable code outlier detection */
            , m_bUsePhaseOutlierDetection( true )           /* do you
want to enable phase outlier detection */
            , m_bUseHighRateClock( true )                   /* do you
want to use high rate clock */
            , m_bCodeOnlySolution( false )                         /* flag
to use only code observations */
            , m_iElevationCutoffAngleDeg( 15.0 )            /* ALGO: 15
*/          /* GIL2: 15 */
            , m_dSigmaPseudorange( 10.0 )                   /* ALGO:
1.00 */     /* GIL2: 2.0 */
            , m_dSigmaCarrierPhase( 0.20 )                         /*
ALGO: 0.05 */     /* GIL2: 0.1 */
            , m_dAprioriVarianceFactor( 1.0 )               /* a-priori
scale factor, usually 1.0 */
            , m_dResOutlierTreshold ( 4.47 )                /* currently
disabled: could be used in res. outlier detection */
            , m_CVBlockIIAPRN(NUMOFBLOCKIIASATS)            /* Number of
block II/IIA PRN's as of (05/02/01) */
            , m_dPhaseDiffThreshold( 1.0 )                           /*
currently disabled: could be used in res. outlier detection */
            , m_iNumUnknowns( NUMOFUNKNOWNS_NORMAL ) /* to be used for
normal estimation, 4 unknowns */
//          , m_iNumUnknowns( NUMOFUNKNOWNS_CALC_IONO )     /* to be
used for zenith ionospheric delay estimation, 5 unknowns */

       {
            m_CVBlockIIAPRN(1) = 17;
            m_CVBlockIIAPRN(2) = 15;
            m_CVBlockIIAPRN(3) = 24;
            m_CVBlockIIAPRN(4) = 25;
            m_CVBlockIIAPRN(5) = 26;
            m_CVBlockIIAPRN(6) = 27;
            m_CVBlockIIAPRN(7) = 1;
            m_CVBlockIIAPRN(8) = 29;
            m_CVBlockIIAPRN(9) = 31;
            m_CVBlockIIAPRN(10) = 7;
            m_CVBlockIIAPRN(11) = 9;
            m_CVBlockIIAPRN(12) = 5;
            m_CVBlockIIAPRN(13) = 4;
            m_CVBlockIIAPRN(14) = 6;
            m_CVBlockIIAPRN(15) = 3;
            m_CVBlockIIAPRN(16) = 10;
            m_CVBlockIIAPRN(17) = 30;
            m_CVBlockIIAPRN(18) = 8;
            // added sats for January, 2002 constellation
            // change: NUMOFBLOCKIIASATS in constants.h if you use it
            /*
            m_CVBlockIIAPRN(19) = 18;
          m_CVBlockIIAPRN(20) = 16;
          m_CVBlockIIAPRN(21) = 21;
          m_CVBlockIIAPRN(22) = 22;
```

```
         m_CVBlockIIAPRN(23) = 19;
         m_CVBlockIIAPRN(24) = 23;
         m_CVBlockIIAPRN(25) = 2;
         m_CVBlockIIAPRN(26) = 17;
             */


             Load( csFilename );
        }


        void Load( const char *csFilename ) { }



};


extern CConfig CONFIG;

#endif __CONFIG_h
```

VITA

Candidate's full name: Tomáš Beran

Universities attended:

Czech Technical University
Thákurova 7
166 29 Praha 6
Czech Republic
1993-1999
Ing., 1999, Surveying Engineering

University of New Brunswick
P.O. Box 4400
Fredericton, New Brunswick, E3B 5A3
1999-2008

Publications:

Beran, T., S. Bisnath, R.B. Langley and L. Serrano (2007). "High-Accuracy Point Positioning with Low-Cost GPS Receivers." *Navigation: Journal of the Institute of Navigation, Vol. 54, No. 1, Spring 2007; The Institute of Navigation, Alexandria, Virginia, U.S.A., pp. 53-63.*

Beran, T., S. Bisnath, R.B. Langley and L. Serrano (2005). "High-Accuracy Point Positioning with Low-Cost GPS Receivers: How Good Can It Get?"*Proceedings of ION GPS/GNSS 2005, 18th International Technical Meeting of the Satellite Division of The Institute of Navigation*, Long Beach, CA, 13-16 September 2005, The Institute of Navigation, Alexandria, Virginia, U.S.A., pp. 1524-1534.

Beran, T., S. Bisnath, and R.B. Langley (2004). "Evaluation of High-Precission, Single-Frequency GPS Point Positioning Models." *Proceedings of ION GPS/GNSS 2004, 17th International Technical Meeting of the Satellite Division of The Institute of Navigation*, Long Beach, CA, 21-24 September 2004, The Institute of Navigation, Alexandria, Virginia, U.S.A., pp. 1893-1901.

Beran, T., (2003). "Single-Frequency, Single-Receiver Spaceborne GPS Orbit Determination.", Ph.D. Dissertation Proposal, Department of Geodesy and Geomatics Engineering, University of New Brunswick, Fredericton, Canada, 30 pp.

Beran, T., D. Kim, and R.B. Langley (2003). "High-Precision Single-Frequency GPS

Point Positioning." *Proceedings of ION GPS/GNSS 2003, 16th International Technical Meeting of the Satellite Division of The Institute of Navigation*, Portland, OR, 9-12 September 2003, The Institute of Navigation, Alexandria, Virginia, U.S.A., pp. 1192-1200.

Beran, T., D. Kim, and R.B. Langley (2002). "Multipath Filtering in the Spaceborne Environment: Simulation Study." Poster presented at the GEOIDE 4th Annual Conference, Toronto, Ontario, 22-24 May 2002.

Bisnath, S., T. Beran, and R.B. Langley (2002). "Precise Platform Positioning with a Single GPS Receiver." *GPS World*, Vol. 13, No. 4, 2002; pp. 42 – 49.

Beran, T., S.B. Bisnath, and R.B. Langley (2001). "Single Receiver GPS Positioning in Support of Airborne Gravity for Exploration and Mapping." Poster presented at the GEOIDE 3rd Annual Conference, Fredericton, 20-22 June 2001.

Bruton, A. M., M. Kern, K.P. Schwarz, S. Ferguson, A. Simsky, K. Tennant, M.Wei, J. Halpenny, R. Langley, T. Beran, K. Keller, P. Mrstik, K. Kusevic and R. Faulkner (2001). "On the accuracy of Kinematic Carrier Phase DGPS for Airborne Mapping.", *Geomatica*, Vol. 55., No. 4, 2001; pp.491 – 507.

Beran, T. (2000). "Improvement of GPS Ambiguity Resolution." Graduate Student Seminar, Department of Geodesy and Geomatics Engineering, University of New Brunswick, Fredericton, Canada, pp. 15.

Beran, T. (1999). Zaměření osy koleje kinematickou metodou GPS (Measurement of the railroad track axis by kinematic GPS method). Masters diploma thesis, K 152 Department of Advanced Geodesy, Faculty of Civil Engineering, Czech Technical University, Prague, Czech Republic, 54 pp.

Conference presentations:

Beran, T., S. Bisnath, R.B. Langley and L. Serrano (2005). "High-Accuracy Point Positioning with Low-Cost GPS Receivers: How Good Can It Get?"*Proceedings of ION GPS/GNSS 2005, 18th International Technical Meeting of the Satellite Division of The Institute of Navigation*, Long Beach, CA, 13-16 September 2005, The Institute of Navigation, Alexandria, Virginia, U.S.A., pp. 1524-1534.

Beran, T. (2004). "Review and Analysis of Deformation monitoring Techniques.", Course on Deformation Surveys and Related Topics, Canadian Centre for Geodetic Engineering, Fredericton, NB, Canada, December 2, 2004.

Beran, T., S. Bisnath, and R.B. Langley (2004). “Evaluation of High-Precission, Single-Frequency GPS Point Positioning Models.” *Proceedings of ION GPS/GNSS 2004, 17th International Technical Meeting of the Satellite Division of The Institute of Navigation*, Long Beach, CA, 21-24 September 2004, The Institute of Navigation, Alexandria, Virginia, U.S.A., pp. 1893-1901.

Beran, T., (2003). “Single-Frequency, Single-Receiver Spaceborne GPS Orbit Determination.”, Ph.D. Dissertation Proposal Defence, Department of Geodesy and Geomatics Engineering, University of New Brunswick, Fredericton, Canada, 30 pp.

Beran, T., D. Kim, and R.B. Langley (2003). "High-Precision Single-Frequency GPS Point Positioning." *Proceedings of ION GPS/GNSS 2003, 16th International Technical Meeting of the Satellite Division of The Institute of Navigation*, Portland, OR, 9-12 September 2003, The Institute of Navigation, Alexandria, Virginia, U.S.A., pp. 1192-1200.

Beran, T. (2000). “Improvement of GPS Ambiguity Resolution.” Graduate Student Seminar, Department of Geodesy and Geomatics Engineering, University of New Brunswick, Fredericton, Canada, pp 15.

Beran, T. (1999). Zaměření osy koleje kinematickou metodou GPS (Measurement of the railroad track axis by kinematic GPS method). Masters thesis defence, K 152 Department of Advanced Geodesy, Faculty of Civil Engineering, Czech Technical University, Prague, Czech Republic, 54 pp.